CONTROL STRATEGIES AND MOTION PLANNING FOR NANOPOSITIONING APPLICATIONS WITH MULTI-AXIS MAGNETIC-LEVITATION INSTRUMENTS

A Dissertation

by

HUZEFA SHAKIR

Submitted to the Office of Graduate Studies of
Texas A&M University
in partial fulfillment of the requirements for the degree of

DOCTOR OF PHILOSOPHY

May 2007

Major Subject: Mechanical Engineering

CONTROL STRATEGIES AND MOTION PLANNING FOR NANOPOSITIONING APPLICATIONS WITH MULTI-AXIS MAGNETIC-LEVITATION INSTRUMENTS

A Dissertation

by

HUZEFA SHAKIR

Submitted to the Office of Graduate Studies of
Texas A&M University
in partial fulfillment of the requirements for the degree of

DOCTOR OF PHILOSOPHY

Approved by:

Chair of Committee,	Won-jong Kim
Committee Members,	Suhada Jayasuriya
	Alexander Parlos
	Jim Boyd
Head of Department,	Dennis O'Neal

May 2007

Major Subject: Mechanical Engineering

ABSTRACT

Control Strategies and Motion Planning for Nanopositioning Applications with Multi-Axis Magnetic-Levitation Instruments.

(May 2007)

Huzefa Shakir,

B. Tech. (Honors), Indian Institute of Technology, Kharagpur

Chair of Advisory Committee: Dr. Won-jong Kim

This dissertation is the first attempt to demonstrate the use of magnetic-levitation (maglev) positioners for commercial applications requiring nanopositioning. The key objectives of this research were to devise the control strategies and motion planning to overcome the inherent technical challenges of the maglev systems, and test them on the developed maglev systems to demonstrate their capabilities as the next-generation nanopositioners. Two maglev positioners based on novel actuation schemes and capable of generating all the six-axis motions with a single levitated platen were used in this research. These light-weight single-moving platens have very simple and compact structures, which give them an edge over most of the prevailing nanopositioning technologies and allow them to be used as a cluster tool for a variety of applications. The six-axis motion is generated using minimum number of actuators and sensors. The two positioners operate with a repeatable position resolution of better than 3 nm at the control bandwidth of 110 Hz. In particular, the Y-stage has extended travel range of 5 mm × 5 mm. They can carry a payload of as much as 0.3 kg and retain the regulated position under abruptly and continuously varying load conditions.

This research comprised analytical design and development, followed by experimental verification and validation. Preliminary analysis and testing included open-loop stabilization and rigorous set-point change and load-change testing to demonstrate the precision-positioning and load-carrying capabilities of the maglev positioners. Decentralized single-input-single-output (SISO) proportional-integral-derivative (PID) control was designed for this analysis. The effect of actuator nonlinearities were reduced through actuator characterization and nonlinear feedback linearization to allow consistent performance over the large travel range. Closed-loop system identification and order-reduction algorithm were developed in order to analyze and model the plant behavior accurately, and to reduce the effect of unmodeled plant dynamics and inaccuracies in the assembly. Coupling among the axes and subsequent undesired motions and crosstalk of disturbances was reduced by employing multivariable optimal linear-quadratic regulator (LQR). Finally, application-specific nanoscale path planning strategies and multiscale control were devised to meet the specified conflicting time-domain performance specifications. All the developed methodologies and algorithms were implemented, individually as well as collectively, for experimental verification. Some of these applications included nanoscale lithography, patterning, fabrication, manipulation, and scanning. With the developed control strategies and motion planning techniques, the two maglev positioners are ready to be used for the targeted applications.

To my parents Ismail and Sabera Shakir

and

my wife Zahabiya

ACKNOWLEDGMENTS

The completion of this dissertation towards my doctoral degree would not have been possible without the encouragement, support and guidance of many. First of all, I would like to thank my parents, Sabera and Ismail Shakir, for all the trust, support, and love that they have bestowed upon me. I owe them every success of my life.

I would like to express my heartfelt gratitude to my advisory committee chair Prof. Won-jong Kim, for his consistent encouragement and moral support throughout my research. I appreciate his giving me a chance to formulate my research problem and to pursue it my own way. He was also very supportive in providing me several opportunities to publish and present my work in reputed journals and conferences. My interaction with him over the past four years was a great learning experience in all aspects of research.

I am grateful to Profs. Suhada Jayasuriya, Alexander Parlos, and Jim Boyd for serving as my committee members. My course-work under the instruction of Prof. Jayasuriya laid the foundation for most of the work presented in this dissertation. I would also like to thank Profs. Parlos and Boyd for sharing their wisdom and expertise with me. I appreciate their taking time to evaluate my work and giving me their precious comments.

In addition to having a great research experience during my studies at Texas A&M, I also gained valuable insights into teaching through my appointments as teaching assistant for two years. My special thanks go to Profs. Ben Zoghi, Darbha Swaroop, Alexander Parlos, Craig Smith, Jingang Yi, and William Schneider. I learned a lot from them about teaching philosophies and class management with a variety of courses, class-levels and class-sizes.

This doctoral work would not have been successful without cooperation of my colleagues. In particular, I would like to thank Dr. Kim’s former graduate students and my

friends Shobhit Verma and Jie Gu. Jie worked on the design of the Δ-stage and software development for the user interface. Design of Y-stage, and fabrication and precision assembly of both the stages were done by Shobhit. I also thank everyone else in the Precision Mechatronics and Nanotechnology Lab for the friendly environment they made.

A special note of thanks goes to my wife Zahabiya for her unbounded love, encouragement, and understanding. I also owe appreciation to all my friends for providing a friendly atmosphere and making my stay here an enjoyable and memorable experience. Last but not the least, I express my deepest gratitude to God, the almighty and merciful, for blessing me with knowledge and diligence, and having made this whole experience yet another endorsement of faith and hard work.

This material was supported in part by the National Science Foundation under Grant No. CMS-0116642 through Dr. Won-jong Kim.

TABLE OF CONTENTS

Page

Page

Page

LIST OF FIGURES

FIGURE Page

FIGURE Page

FIGURE Page

FIGURE Page

FIGURE Page

LIST OF TABLES

CHAPTER I

INTRODUCTION

1.1 Background and Motivation

Manufacturing and manipulation at nanoscale is one of the major research-and-development focus areas in the application of the nanotechnology and has significant economic and societal impacts[1] [1]. Commonly used nanopositioning devices include scanning probe microscopes (SPMs) and atomic force microscopes (AFMs). In industry, linear motors and servomotors are still popular for microscale positioning. Finer positioning is achieved using separate actuators such as piezoelectric actuators. The key role of a precision positioning system is to load, position, and orient an object, and regulate or track its position at desired levels without getting affected by external process and measurement noises. This requires high positional accuracy, large travel range, and simultaneous generation of multi-degree-of-freedom (DOF) motions and high control bandwidth. Most of the conventional methods have several limitations due to which they cannot meet these demanding performance requirements. This situation calls for the development of high-precision positioning methodologies and application-specific tools [2].

Magnetic levitation has been demonstrated to meet these stringent requirements. The main benefit of magnetic levitation over other prevailing technologies is its non-contact nature while in operation, i.e., the forces are applied to the moving part without any mechanical contact.

This dissertation follows the format of *IEEE Transactions on Mechatronics*.

[1] National Nanotechnology Initiative [Online]. Available: http://www.nano.gov/html/research/nnigc.html.

Thus there is no friction, hysteresis, or backlash. Due to the absence of friction, the moving part can be modeled as a pure mass. This maglev technology is suitable for clean-room or vacuum environments since it does not require any lubricants or generate wear particles. Furthermore, without complex mechanical elements, the fabrication cost can be substantially reduced.

Several research groups have been working on a variety of concepts using magnetic levitation to meet the demanding requirements of nanopositioning. However, most of the results available in literature focus primarily on the design and fabrication aspects of maglev positioners. Very little attention has been given to the commercialization aspect of this powerful technology, which is capable of replacing most of the prevailing positioning methods. In this dissertation, an attempt has been made to demonstrate the use of maglev positioners for commercial application. Control strategies and motion planning have been devised to overcome the inherent shortcomings of this technology. Accordingly, it centers around three key terms – maglev nanopositioners, control strategies, and commercial applications requiring precision positioning.

1.2 Review of Prior Art

1.2.1 Magnetic Levitation

Maglev technology has been demonstrated successfully for nanopositioning applications. It uses electromagnetic force for levitation as well as propulsion and has been found to be very useful for precision motion control. Several research groups developed multi-axis precision positioning devices using this technology. Kim *et al*. [3], Shan *et al*. [4], Holmes *et al*. [5], and Hajjaji *et al*. [6] have done pioneering work in high-precision magnetic levitation. Kim *et al*. constructed a 6-DOF high-precision planar maglev stage using a concentrated-field magnet matrix, which generates a constant 3-D magnetic field for actuation [3, 7, and 8]. The magnet

matrix was constructed by the superimposition of two orthogonal Halbach magnet arrays. This maglev stage demonstrated a position resolution of 20 nm at a 100-Hz control bandwidth with a planar travel range of 160 mm × 160 mm .The maximum velocity of this stage was 0.5 m/s at a 0.5 m/s^2 acceleration, which implies an enhanced throughput in precision manufacturing. Verma *et al*. [9] and Gu *et al*. [10] demonstrated the use of a multi-axis maglev nanopositioner for precision manufacturing and manipulation applications which is capable of carrying and orienting a payload up to 0.3 kg with a position resolution better than 2 nm and with a total nominal power consumption of 1 W.

Similar work has been pursued by other research groups in related applications. A maglev scanning stage that is capable of a 0.6-nm three-sigma horizontal position noise was fabricated and demonstrated by Holmes *et al*. [5]. The stage utilizes four levitation linear motors to suspend and servo the moving element throughout its 25 mm × 25 mm × 0.1 mm range of travel. Position feedback is provided by three plane-mirror interferometers and three capacitance probes. The suspended platen of 12 kg mass is floated in oil to enhance the stage's disturbance rejection and to reduce power dissipation in the actuators. Jung and Baek designed and demonstrated a 6-DOF maglev positioner with self-stability for 5 DOFs [11]. It has a moving mass of 173 g and had a position resolution of 0.5 μm in 32-mm-wide *x*-*y* planar motion and a 0.45-μm resolution in *z* motion. The development and motion control of a large-travel ultra-precision magnetic suspension stage was presented by Menq *et al*. [4, 12]. Galburt *et al*. [13, 14] developed an apparatus adapted to align a wafer in a microlithography system. It consists of a monolithic stage, a sub-stage, an isolated reference structure, and force actuators and sensors.

In yet other set of applications, Hollis *et al*. developed a maglev fine motion wrist with programmable compliance [15, 16]. The floater carries an end effector which may be used as a tool. The control unit changes the forcer coil current patterns as the fine motion device

approaches its final position in order to provide selected compliance in one or more DOFs. An optical pickup apparatus with a magnetic circuit was developed by Kano [17] which has an application in an optical-type recording and reproducing apparatus. Khamesee *et al*. demonstrated the application of magnetic levitation in a micro-robotic system used for transportation and assembly of miniature parts in hazardous environment [18]. This microrobot can be remotely operated in 3 DOFs in an enclosed environment by transferring magnetic energy and optical signals from outside. A dual-axis repulsive maglev guiding system was developed using permanent magnets [19]. This system uses a modified voice-coil motor, a passive carrier, and an active track.

1.2.2 Precision-Motion-Control Strategies

A. System Identification

System identification is necessary in order to get an accurate plant model and subsequently to prove the effectiveness of the developed control strategies. In the case of a maglev system, this is crucial as well as challenging because of the inherently unstable nature of magnetic levitation. Thus, the system identification needs to be performed in closed loop. There are a few results reported in literature on closed-loop identification. Kuo *et al*. used system identification to validate their proposed mathematical model as well as parameter variations due to changing air gaps for the ultra-precision motion control of a magnetic-suspension stage [12]. Dejima *et al*. used step responses with PID controller in order to identify the parameters of the plant transfer function (TF) [20]. Villota *et al*. constructed additive uncertainty models by using a zero-mean white-noise random signal as a reference input for system modeling [21].

In this research, an attempt has been made to carry closed-loop identification a step further in order to obtain a reliable and complete plant model. The Box-Jenkins (BJ) method

with a closed-loop framework and a known controller structure is used to obtain the closed-loop TF [22, 23, and 24]. It is assumed that the measurable part of the input is known precisely and that noisy observations of the output are available. A parametric plant and noise model is then identified simultaneously from the sampled input-output signals. The advantage of using this frequency-domain approach is that the identified model neither requires any guess-work for parameter estimation nor depends upon the initial conditions or operating point, at least for a linear time-invariant (LTI) plant.

B. Classical Methods in Motion Control

A number of researchers have been working on various problems associated with motion control systems such as maglev, servomotors, AFM, etc. The problems of particular interest are precision positioning, system bandwidth, parameter variations, actuator nonlinearities, external disturbances, and sensor noise. Endo *et al*. used a combination of a feedforward controller and a robust feedback controller for digital tracking of high-speed poisoning systems [25]. The feedforward controller anticipates and compensates for the closed-loop dynamics and the feedback controller compensates mechanical nonlinearities, parameter variations, and disturbances. Feedforward control was also used by Yasuda *et al*. to suppress microvibrations in precision machines, for example, for semiconductor manufacturing [26]. This feedforward signal was not generated online but was computed in advance from the response to the direct disturbance and a TF from control input to the controlled output. Kuo *et al*. proposed a parameter variation model in conjunction with a reduced-order observer to compensate the joined effect of disturbance, modeling error, and cross-coupling [27]. Hajjaji and Ouladsine built a nonlinear control model for long-range movement of a maglev system and tested it by real-time control implementation [6]. Sebastian and Salapaka demonstrated the effectiveness of an

$\mathcal{H}_\infty$ control to improve the positioning speed and precision of AFM for imaging of biological samples, while eliminating the undesirable nonlinear effects of the actuator [28]. The AFM was actuated by a piezoelectric stack and its motion was sensed by a linear variable differential transformer. Noise levels are also significant in precision positioning systems since the reliability of the sensor data relies on that. Particularly, if the data is read using an analog device and digitized for further processing, a measurement uncertainty component is incurred from quantization. This uncertainty can be reduced by oversampling and averaging multiple measurements [29].

C. Multivariable Control

Since only one moving part generates all the motions its dynamics is coupled in 6 DOFs. Thus a multivariable LQR is a natural choice to regulate the position of the platen, the moving part. Kim *et al*. have designed a multivariable optimal control of a 6-DOF maglev stage with large motion capabilities [3]. Nakashima *et al*. designed a servosystem for suppressing natural vibrations of a maglev system using the closed-loop identification and $\mathcal{H}_\infty$ control theory [30]. Becerril-Arreola, *et al*. performed nonlinear set-point stabilization for the control of a 3-DOF maglev system [31].

There are many research results on macroscopic time-optimal control especially in path planning in robotics [30, 32, and 33]. However, no significant literature is available for manufacturing applications at nanoscale. I designed and implemented a multivariable LQR for the lateral modes (x, y and the angle about the z-axis) of the maglev stage to reduce the coupling among the axes [34]. Although I have used well-established classical and modern control

techniques to design the controllers, the designed methodologies enable path planning and motion control at nanoscale.

D. Multiscale Control

A problem of continuing interest in feedback control is handling the performance specifications of a controller to meet given time-domain characteristics, some or all of which may be conflicting in nature. In particular, the desired performance specifications may require (1) fast response (in rise and settling times) with little or no overshoot (2) large travel range with nanometer-level position resolution. Fast response is important in applications like a manipulator's pick-and-place operations near a wall, filling a tank with fluid in minimum time without spilling over, and temperature control in hazardous environment. Fine position resolution and high accuracy are required in applications like microstereolithography, nanopositioning, and scanning and imaging of nanoscale phenomena. In these applications, however, there is a notable trade-off between the position accuracy and the process throughput, particularly in the applications requiring large travel ranges. High position accuracy can be achieved for large travel if the scan speed is kept very slow. However, in commercial applications like semiconductor manufacturing, high position resolution as well as throughput is important. I use the term *multiscale control* throughout this paper in order to emphasize the fact that such control is capable of meeting such conflicting time-domain performance specifications and providing desired performances in both nanoscale and macroscale operations.

Despite the advancement in the control theory over the last few decades, this problem of dealing with conflicting time-domain performance specifications remains open. One reason is that there is no analytic relationship between the system parameters and the time-domain transient-response characteristics for systems of the order higher than two [35]. Even with the

conventional optimal-control techniques, the problem cannot be completely solved. The controllers tuned for load changes tend to produce large overshoots for reference tracking whereas those tuned for reference tracking would result in sluggish recovery from load disturbances. This fact will be further demonstrated using an example of maglev positioner in Chapter VII (Fig. 7.2). A detailed description of the conventional optimal PI control and the difficulties associated with it is also given in Chapter VII.

Several methods were suggested in literature to achieve time-domain performance specifications using various control techniques. Deodhare and Vidyasagar [36] and Phillips and Seborg [37] gave the conditions for non-overshooting feedback control systems for linear systems. Vidyasagar [38] and Jayasuriya and Dharne [39] described the conditions for non-overshooting and non-undershooting responses based on the number of non-minimum-phase plant zeros. Moore and Bhattacharyya [35] and Darbha and Bhattacharyya [40] proposed controller synthesis based on a zero-placement method to achieve non-overshooting step responses and sign-invariant impulse responses, respectively. Datta *et al*. [41] and Ho [42] designed fixed-order constant-gain, PI and PID controllers, which met the specified time-domain characteristics. Among other techniques to reduce the overshoot are set-point filtering, in which the set-point is filtered before it enters the feedback loop; model-following approach, in which the objective is to make the plant output follow the output of a reference model as closely as possible; anti-reset wind-up; and ramping the set-point to its new value in small increments [43, 44].

Some of these methods are based on several assumptions, like open-loop stability of the plant, a pre-specified relationship between the zeros and poles of the plant, or a strictly proper SISO plant [36, 37, 38, and 39]. The developed control methods also have several limitations. Some of them require solving a partially finite convex programming problem while others

involve searching for a solution over the entire set of the stability region, which may be unbounded [42]. Furthermore, the synthesized controllers may be of a very high order and thus affect the overall robust stability of the closed loop [45]. This motivates the need to develop multiscale-control schemes that can satisfy the time-domain performance specifications in a unified way. It turns out that by relieving the constraint of overshoot from strictly non-overshooting to sub-optimally overshooting, the problem under discussion may be much simplified. Suitable modifications of the existing optimal control techniques can provide significant improvements in time-domain performances. Besides, if full-state feedback is available, the excellent stability margin of optimal control is an added advantage.

1.2.3 Applications of Motion Control in Industry

A. Semiconductor Manufacturing

Precision positioning stages plays a vital role in the semiconductor manufacturing industry. Some of the key requirements of wafer stages used for lithography, also known as steppers or step-and-repeat aligners, are (1) multi-axis high-resolution positioning capability, (2) repeatability, (3) large travel, (4) high throughput, and (5) excellent disturbance-rejection capabilities for defect-free wafers. Nikon's NSR-S610C is the industry's first scanner for 45 nm mass production and development of 32 nm devices[2]. This high-accuracy positioning is achieved with the tandem stage, shown in Fig. 1.1, which is designed for high volume manufacturing and provides optimized performance and efficiency for immersion lithography. The exposure stage processes wafers at very high rates, while the calibration stage is used for calibrations during

[2] Nikon Precision Inc. [Online]. Available: http://www.nikonprecision.com/products/nsr_s610c.html.

wafer exchange. The tandem stage enables throughput ≥130 wafers per hour, and delivers wet-dry overlay matching equivalent to dry system performance.

However, the shrinking feature sizes, increased wafer sizes, demanding overlay accuracy, and competitive throughput requirements introduce significant design challenges in semiconductor manufacturing. Most of the traditional wafer handling systems mainly consist of pneumatic, hydraulic, and mechanical/electromechanical devices. Such systems are complex in design, and expensive and time-consuming to produce and maintain [46]. Therefore, a reliable low-cost positioning system for precision manufacturing processes requiring clean-room, extreme-temperature, or vacuum environments is the key for the microelectronics manufacturing, packaging, and high-precision inspection industries.

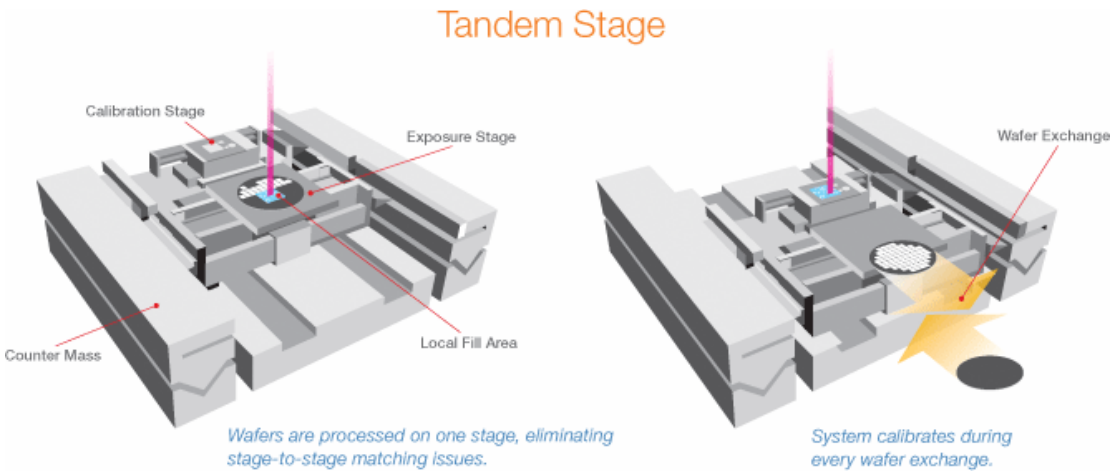

Fig. 1.1. Tandem stage operation for Nikon's NSR-S610C lithography equipment (Source: Nikon Precision Inc.)

B. Microstereolithography

Microstereolithography (μSTL) is another application requiring high-accuracy positioning for the manufacture or prototyping of small scale objects. Classical stereolithography (STL) processes use separate motion control stages for *x*-*y* and *z* axis motions as shown in Fig.

1.2(a). These motion control stages are driven by servo motors with a position resolution about 0.5 μm. Another schematic shown in Fig. 1.2(b) uses a laser beam deflected by a pair of low-inertia-galvanometric mirrors and focused by a dynamic lens to solidify photopolymer [47]. This methodology works well for objects on the order of a few hundred micrometers. However, beam defocusing becomes problematic for smaller objects. An alternate approach is to keep the laser beam fixed and use a high-precision positioning stage to generate *x-y* motions for scanning [48]. Beluze *et al.*, Zhang *et al.*, and Jiang *et al.* have used this kind of *x-y* stages for μSTL [49, 50, and 51]. Ikuta *et al.* showed the capability of such stages for the mass integrated harden polymer STL process [52]. However, in all these processes, the minimum achievable part size is limited by the position resolution of the stage being used. In the work presented herein, I have demonstrated that this limitation in positioning can be easily overcome with our maglev stage.

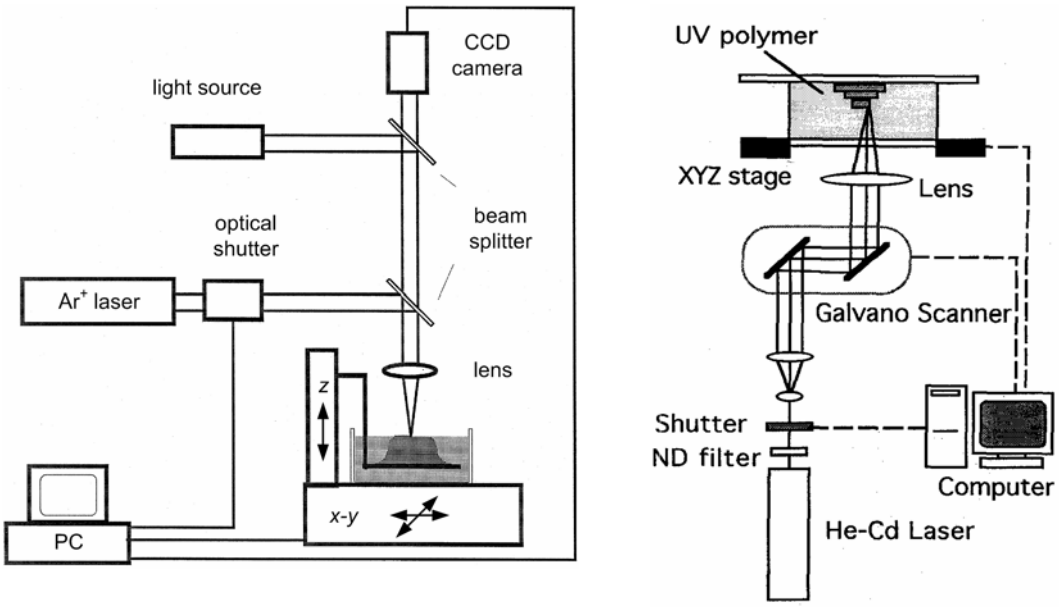

(a) (b)

Fig. 1.2. A typical μSTL setup with (a) separate *x-y* and *z* precision motion stages [50], and (b) galvanometric mirror for scanning [52]

C. SPM Based Scanning, Imaging and Nanomanipulation

The development of the Scanning Probe Microscope (SPM) initiated a variety of atomic-level profiling and characterizing instruments. SPM measures and images the specimen's surfaces on a fine scale, down to the level of molecules and groups of atoms. It is based on the concept of scanning an extremely sharp tip with a 3–50 nm radius of curvature, across the object surface. The tip is mounted on a flexible cantilever, allowing the tip to follow the surface profile. SPMs are primarily operated in the *contact mode*, wherein there is physical contact between the sample and the cantilever tip and a very small constant force is maintained between the two [53]. While scanning the area of sample, the tip is deflected. The sensor system consisting of a laser diode and a position sensitive detector (PSD) senses this deflection indicating the height of the sample at that point. By following a raster pattern, the sensor data forms an image of the probe-surface interaction. The schematic of the contact mode operation is shown in the Fig. 1.3.

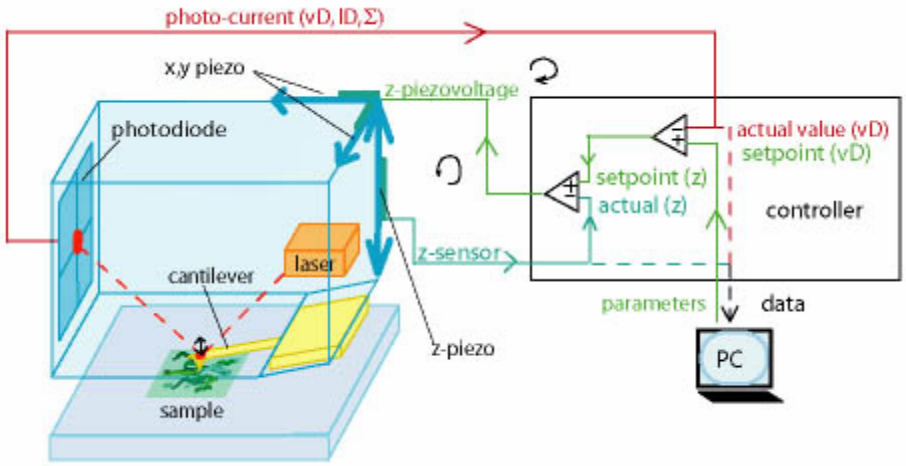

Fig. 1.3. Schematic for Atomic Force Microscopy[3]

[3] Soft Matter Physics – Atomic Force Microscopy [Online].
Available: http://www.uni-leipzig.de/~pwm/kas/afm/AFM.html.

Although their primary application was topographical imaging, SPMs have become the prime tools for nanomanipulation over the last decade [54]. Three most common SPM techniques are Atomic Force Microscopy (AFM), Scanning Tunneling Microscopy (STM), and Near-Field Scanning Optical Microscopy (NSOM). Currently most of the atomic-level positioning and profiling is accomplished by AFMs and STMs [55, 56]. As an example, the Dimension 3100 SPM[4] of Veeco Instruments utilizes automated AFM and STM techniques to measure surface characteristics for semiconductor wafers, lithography masks, magnetic media, biomaterials, etc.

Most of the actuation units in micro/nanopositioning devices are based on piezoelectric materials [56, 57]. These actuators have become a standard solution in positioning applications where the displacement must be small. However, there are certain challenges with the piezoelectric actuation systems. (1) The motion capability of these devices is usually limited to linear motions with a short travel range of around 100 μm. (2) The hysteresis in piezoelectric materials reduces the repeatability in positioning, sometimes precluding closed-loop operation [54, 58]. (3) A slow creeping motion after a large voltage step results in a significant positioning error [59]. (4) The accuracy is greatly influenced by thermal drift under temperature variation. (5) The voltage required to operate piezoelectric actuators can be as high as several hundred volts.

D. Nanopatterning

Nanopatterning is a direct-write nanofabrication technique, which plays an important role in areas such as sensor patterning, miniaturization of biological assays, and creation of nanoelectronic components. Dip-pen-nanolithography is one such application, which is

---

[4] Veeco Instruments, Applications of AFM [Online].
Available: http://web.mit.edu/cortiz/www/nanomechanics.html.

essentially the process of writing stable nanoscale patterns of molecular ink onto a sample substrate via a coated stylus tip (for example, a STM probe). Nanoink uses NSCRIPTOR™ (Fig. 1.4), a dedicated scanning probe lithography system, for dip-pen-nanolithography (DPN) process [60]. This system employs separate stage and scanner for large and small range motions. The DPN stage is driven by seven motors – two for *x*-*y* sample puck translation, one for camera lens zoom, one for 10× lens focus, and three for *z*-axis leveling and *z* tip-approach. The *x*-*y* sample translator motors have a minimum 3 μm step size, 25 mm × 25 mm travel, and maximum 2.5 mm/s slew rate. Scanning is performed with a tripod stack piezoelectric configuration, i.e., independent *x*-*y*-*z* piezos. These piezoelectric actuators have a 90-μm travel range in *x*-*y* and 8 μm in *z* with a position resolution of 10 nm in *x*-*y*.

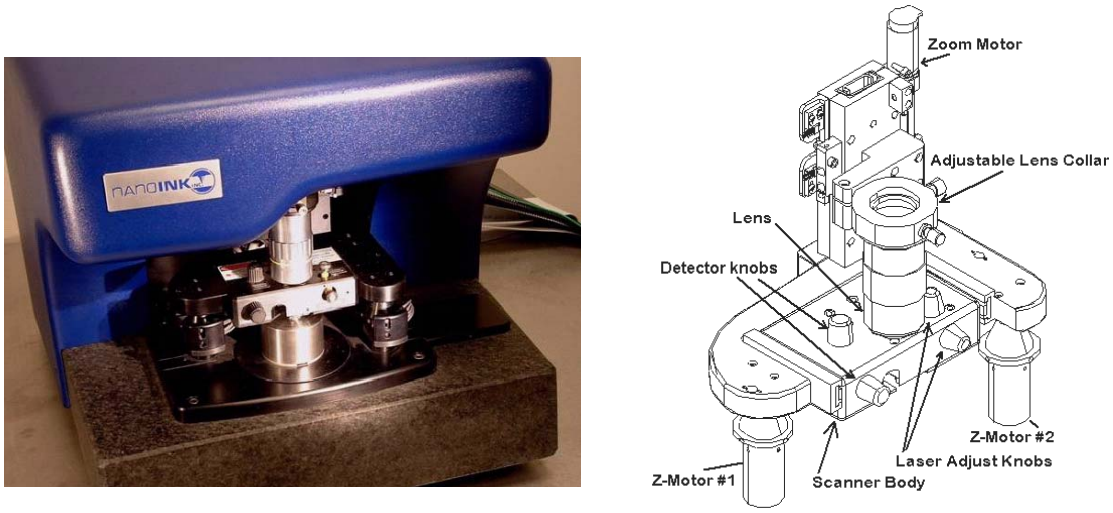

(a) (b)

Fig. 1.4. (a) Nanoink's NSCRIPTOR™ for DPN (b) Schematic of the stage [60]

They also require periodic calibration and linearization. This arrangement has several apparent shortcomings. The scanning stage requires intensive maintenance and suffers losses due

to friction from its contact-type mechanisms. It is also not suitable for clean-room operations. Piezos, on the other hand, have very limited travel range and are suitable only for microscale scanning operation, not for alignment. They also require periodic calibration and linearization because of hysteresis and creep phenomena.

1.3 Contributions of This Dissertation

Despite all the benefits of the magnetic levitation over other prevailing nanopositioning techniques, it has several inherent technical challenges: (1) the maglev systems are open-loop unstable. (2) the nonlinear relationship between current and displacement may not allow large travel ranges, (3) since only a single moving part generates all the motions, its dynamics is coupled in 6 DOFs, and (4) due to the absence of any damping or restricting force on the moving part, the overshoots to commanded steps are large. Furthermore, the performance of the stage depends on the accuracy of sensing. In our case, for instance, use of high-resolution laser-interferometer sensors results in a root-mean-square (rms) noise level of as good as 2 nm for lateral modes. However, the capacitive gauge resolution used for vertical modes is limited by the associated analog-to-digital converters (ADCs) to about 200 nm peak-to-peak.

In addition to these, the working of maglev stages has been demonstrated in literature mostly with the basic closed-loop control. When put in conjunction with a practical application, the control requirement may be more stringent. Various potential applications of the maglev nanopositioning device include μSTL, microscale rapid prototyping, dip-pen-nanolithography, scanning/imaging, ultrafine machining, manufacture of nanoscale structures, atomic level manipulation, nanoscale vibration isolation for delicate instruments, seismic motion detection and so on. These applications require tasks like loading, isolating, positioning, orienting, fabricating, or assembling the objects to be manipulated at nanoscale precision. In such

applications, this maglev stage can be used as the positioning device, and the task to be performed can be done with a fixed tool. In these applications, the presence of external forces in the form of payload variation or mass fluctuation is inevitable. For instance, in μSTL, the mass of the substrate may vary as the photopolymer is solidified. Similarly, in scanning applications, there may be abrupt changes in external forces coming on the positioner during contact-mode operation. Consequently, the maglev stage needs to be tested rigorously for set-point changes and load-changes and application-specific control strategies and motion planning need to be devised to demonstrate its use as precision positioning device in any of these applications.

1.3.1 Objectives

With reference to the above requirements, the objectives of my research are as follows.

1. To perform, as preliminary analysis, rigorous set-point change and load-change testing to demonstrate the precision-positioning and load-carrying capabilities of the maglev stages.
2. To accurately model the plant dynamics, analytically as well through system identification, for reliable and effective control designs and motion planning.
3. To devise control and motion planning strategies for using the maglev stage in conjunction with the practical applications with the following objectives.
   (a) The control schemes and motion planning should be application-specific.
   (b) They should be able to overcome the above-listed technical challenges of the maglev systems.
   (c) They should be able to meet the specified time-domain performance specifications, some of which might be conflicting in nature.

(d) To demonstrate the effectiveness of the developed methods in terms of stability, transient and steady-state behavior, and closed-loop criteria.

4. To demonstrate the use of maglev stages for several industry-relevant applications.

1.3.2 Dissertation Overview

The dissertation consists of eight chapters. Motivation and contributions of the work presented were reported in this chapter. It also provided a review of the prior art, trends in motion control in precision positioning and prevailing technologies in industry with an emphasis on applications such as semiconductor manufacturing, μSTL, SPM-based scanning, imaging and nanomanipulation, and nanopatterning. Benefits and technical challenges associated with the maglev technology and maglev positioning systems were discussed and key objectives for the research were identified in the light of these discussions.

Chapter II provides an overview of the two maglev positioners, namely the Δ- and Y-stage. The developed maglev instruments will be compared in terms of their characteristics and performance specifications. Mechanical design and sensing schemes will be described for the both the positioners. The need for developing a feedback linearization scheme, which is one of the key objectives concerning limitations of the maglev positioners, will also be discussed. Details of the design and experimental setup to characterize the behavior of nonlinearities and results of the feedback linearization will be addressed.

In Chapter III, we discuss preliminary analysis and testing of the maglev positioners. This includes analytical plant modeling, decoupled SISO PID control and testing results for the two maglev positioners. This elementary analysis is based on several assumptions, such as a pure-mass model for the plant, negligible cross-talk among the axes, linear actuator behavior and

so on. The limitations of these assumptions and simplified models will be analyzed, and motivation for developing advanced control schemes and motion planning will be discussed. Performances of the two positioners will be tested in terms of their precision-positioning and load-carrying capabilities.

A systematic procedure for modeling, linearization, and multivariable optimal control of the two maglev positioners will be discussed in Chapter IV. The modeling and controller-design procedures are the same for both the positioners, except for the differences in their dimensional parameters. The equations of motion will be derived using the Euler-angle methodology and linearized about an operating point to derive state-space equations. The performance of this multivariable control will be analyzed and compared with that of six decoupled SISO controllers used earlier in Chapter III. The effect of adding the integrators to eliminate the steady-state error will also be addressed and the performance of the LQR controller with different weight matrices will be compared.

Another key objective of this research is to have a working space as large as the designed travel range itself, which implies that the performance of the positioner must be uniform throughout the working space. System identification is necessary in order to analyze and model the plant behavior accurately and to subsequently develop effective control strategies. It is also required to reduce the effect of unmodeled dynamics and nonlinearities in the actuators which may not be modeled precisely using analytical methods. The identification of the plant and coupling TFs for the Y-stage will be discussed in Chapter V. Closed-loop system identification techniques with known controller dynamics and a persistently excited signal will be used and an order-reduction algorithm will be described. Several test results will be presented to demonstrate the accuracy of the identified TF models.

Chapter VI addresses nanoscale path planning and motion control with the two maglev nanopositioners to test their performances when put in use for any practical applications such as μSTL, DPN, and scanning applications for imaging and manipulation of nanoscale surface phenomena. Motion trajectories of practical importance will be identified, along with the challenges in optimal path planning to meet the nanoscale motion-control objectives. Key control parameters in path planning will be determined, and control design methodologies will be proposed to satisfy the positioning requirements. The proposed methodologies, individually and collectively, will be implemented.

Finally in Chapter VII, three multiscale control schemes will be presented to meet the conflicting time-domain performance specifications: (1) a controller-switching technique that employs two controllers designed to meet two conflicting performance objectives and are switched in the course of operation, (2) an integral-reset scheme, which resets the integral term in the control law when a new reference point is reached, and (3) a reduced-order model-following approach, that uses a dynamic reference model with an objective to make the plant's output track the model's output as closely as possible. These control schemes will be analyzed in detail. Simulation and experimental verification of the proposed control methods will be presented. The three methods will be compared in terms of their dynamic and steady-state behavior and the ability to meet the desired objectives. In particular, the third method, being most effective among the three, will be analyzed in further details including closed-loop stability, initial state uncertainties, and input and output sensitivities.

Chapter VIII concludes this dissertation with a summary of significant achievements and contributions, and a list of suggestions for next few tasks which can be accomplished with the developed methodologies and further improvements in the performance of the two maglev positioners.

CHAPTER II

MAGLEV STAGE CHARACTERIZATION

2.1 Introduction

In this chapter, a detailed overview of the two maglev positioners is given. The developed maglev instruments are compared in terms of their characteristics and performance specifications. The underlying mechanical design and fabrication, electrical system setup, and elementary testing for the Δ-stage was done by Gu [61]. He also developed a use interface for the real-time control of the maglev positioners. Precision assembly for the Δ-stage and mechanical design, fabrication, and precision assembly for the Y-stage was done by Verma [62]. In this chapter, the mechanical design and sensing schemes of the two maglev positioners are revisited briefly. The need for developing a feedback linearization control scheme to reduce the effect of actuator nonlinearities in the large travel-range motion is also explained. Details of the design and experimental setup to characterize the behavior of nonlinearities and results of the feedback linearization are presented.

2.2 Δ and Y Maglev Positioners

Fig. 2.1(a) shows a photograph of the Δ-maglev stage. "Δ" refers to the shape of the single-moving levitated platen, which consists of a triangular aluminum part and six single-axis actuators [63, 64]. The compact maglev stage uses the minimum number of actuators required for 6-DOF motion. Each vertical actuator consists of a cylindrical magnet and a coil, and each

horizontal actuator consists of two cylindrical magnets and a coil. Prevailing precision positioning devices like STMs and AFMs are able to position in the travel range of 100 μm in 3 DOFs. However, this Δ-maglev stage is capable of motion control in all 6 DOFs with the travel ranges of 300 μm in the *x*-, *y*-, and *z*-translations and 3.5 mrad in the *x*-, *y*-, and *z*-rotations. The position resolution is better than 2 nm at 48-Hz control bandwidth for lateral motion control [9, 10, and 65].

Fig. 2.1(b) shows a photograph of the Y-maglev stage [66]. "Y" refers to the shape of the levitated single-moving platen. The Y-stage possesses several competitive advantages over the Δ-stage in terms of travel range, simplicity in mechanical design, and power consumption.

1. *Larger travel range*: This second-generation Y-stage has the planar travel range more than 15 times wider (5 × 5 mm) than that of the Δ-stage. Due to sensor specifications, this Y-stage is currently limited to move 500 μm in the *z*-axis and 3.5 mrad in rotation. However, the mechanical design of the stage makes it capable to rotate about 87.3 mrad (5°) and translate about 7 mm in *z* with appropriate sensors.
2. *Fewer components*: The Y-stage is based on a novel actuation mechanism in which forces in two perpendicular directions are generated by a single magnet (Refer to Section 2.3.2-B for details). This mechanism reduces the number of magnets three times compared to that in the Δ-stage.
3. *No mechanical restriction*: The platen of the Y-stage can be removed from the stage frame easily without disturbing any stationary parts. This facilitates easy loading and unloading of objects on the platen for various applications, which is an added advantage over the nanomanipulator developed by Culpepper and Anderson [67] and the Δ-stage [65].

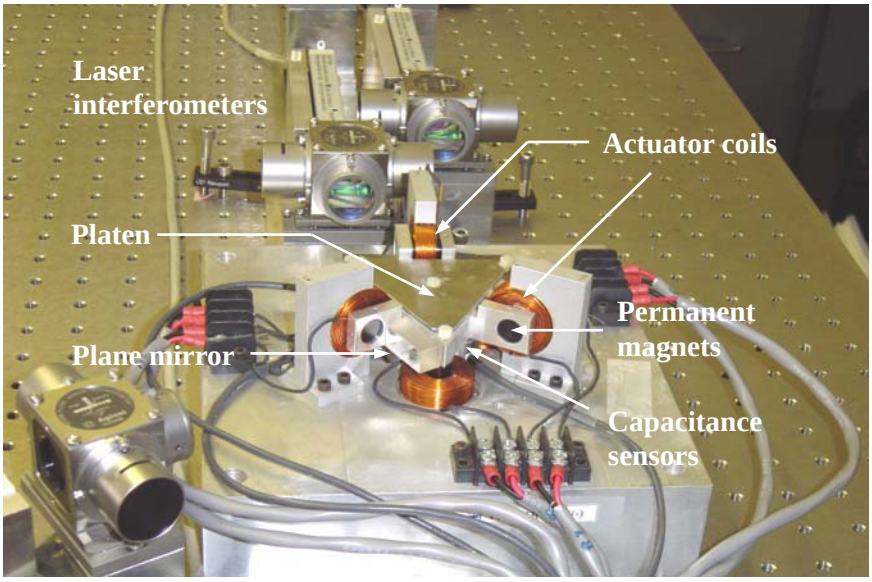

(a)

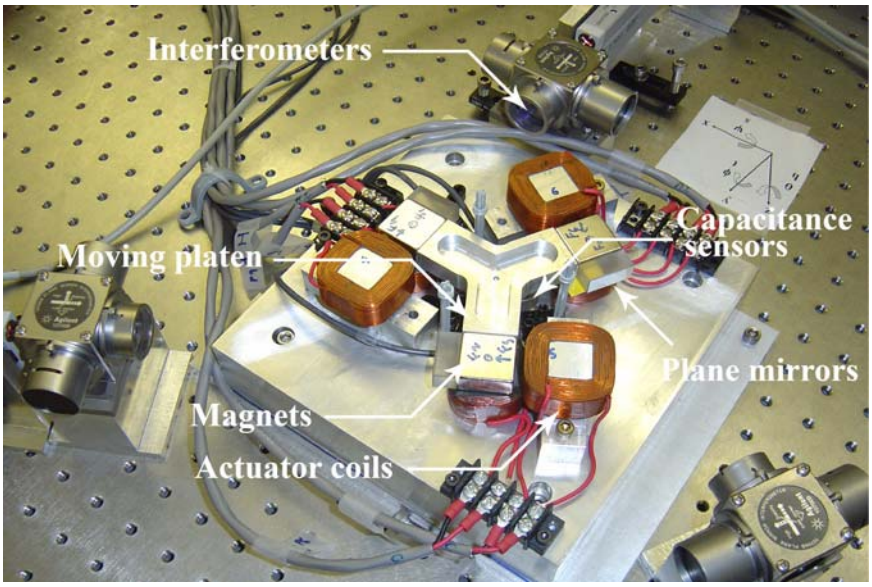

(b)

Fig. 2.1. Photographs of the (a) Δ-stage and (b) Y-stage showing major platen components, sensors and actuators

Table 2.1 summarizes and compares the specifications of the two maglev positioners in terms of their single-part moving elements, actuators, and motion capabilities.

Table 2.1. Summary of the two maglev-stage specifications

Property	**Δ-stage**	**Y-stage**	**Units**
Moving Elements			
DOFs	6	6	
Mass	0.212	0.267	kg
Size	80 × 69 × 17.5	115 × 127 × 12.7	mm
Actuation			
Number of coils	6	6	
Number of magnets	9	3	
Power consumption	1.0	0.8	W
Motion Capabilities			
Position resolution	2	3	nm
Travel range (translation)	0.3 × 0.3 × 0.5	5 × 5 × 0.5	mm
Travel range (rotation)	3.5 × 3.5 × 3.5	3.5 × 3.5 × 3.5	mrad
Maximum payload	0.3	0.2	kg

2.3 Mechanical Design

Fig. 2.1 shows different components of the two maglev positioners. The triangular part at the center in Fig. 2.1(a) and the Y-shaped part in Fig. 2.1(b) are the single-moving platens. The platens carry permanent magnets for actuation and plane mirrors for horizontal motion sensing. The details of the platen design and precision assembly are described in the following sections.

Effective packaging is important for any assembly. All parts were designed and assembled in such a way that (1) the platens must be close enough to all coils for sufficient force generation, (2) the bottom surfaces of the platens must be in the sensing range of all capacitance probes, and (3) the HeNe laser beams from the interferometers should not be blocked by other assembly components.

Since the platen is the only moving part in each of the two maglev stages, its design is very crucial with the following considerations: (1) the vertical actuators must continuously apply vertical forces to balance the platen's weight against gravity at a predetermined levitated height,

(2) the platen should be light in weight to maintain the coil currents in the actuators low, and (3) the moving and stationary structures should be stiff enough to exhibit a high natural frequency.

2.3.1 Platens

A. Platen for the Δ-Stage

The core of the platen is made of pocket-milled single-piece aluminum to reduce its mass and to keep its natural frequency high without sacrificing stiffness. There is no iron part in the assembly, which makes the actuators operable at high bandwidth without magnetic saturation or hysteresis. The parts attached to it are three horizontal magnet assemblies, three vertical magnet assemblies, three plane mirrors, and a set of aluminum, viscoelastic, and constraint layers on top. The assembly of these three layers adds passive damping to the system to minimize the structural vibrations and improve the stability. The bottommost aluminum layer, called the top plate, covers the pockets of the platen. It was attached to the platen using four screws, three at the corners and the fourth at the center. The total mass of the moving part is 0.212 kg.

The horizontal and vertical actuator assemblies will be described in details in the next subsection. There are three arms protruded on the sides of the platen to hold the magnet assemblies for horizontal actuation. Since the magnetization directions of the magnets are parallel to the sides of the triangular platen, these units generate horizontal force parallel to the sides of the platen. Each of the three vertical actuator assemblies consists of a cylindrical magnet and a cylindrical aluminum mount with three holes potted together. Each assembly is mounted on the platen using three set-screws.

Three plane mirrors were mounted on the platen for horizontal motion sensing. These plane mirrors act as the reflectors for the laser interferometers. The bottom surface of the platen was machined and ground to be flat within 2.54 μm as this surface would be used as the target by the capacitance gauges to sense the vertical displacements of the platen.

B. Platen for the Y-Stage

The platen core was machined from single-piece aircraft-grade 7075 aluminum. It was pocket-milled in the center leaving the ribs on the edge to reduce the weight while keeping the high stiffness and natural frequency. The three ends of the Y-shaped platen core have a width of 25.4 mm and a height of 12.7 mm to match the side dimensions of the magnet. A small hole was drilled and tapped in the center of platen for a screw to hold a grounding wire for the capacitance gauges. The bottom surface of this Y-platen was also ground to achieve a surface roughness of 2.54 μm like that of the Δ-stage. The three cuboid-shaped permanent magnets were attached at the three ends of the platen core with the square faces on the top and bottom being the N and S poles, respectively. Three plane mirrors were then attached at one of the side faces of the magnets for horizontal motion sensing.

2.3.2 Actuators

A. Actuator Units for Δ-Stage

The six-axis motion generation by the platen for the Δ-stage is achieved by the application of a combination of independent force components acting through six unit actuators. Each horizontal-actuator unit consists of two cylindrical permanent magnets attached together with an aluminum spacer between them placed inside a doughnut-shape current-carrying coil.

Each vertical-actuator unit consists of one permanent magnet and a current-carrying coil identical to those in a horizontal-actuator unit. The assembly of the magnets and spacer is attached to the moving platen, while the six current-carrying coils are fixed to the stationary base plate.

Schematics of the assemblies of the horizontal and vertical actuators are shown in Fig. 2.2. The coil generates the N or S pole based on the direction of the current governed by the right-hand rule. Depending on its magnetization direction, an attractive or repulsive force is applied on the magnet. A magnet-coil air gap of 504 μm limits the total achievable travel range of the platen.

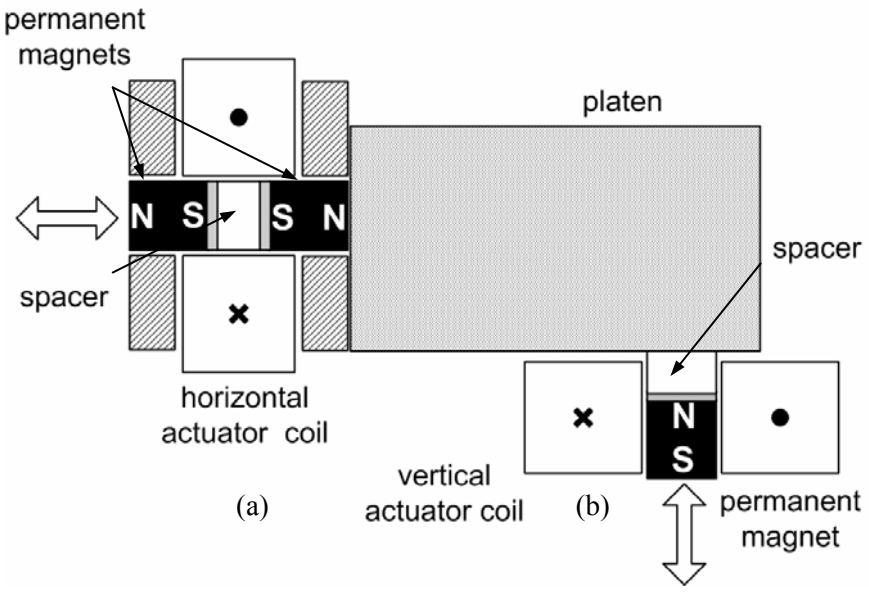

Fig. 2.2. Schematics of (a) the horizontal-actuator unit and (b) the vertical-actuator unit for the Δ-stage

The primary benefit of this maglev stage apart from its precision positioning and load-carrying capabilities is the nominal power consumption by the actuators. The average nominal

current in each vertical actuator is 0.7 A, so the power consumption with the coil resistance of 0.6 Ω is only around 1 W in the entire actuation system to levitate the platen against gravity. Assuming the coils to be point sources of heat, this power consumption would increase the temperature of the base plate by a maximum of 0.2°C. Furthermore, this heat is transferred to the platen only through convection since there is no mechanical contact between the base plate and the platen. Since this maglev stage is intended to be used as a nanopositioner, even small changes in the dimensions due to thermal expansion may be significantly detrimental. The small power consumption leads to lesser heat generation and thermal-expansion error due to Joule losses. Hence, a consistent and repeatable positioning performance can be ensured. Thus for all practical purposes, the thermal expansion errors due to heat losses may be safely ignored. The characterization of these actuators was described in detail in [63]. The detailed specifications of the actuating units in the Δ-stage are given in Table 2.2.

Table 2.2. Properties of the actuators

	Property	**Δ-stage**	**Y-stage**	**Units**
Permanent magnet	Size	Ø 11.7	25.4 × 25.4	mm
	Height	9.5	12.7	mm
	Material	NdFeB	NdFeB	-
	Energy product	400	280	kJ/m^3
Coil	Wire gauge	AWG#24	AWG#24	-
	Material	Copper	Copper	-
	Turns	179	679^V 561^H	-
	Resistance	0.6	5.5^V 5.9^H	Ω
	Inner dimension	Ø 12.2	10×10^V 20×20^H	mm
	Outer dimension	Ø 32.5	35×35^V 40×40^H	mm
	Thickness	9.6	17.5	mm

V: Vertical actuator
H: Horizontal actuator

B. Actuator Units for Y-Stage

The working of the Y-stage is based on a novel 2-axis electromagnetic-force generation scheme, which generates forces on a single permanent magnet in two perpendicular directions using a horizontal and a vertical current-carrying coil [66]. The terms "vertical coil" and "horizontal coil" are used to designate the coils which generate vertical and horizontal actuation, respectively. Fig. 2.3 shows a cross-sectional view of each actuator unit. The maglev stage is comprised of three such actuating units with three permanent magnets attached to ends of the Y-shaped platen and two fixed square-shaped coils per magnet as shown in Fig. 2.1(b). The magnetic-field lines generated by the permanent magnet are also shown in Fig. 2.3. The directions of the currents in flow are assumed clockwise in the vertical coil and counterclockwise in the horizontal coil, seen from the top.

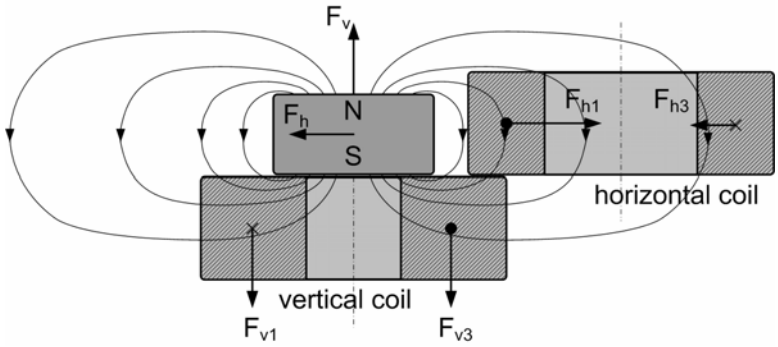

Fig. 2.3. Cross-sectional view of the novel two-axis actuator used in the Y-stage [66]

The magnetic flux generated by the magnet is shared by the two coils, one right below and another on the side of the magnet. The magnitude and directions of currents in the coils govern the forces exerted on the magnet following the Lorentz-force law. In the vertical coil, the direction of the magnetic-field lines is normal to the direction of current flow and towards the center of the coil on all the four sides of the coil (neglecting the corner effect). Thus the $\boldsymbol{J} \times \boldsymbol{B}$

Lorentz force on the coil is vertically downwards on all the four sides of the square. The equal electromagnetic reaction force is applied vertically upwards on the moving magnet since the coil is fixed in a stationary frame. Similarly, in the horizontal coil the direction of the magnetic-field lines is approximately downwards in all the four sides. Thus, the effective force on the coil is to the right following the right-hand rule, and on the magnet, to the left. To change the magnitude and directions of the vertical and horizontal forces, appropriate changes are made in the magnitude and directions of current flow in the corresponding coils. In this manner the forces can be generated in the two perpendicular directions independently on a single moving magnet. The detailed specifications of the actuating units in the Y-stage are given in Table 2.2.

While it retains all the advantages of the Δ-stage as regards the precision-positioning and load-carrying capabilities and nominal power consumption, the Y-stage also exhibits several additional benefits over its first generation counterpart owing to this new actuation scheme. (1) It makes the mechanical design of the maglev stage very simple to manufacture and assemble, (2) there is no mechanical constraint on the platen to separate it from the actuator assembly, and (3) since there are only three magnets used to generate actuation forces in all the six directions, the structure of the platen is simple.

2.4 Sensing

2.4.1 Laser Interferometry

The horizontal-plane position and velocity sensing for real-time control is done by laser interferometer system from Agilent shown in the Fig. 2.4. The laser interferometer metrology arrangement for the Y-stage is shown in the Fig. 2.5. The arrangement is similar for the Δ-stage with the only exception in the placement of the mirrors on the platen. It has two mirrors placed

on one side and the third one on another side 60° apart. The interferometer arrangement is also modified accordingly.

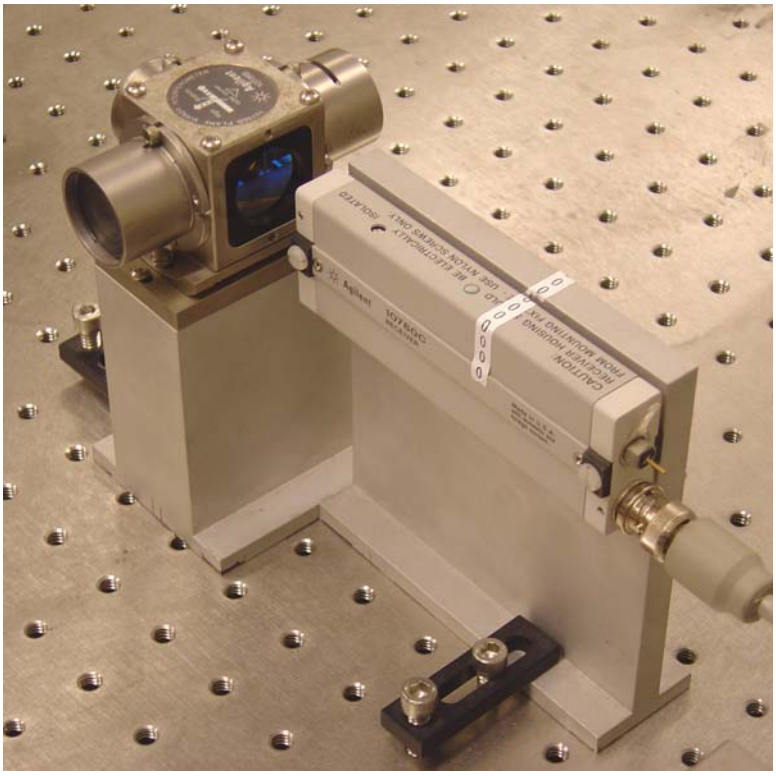

Fig. 2.4. Laser interferometer and receiver for horizontal motion sensing

The primary components of this interferometry system are He-Ne laser head (5517D), three plane interferometers (10706B), three receivers (10780C), three laser axis boards (10897B) for *x*- and *y*-translation and *z*-axis rotation, a 33% beam splitter (10706A), a 50% beam splitter (10701A), a beam bender (10707A), and two plane mirrors for non-orthogonal beam-bending. The laser head is the source of orthogonally polarized HeNe laser at a wavelength of 632.99 nm. The beam power output is 180 μW – 1 mW. The beam from laser head is distributed into three parts of equal intensity using beam-splitters and directed by beam benders and mirrors so that

each beam falls normally on the platen mirrors. The receiver senses the reflected beams from mirrors and transmits the data to the laser-axis boards, which provide position and velocity information. The laser axis board gives 35-bit position data at a 10-MHz refresh rate. It also provides 24-bit velocity data. This is an added benefit since differentiating position data to get velocity is usually troublesome due to the high-frequency noise present in the sensed data.

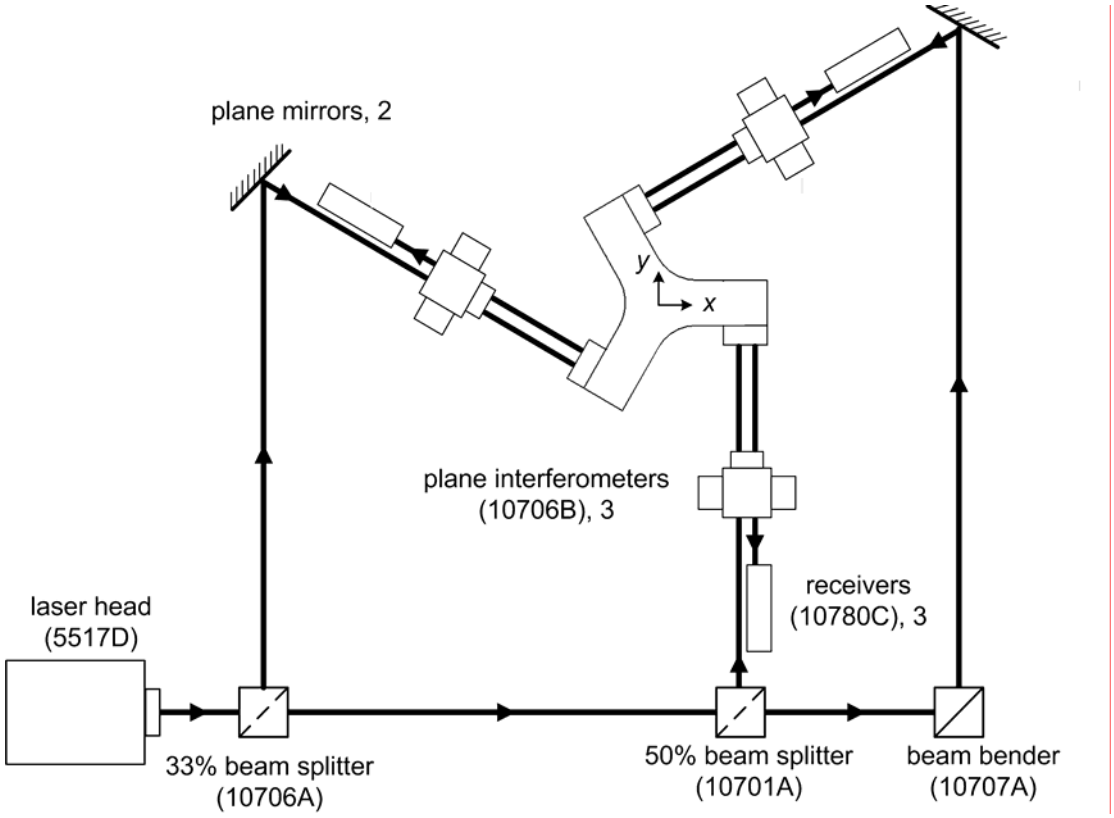

Fig. 2.5. Interferometry system for the Y-stage [62]

The schematic of the high-stability plane-mirror interferometry is shown in the Fig. 2.6. This interferometer uses the dual-pass method and provides 0.6-nm resolution over a travel range of 40 m. The incident beam consists of a measurement beam and a reference beam with orthogonal polarizations. The reference beam gets internally reflected from the interferometer

and received by the laser receiver. The measurement beam falls normally on to the plane mirror mounted on the platen after one internal reflection through the interferometer and the mirror, gets received by the laser receiver. The optical path length changes by twice the amount the plane mirror moves [68]. Since the measurement beam and the reference beam have a common path, the thermal expansion of the interferometer optics causes the thermal measurement drift of up to 12 times less compared to the value typically achieved by conventional plane mirror interferometers, hence the term high-stability [69]. The maximum velocity that this interferometer can sense is 0.5 m/s. The laser interferometric position sensing system gives only relative position data with respect to an initial position. This requires initial position adjustment and subsequent initialization of the position data.

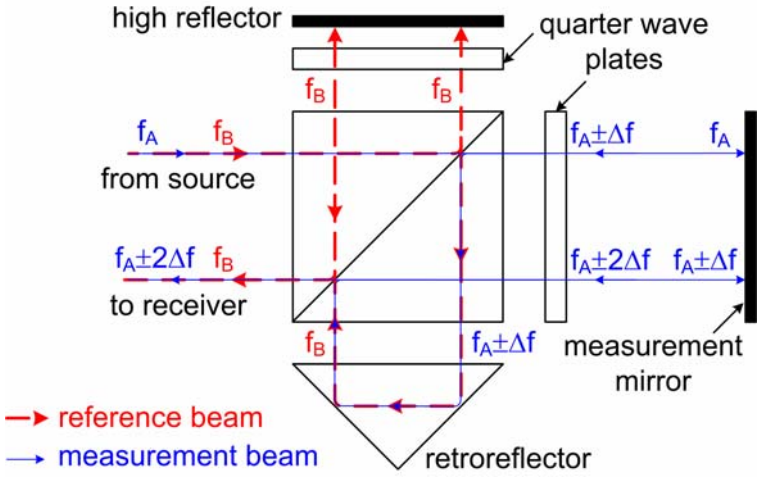

Fig. 2.6. Schematic showing working principle of high-stability plane-mirror interferometer system [69]

2.4.2 Capacitance Probes

Three capacitance probes from ADE (2810), facing the bottom surface of the platens, were used for vertical position sensing as shown in the Fig. 2.7. The linear sensing range of these

probes is around 500 μm in a gap of 250 μm to 750 μm between the probe and the target surface. These probes have outer diameter and height of 20 mm and 18 mm, respectively, with a 10-mm active sensing area. Each probe measures probe-to-target distance by sensing the change in the capacitance between the two surfaces and converting it to a voltage signal. The outputs of the three probes are fed to the signal conditioning boards (ADE 3800), placed in the VME chassis. These ADE 3800 boards provide the analog signals with an output range of ±5.0 V. These boards have jumper settings and can change the output voltage swing.

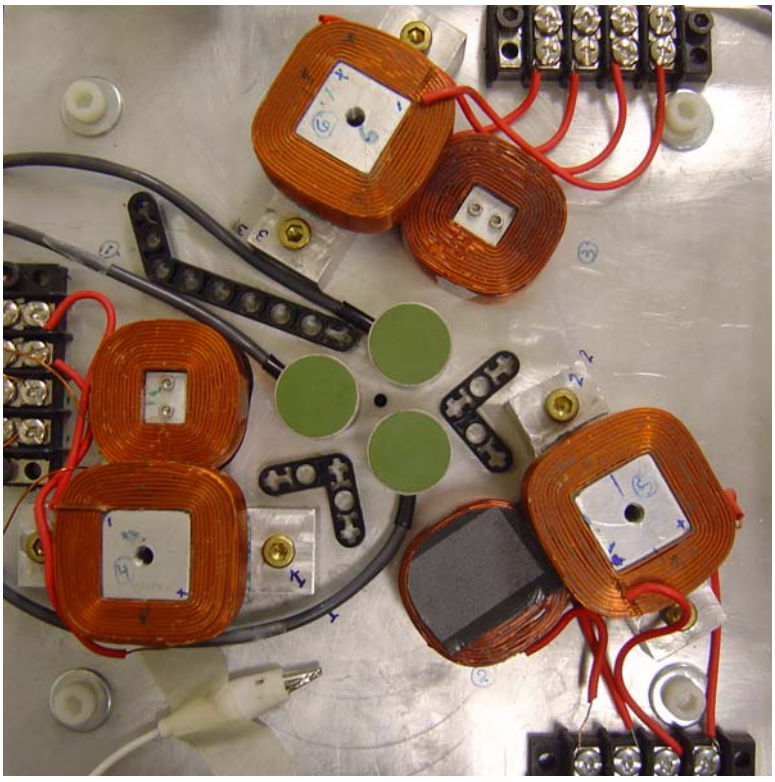

Fig. 2.7. Capacitance gauges for vertical motion sensing

The analog signals are sampled and converted to digital data using 16-bit ADCs on Pentek 6102. Actual position and rotation values for *z*-translation and *x*- and *y*-axis rotation for

real-time digital control are obtained from this data using triangulation method. In order to avoid the aliasing of the sensor signals by higher-frequency noise contents, a set of first-order RC anti-aliasing filters are used right before sampling by the ADCs. The bandwidth of the ADE 3800 systems is set at 1 kHz. Typical noise amplitude in the probe information is 50 nm peak-to-peak or more due to the noise in the Pentek ADC card. ADE recommends grounding the target, i.e., the platen, to reduce noise, so a wire attached to the platen was used to do this.

2.4.3 Instrumentation Structure

The schematic of instrumentation structure is shown in the Fig. 2.8 and is common to both the maglev positioners. The primary components of instrumentation are a Versa Module Eurocard (VME) PC (VMIC 7751), a digital signal processor (DSP) board (Pentek 4284), a 16-bit data-acquisition board (Pentek 6102), and 3 laser-axis boards (Agilent 10897B). A VME chassis is used as a communication backbone among various instrumentation components. Details of these vital instrumentation components are given below.

A. DSP Board (Pentek 4284)

The Pentek 4284 board with a TMS320C40 DSP is employed for the all the foreground computing tasks in real-time control. It takes position and velocity inputs from the 10897B laser-axis boards and Pentek 6102 data-acquisition board, user commands or predefined positions and trajectories from VME PC, samples the data, applies the control law, and generates the output commands via 16-bit digital-to-analog converters (DACs), also available on the data-acquisition board. All these tasks are accomplished in an interrupt service routine (ISR) called by an external interrupt every 200 μs.

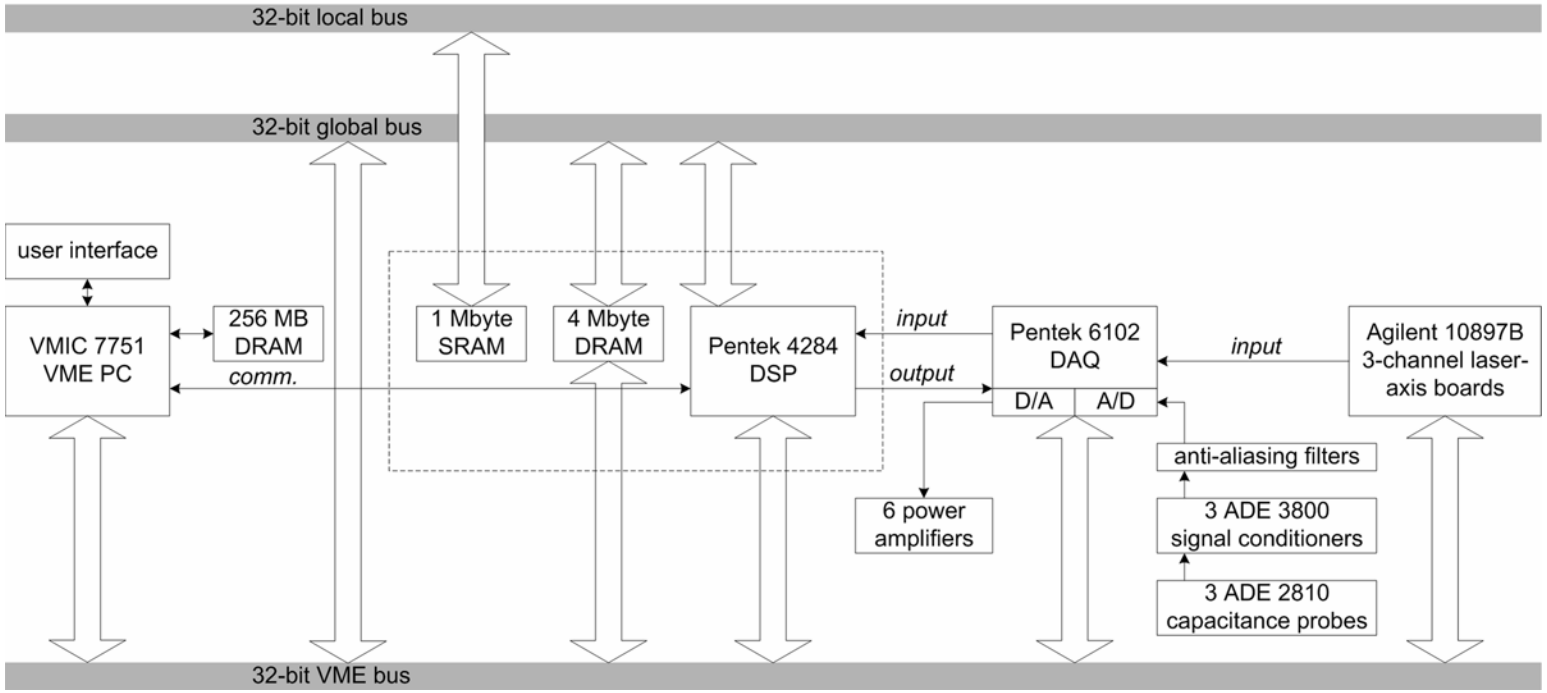

Fig. 2.8. Schematic of the instrumentation for the two maglev positioners

B. Data-Acquisition Board (Pentek 6102)

The data-acquisition board contains 8 channels of 16-bit ADCs and 8 channels of 16-bit DACs with input/output (I/O) range of ±5 V. The 10-MHz 35-bit position and 24-bit velocity data from the laser axes board is received by the DSP via the VME bus. For vertical position sensing, 3 capacitance sensing probes (ADE 2810) with signal conditioning boards (ADE 3800) are used. The analog outputs of these boards are fed to a data-acquisition board on VME chassis after a 1-kHz low-pass anti-aliasing filter.

C. Power Amplifiers

The control outputs indicating desired coil currents are fed to transconductance amplifiers via the DAC. The output current from an amplifier is linearly proportional to the input voltage. Each amplifier consists of a differential amplifier to reject common-mode noise, a feedback amplifier to stabilize the current-control loop, and a power booster with a power operational amplifier (PA12A) by Apex. The output of amplifier causes flow of desired current in the coils for electromagnetic actuation. The output swing of the DACs is ±5V and the current limit in the coils is set at ±2.5 A.

D. VME PC

The VME PC is used to compile the C codes and download the executable file to the DSP. This VMIC 7751 VME PC has a Pentium III 733-MHz processor and 256 MB of RAM on it. Additionally, it has Swiftnet, Code Composer, Visual Studio, and a custom-designed user interface to operate the maglev positioners. Swiftnet is a software by Pentek that acts as a controller panel interface between the VME PC and the DSP board. It is a mandatory program to

run the PC for continuous communication for real-time commands while the stage is in operation. The Code Composer by Texas Instruments is used to compile the projects written in C language and link them to generate a DSP-executable code. The compiled code can be downloaded to the DSP via Swiftnet.

E. User Interface

The user interface is a graphical user interface (GUI) developed by Gu [61], one of Dr. Kim's former graduate students, that interacts with the DSP for real time position inputs and trajectory-tracking during the operation. This communication between the DSP and the VME PC is established via a dual-port memory on the Pentek 4284 board. Primary functions of the user interface are listed below.

1. It sends the user-defined reference input commands to the DSP. These commands include steps in single or multiple axes, and predefined trajectories.
2. It sends system commands for initializing DSP and ADC and DAC boards, and setting initial reference values for the laser interferometer sensors.
3. It displays the positioner's status in real time. This includes input reference positions in 6 axes, actual measured position values from the sensors, position errors, and calculated coil currents and the actuator forces for the 6 actuating coils.
4. It snaps and records the data whenever required by the user in a text file for plotting and/or further analyses.

2.5 Feedback Linearization of Actuation Forces

While modeling the actuators initially, we assumed that the force applied by the electromagnetic actuators was related to the coil current with a nominal force constant and not a function of position. However, if the translation of the permanent magnet is large, this current-to-force conversion factor is no longer constant. This is not a problem for the Δ-stage since the total travel range is limited by the gap between the coil and the permanent magnet to 300 μm. In this range, the force-gap relationship remains linear and the force constant may be assumed constant. However, for the Y-stage, there is mo such mechanical constraint. The packaging of actuator units allows the travel range to be as large as 5 mm × 5 mm and hence, the force-gap relation is expected to be a nonlinear one.

The nonlinear relations between force and coil-magnet gap for horizontal and vertical actuators were identified experimentally. The experimental setup is shown in Fig. 2.9. The magnet was fixed on one end of a precision load cell. The other end of the load cell was attached to a $xyz\phi$ manual positioning stage. The magnet was positioned in the 3 axes using the micrometers on the stage with respect to the coils at different positions and measured the load-cell voltage output. The load cell was calibrated by subtracting the offset forces due to gravity with zero coil-current. The forces due to magnetic attraction with optical table and bolts etc. were also identified using a known load and the load-cell reading was adjusted accordingly. The forces generated by the vertical and horizontal actuators as a function of the distance between the coil and the permanent magnet are shown in Fig. 2.10(a) and (b), respectively. Evidently, the forces are nonlinear functions of the gap as expected.

For a nonlinear system, controllers based on a linearized model at an operating point are only effective in a small neighborhood around that point. Out of this neighborhood the system performance often degrades rapidly. Two approaches to the problem of ensuring consistent

performance independent of the operating point have been reported in literature. One approach is the gain scheduling [70] where the nonlinear force-gap relationship of the electromagnetic actuation is successively linearized at various operating points with a suitable controller designed for each of these operating points. To ensure long travel ranges and still obtain good tracking performance, gain-scheduling controllers require the entire operating range to be broken into fine intervals and stored in large lookup tables of controller gains.

An alternative to the gain scheduling approach is feedback linearization [71]. The approach can algebraically transform a nonlinear system dynamics into a linear one, based on which linear control design methods can be applied. Feedback linearization has been proved to be a very successful technique for such systems [72, 73, and 74]. French and Rogers used the approximate parameterization for adaptive feedback linearization [72]. Approximate state-feedback linearization using spline functions was applied by Bortoff for single-input nonlinear systems [74]. A rotating inverted pendulum was used to demonstrate the improved performance.

A similar approach was used to compensate for the nonlinearity of the maglev system. The calculation of the desired current to generate a particular force based on a quintuple integration [9] cannot be performed in real time because the force calculation evaluating the quintuple integrals is a very time-consuming process. Therefore I calculated the force at several points offline and used these values to estimate the force at other points. I used the "basic fitting" function in MATLAB to find an approximate second-order polynomial function that is closest to the experimental value. Fig. 2.10(a) (dashed line with circles) shows the experimental vertical force of the actuator with a 1-A coil current, and the approximate quadratic polynomial curve is given by

$$K_v = 4.7418 \times 10^4 g_v^{\,2} - 8.7132 \times 10^2 g_v + 6.7712 \qquad (2.1)$$

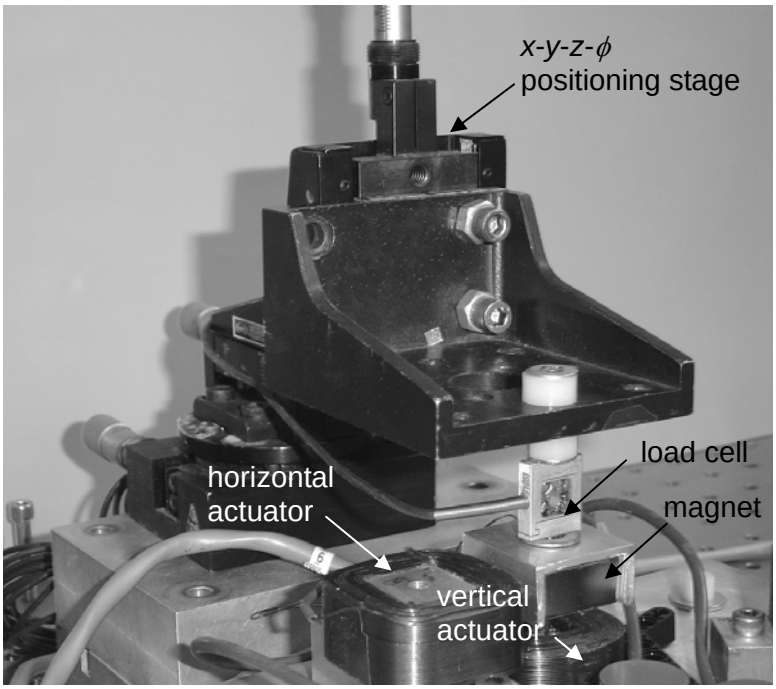

Fig. 2.9. Experimental setup to determine the force-gap relationship for vertical and horizontal actuators

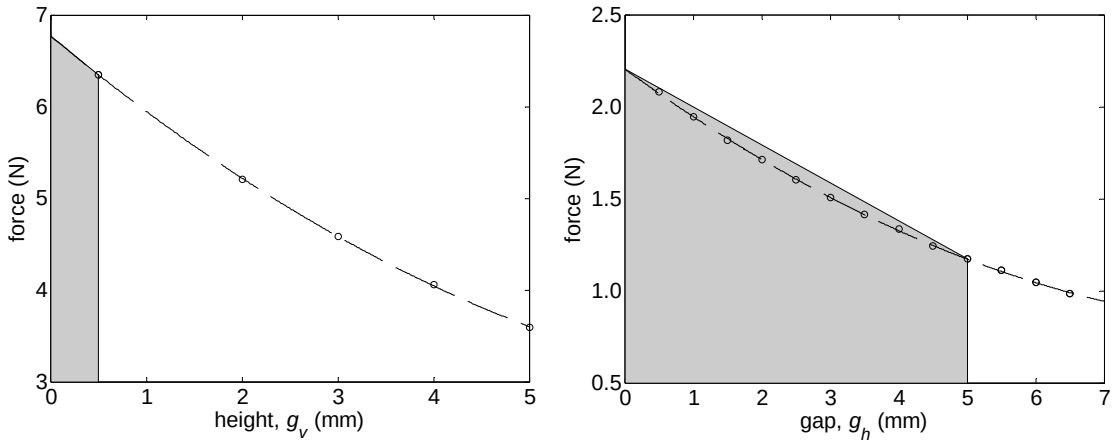

(a) (b)

Fig. 2.10. Experimentally determined values of force (o), quadratic fit (dashed line), and operating range (shaded region) to determine the force-gap relationship for (a) vertical and (b) horizontal actuators for a 1-A current

where g_v is the levitation gap [m] between the magnet and the top surface of the coil and K_v is a nonlinear current-to-force conversion factor [N/A] in the vertical actuator. Similarly for the horizontal actuation, I calculated forces from the actuator at different horizontal gaps (g_h) between the coil and the magnet with the 1-A coil current. Fig. 2.10(b) (dashed line with circles) shows the experimental horizontal force at several gaps [m] with the 1-A coil current, and the approximate quadratic polynomial fit is given by

$$K_h = 1.3031 \times 10^4 g_h^{\,2} - 2.7161 \times 10^2 g_h + 2.2050 \tag{2.2}$$

where K_h is a nonlinear current-to-force conversion factor [N/A] in the horizontal actuator. Fig. 2.10 also shows the operating regions for the two actuators. For vertical actuation, the travel range is limited by the sensing range of capacitance gauges to 500 μm. In this small operating range, the force constant may be assumed constant. However, we do need feedback linearization for horizontal motion control where the travel range may be as large as 5 mm. Feedback linearization would also be needed for vertical motion control if we use the extended range motion sensors.

The plant dynamics can now be modeled for horizontal motion control in the following nonlinear form.

$$\begin{aligned} \dot{\boldsymbol{x}}_1 &= \boldsymbol{x}_2 \\ \dot{\boldsymbol{x}}_2 &= \frac{1}{m} f(\boldsymbol{x}_1)\boldsymbol{u} \end{aligned} \tag{2.3}$$

where $\boldsymbol{x}_1$ is the position vector, $\boldsymbol{x}_2$ is the velocity vector, m is the mass of the platen, and $\boldsymbol{u}$ is the coil current vector. $f(\boldsymbol{x}_1)$ consists of the modal force transformation matrix and the current-to-force conversion factors. Since the complete information on the force-gap relationship is available, the plant input $\boldsymbol{u}$ can be chosen as

$$\boldsymbol{u} = \left[f(\boldsymbol{x}_1) \right]^{-1} \boldsymbol{v} \tag{2.4}$$

to cancel the nonlinear term. The vector $\boldsymbol{v}$ in (2.4) is the control efforts from the linear controllers in the form of force [N]. This cancellation results in the following linear dynamic equation of motion.

$$\begin{aligned} \dot{\boldsymbol{x}}_1 &= \boldsymbol{x}_2 \\ \dot{\boldsymbol{x}}_2 &= \frac{1}{m}\boldsymbol{v} \end{aligned} \tag{2.5}$$

This feedback linearization utilizes the complete nonlinear description of the electromagnetic force and hence yields consistent performance largely independent of operating points. The block diagram shown in Fig. 2.11 represents the implementation of this feedback linearization approach through nonlinear compensation. The feedback linearization equations were implemented in a real-time C code to calculate the desired coil currents for a given value of force and position.

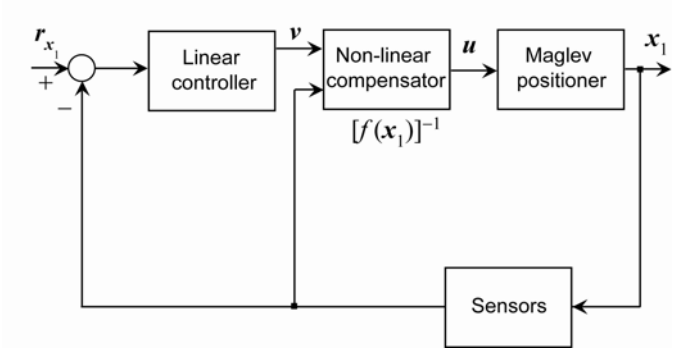

Fig. 2.11. Block diagram representing the feedback linearization through nonlinear compensation

Fig. 2.12(a) shows the experimental result of position regulation in x. Position resolution is clearly better than 3 nm. Fig. 2.12(b), (c), and (d), respectively show the response of the maglev stage to a reference step command of 5 mm in x and the perturbations in the other two

axes, namely y and ϕ (rotation about z) with and without using feedback linearization. As can be seen in Fig. 2.12(b), the overshoot decreased from 21.3% to 12.9% with feedback linearization.

Feedback linearization also helps in reducing the effect of the stray torques acting on the levitated platen. These stray torques appear mainly due to the force imbalance when the magnet is substantially away from an operating point. They also come due to the difference in the plane of application of forces and center of mass (CM) of the platen. This will be discussed in further details in Section 3.1. Furthermore, in the absence of feedback linearization, the controller would keep applying equal current to all the three horizontal and vertical actuators. Due to the difference in the gap in individual coil-magnet pairs, however, the actual forces acting on the magnets would be different. This would result in an imbalance in the net force acting on the three magnets and there would be a net moment on the maglev platen. Other sources of stray torques include the asymmetry in the stage structure due to mirrors and other assembly errors. Feedback linearization is again capable of effectively mitigating this problem since it uses the actual position feedback to calculate the required current. Fig. 2.12(b) and (c) show that there were significant deviations from the commanded regulatory positions of y and ϕ if a constant force constant was used. Feedback linearization reduced this perturbation significantly.

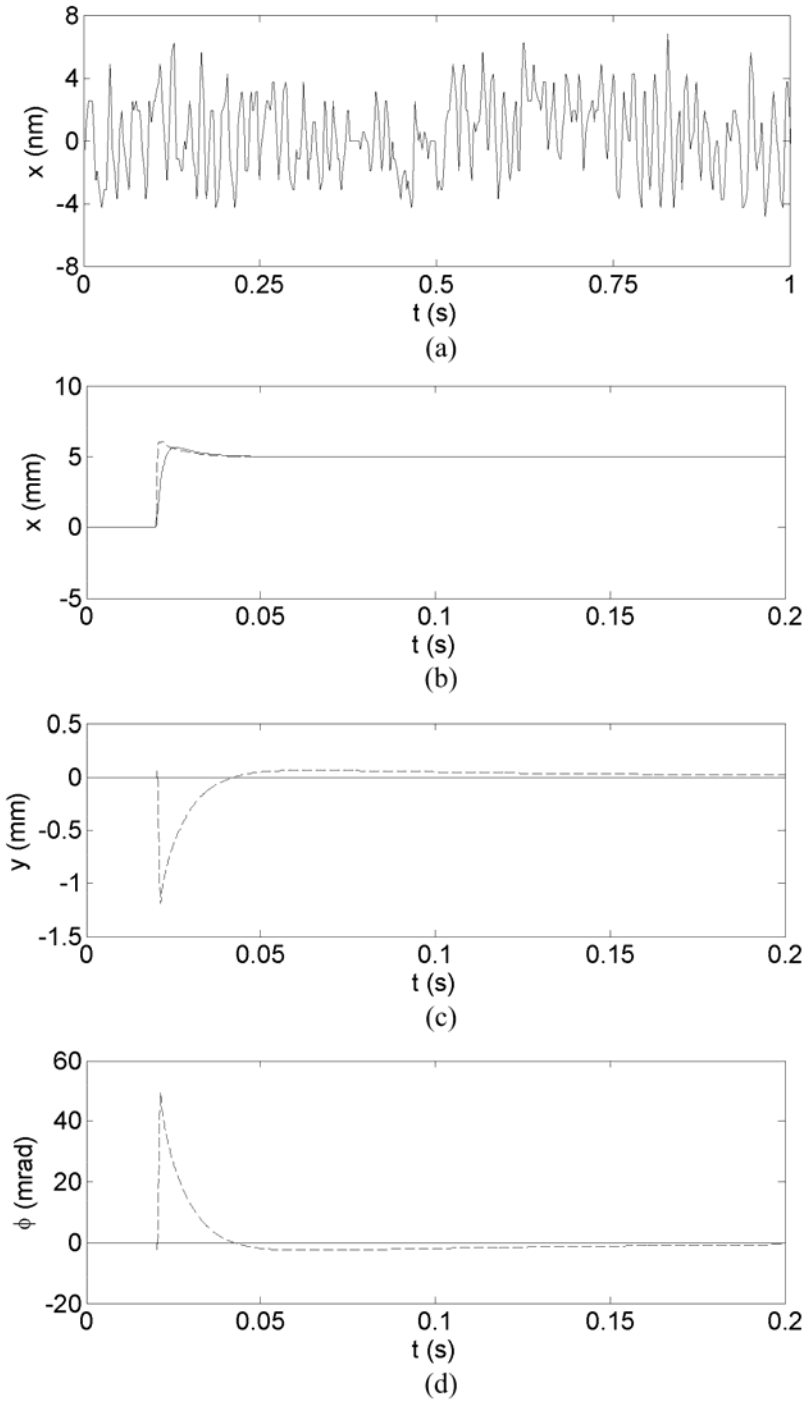

Fig. 2.12. (a) Position regulation in x. (b) Response of the maglev stage to a reference step command of 5 mm in x and perturbations in (c) y and (d) ϕ with (solid line) and without (dashed line) feedback linearization

CHAPTER III

PRELIMINARY ANALYSIS AND TEST RESULTS

In this chapter, the plant modeling, control and testing results for the two maglev positioners are discussed. These results are based on decoupled SISO plant models with pure-mass assumption. Accordingly, six individual controllers will be used for preliminary performance testing. The limitations of these assumptions and simplified models will be analyzed, and motivation for developing advanced control schemes and motion planning will be discussed. Performance of the two positioners will be tested in terms of their precision positioning and load carrying capabilities. With the results and motivations presented in this chapter, I will pursue further developments on the maglev systems in order to be able to use them for commercial applications.

3.1 Dynamic Modeling and SISO PID control

3.1.1 6-DOF Force Generation

The actuation schemes of the two maglev positioners were discussed in the previous chapter. Both the stages use six linear actuators to generate 6-DOF motion, namely translations in x, y, and z and rotations about these axes, through appropriate combination of forces. Fig. 3.1(a) and (b) respectively show the directions of forces generated by each of the linear actuators in the two stages and the axis conventions.

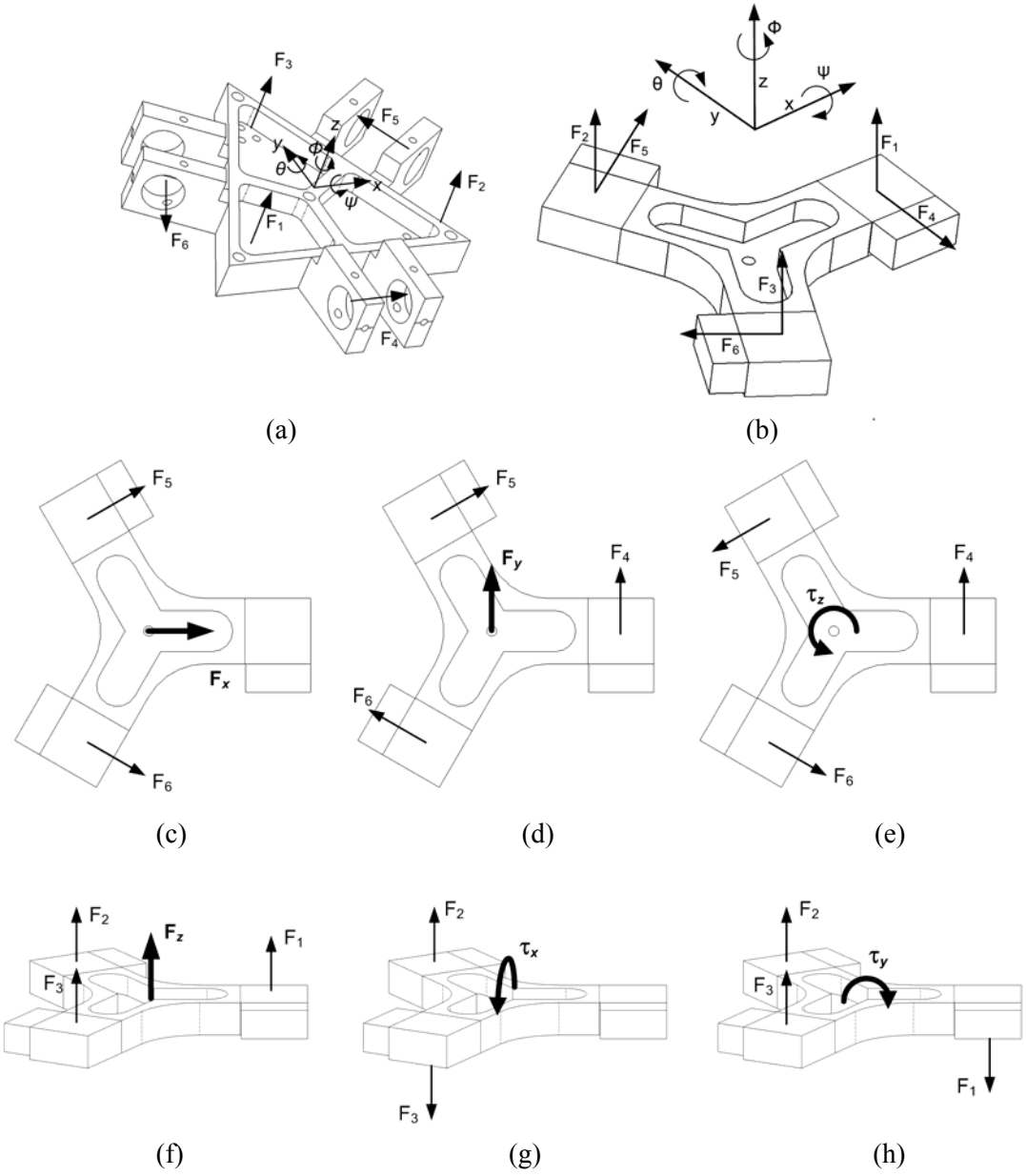

Fig. 3.1. Convention of the coordinate axes and the directions of forces generated by the unit linear actuators for (a) the Δ-stage and (b) the Y-stage. (c–h) Force generation using a combination of six actuator forces

The conceptual modal force generation of the maglev system is depicted in Fig. 3.1(c–h), taking example of the Y-stage. Fig. 3.1(c), for instance, shows the directions of forces F_5 and F_6

to get an effective force in the x axis. Likewise, Fig. 3.1(d) depicts the force generation in the y-axis using a combination of F_4 in negative direction, and equal values of F_5 and F_6 in positive directions, so that the x components of F_5 and F_6 are cancelled. For rotation about z the three horizontal forces F_4, F_5 and F_6 are applied in positive directions. In this way, by combination of these three horizontal forces, we achieve planar horizontal motion. Similarly, for vertical motion, suitable combinations of the three vertical forces F_1, F_2 and F_3 give translation in z and rotations about x and y as shown in Fig. 3.1(f–h).

3.1.2 Analytical Plant Modeling

A. Mass and Inertia Tensors

The mass m of the platen assembly was measured using a precision electronic balance. The total mass of the moving part for Δ-stage includes the platen, mirrors, vertical magnets, horizontal magnets, cover layer, damping layer, constraint layer, spacers, and screws. The structure of the Y-stage was relatively simple and the platen mass consists only of the Y-shaped aluminum core, three permanent magnets and three plane mirrors. The three permanent magnets contribute nearly 73% of the total platen weight. Other system parameters like CM, inertia matrix, and natural frequencies, were determined using a finite element (FE) model in SolidWorks. Details of these calculations are reported in [61]. Here I present the final values of mass and moment of inertia at the CM of the two stages in Table 3.1. The definition of each axis is shown in Fig. 3.1.

For the Δ-stage, the off-diagonal terms are non-zero. This is due to asymmetry because of the mirrors. However, the products of inertia are less than 3% of the principal moments of inertia, and hence, they are neglected in the preliminary analysis. The Y-stage, on the other hand,

has more symmetrical structure due to the innovative design of the moving platen. Thus, the ideal SolidWorks model does not yield any off-diagonal terms and for preliminary analysis, the platen motion may be assumed decoupled in 6 DOFs [62]. It is to be noted, however, that the system does have coupling terms, as I will demonstrate in the Section 3.2.3. These coupling terms may be due to errors in the precision assembly of the platen components. In the Chapter V, closed-loop system identification will be used in order to identify these coupling terms in the form of transfer function.

Table 3.1. Mass and moment of inertia for the two stages

Property	**Δ-stage**	**Y-stage**
Mass (kg)	0.2126	0.2670
Moment of inertia $\begin{bmatrix} I_{xx} & I_{xy} & I_{xz} \\ I_{yx} & I_{yy} & I_{yz} \\ I_{zx} & I_{zy} & I_{zz} \end{bmatrix} \times 10^{-6}$ kg.m^2	$\begin{bmatrix} 132.88 & -3.14 & 0 \\ -3.14 & 122.28 & 0 \\ 0 & 0 & 235.87 \end{bmatrix}$	$\begin{bmatrix} 340.37 & 0 & 0 \\ 0 & 340.37 & 0 \\ 0 & 0 & 653.61 \end{bmatrix}$

B. Plant TF Models

In the absence of any mechanical contact between platen and the stationary parts, the analysis may be simplified by assuming that spring and damping effects are negligible. Accordingly, we model the plant as a pure mass. From Newton's second law, the equation of motion for *x*-translation is given by

$$m\ddot{\tilde{x}}(t) = \tilde{f}_x(t) \tag{3.1}$$

where $\tilde{x}(t)$ is the perturbation of position of the platen in *x* from the operating point and $\tilde{f}_x(t)$ is the modal force required in *x* to regulate its position. Subsequently, for vertical motion, $\tilde{f}_z(t)$

refers to the actuator forces subtracted by the platen weight. Similarly, for rotation about *x*, the equation of motion is given by

$$I_{xx}\ddot{\tilde{\psi}}(t) = \tilde{\tau}_{\psi}(t) \tag{3.2}$$

where $\tilde{\psi}(t)$ is the perturbation of angular position of the platen about *x* from its operating point and $\tilde{\tau}_{\psi}(t)$ is the modal torque required about *x* to regulate its position. The open-loop plant transfer functions are, therefore, given by

$$G_{xx}(s) = \frac{\tilde{X}(s)}{\tilde{F}_X(s)} = \frac{1}{ms^2} \tag{3.3}$$

and so on.

This simplified plant model is good enough for testing and preliminary analysis. However, as we will see in the subsequent chapters, a double-integrator model like this poses several challenges in the advanced controller design. One such problem is a non-invertible system matrix in the state-space notation. System response, on the other hand, also gives some unexpected results. Since the integral action is assumed to be present inherently in the system model, theoretically there is no need for additional integrators in the controller. An optimal proportional control, for instance, does not have any integrators. So in simulation, the simple-mass plant model such as (3.3) stabilized with a controller without any integrators would still give a zero steady-state error since the plant model itself has double integrator. But the actual plant, being type-0, would have non-zero steady-state error in its closed-loop response. Thus a more realistic model would be one with the spring constant and damping taken into account. In the Δ-stage, a viscoelastic layer was attached to the platen as we indicated in Section 2.3.1-A. This layer can be modeled as a spring and damper. The single-axis actuators also have negative

spring-constants. Similarly, in the Y-stage, there are negative spring-constant terms. In Chapter V, these terms will be identified using closed-loop system identification.

C. Force Transformation

The actuator forces and the forces required to generate motions along the coordinates axes (called the modal forces) are illustrated in Fig. 3.1. By suitably combining actuator forces, 6-DOF motion can be generated. Modal force transformation is required in order to obtain the information of force required from the actuators in order to generate a desired motion along the coordinate axis. Using the geometric parameters defined in the Fig. 3.2(a), the modal force transformation matrix for Δ-stage is given by

$$\begin{bmatrix} f_x \\ f_y \\ \tau_\phi \\ f_z \\ \tau_\theta \\ \tau_\psi \end{bmatrix} = \begin{bmatrix} 0 & 0 & 0 & 1 & -1/2 & -1/2 \\ 0 & 0 & 0 & 0 & \sqrt{3}/2 & -\sqrt{3}/2 \\ 0 & 0 & 0 & l_{1z} & l_{2z} & l_{3z} \\ 1 & 1 & 1 & 0 & 0 & 0 \\ -l_{1y} & -l_{2y} & l_{3y} & 0 & 0 & 0 \\ l_{1x} & -l_{2x} & l_{3x} & 0 & 0 & 0 \end{bmatrix} \begin{bmatrix} F_1 \\ F_2 \\ F_3 \\ F_4 \\ F_5 \\ F_6 \end{bmatrix} \tag{3.4}$$

Substituting the values of the parameters and inverting the matrix, we get

$$\begin{bmatrix} F_1 \\ F_2 \\ F_3 \\ F_4 \\ F_5 \\ F_6 \end{bmatrix} = \begin{bmatrix} 0 & 0 & 0 & 0.3339 & -10.4990 & 18.177 \\ 0 & 0 & 0 & 0.3338 & -10.4990 & -18.177 \\ 0 & 0 & 0 & 0.3323 & 20.9970 & 0 \\ 0.6667 & 0 & 8.3132 & 0 & 0 & 0 \\ -0.3333 & 0.5774 & 8.3132 & 0 & 0 & 0 \\ -0.3333 & -0.5774 & 8.3132 & 0 & 0 & 0 \end{bmatrix} \begin{bmatrix} f_x \\ f_y \\ \tau_\phi \\ f_z \\ \tau_\theta \\ \tau_\psi \end{bmatrix} \tag{3.5}$$

Similarly, for Y-platen, a combination of 6 actuator forces is used to achieve modal forces and torques in all axes at the platen CM through the following modal force transformation matrix.

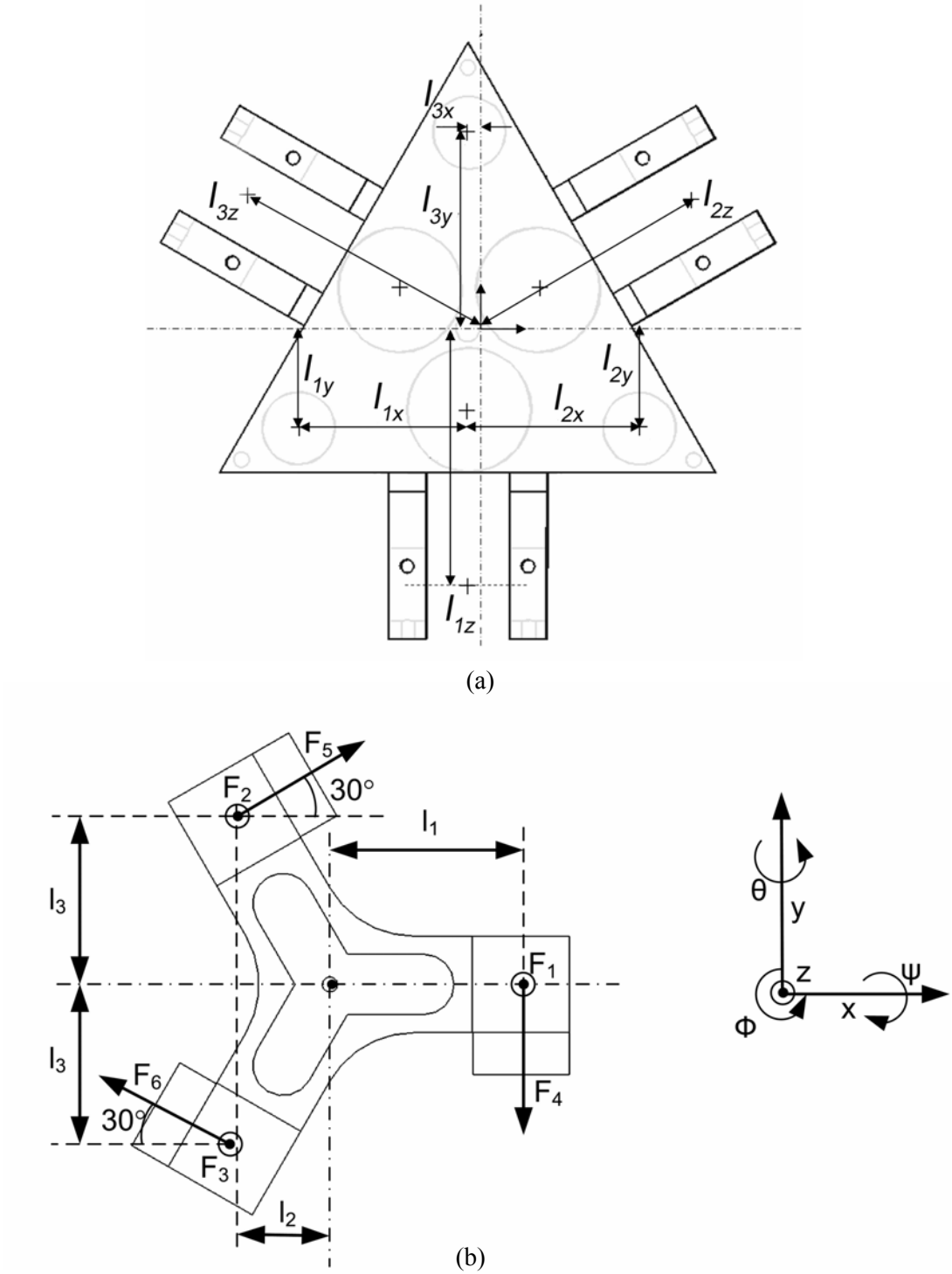

Fig. 3.2. Axis convention and definition of parameters for modal force transformation for (a) the Δ-stage and (b) the Y-stage [62]

$$\begin{bmatrix} f_x \\ f_y \\ \tau_\phi \\ f_z \\ \tau_\psi \\ \tau_\theta \end{bmatrix} = \begin{bmatrix} 0 & 0 & 0 & 0 & \sqrt{3}/2 & -\sqrt{3}/2 \\ 0 & 0 & 0 & -1 & 1/2 & 1/2 \\ 0 & 0 & 0 & -l_1 & -l_1 & -l_1 \\ 1 & 1 & 1 & 0 & 0 & 0 \\ 0 & l_3 & -l_3 & 0 & 0 & 0 \\ -l_1 & l_2 & l_2 & 0 & 0 & 0 \end{bmatrix} \begin{bmatrix} F_1 \\ F_2 \\ F_3 \\ F_4 \\ F_5 \\ F_6 \end{bmatrix} \tag{3.6}$$

The definitions of various forces and geometric parameters are shown in Fig. 3.2(b). Substituting these values and taking the inverse, we get

$$\begin{bmatrix} F_1 \\ F_2 \\ F_3 \\ F_4 \\ F_5 \\ F_6 \end{bmatrix} = \begin{bmatrix} 0 & 0 & 0 & 0.3333 & 0 & -13.1761 \\ 0 & 0 & 0 & 0.3333 & 11.4103 & 6.5880 \\ 0 & 0 & 0 & 0.3333 & -11.4103 & 6.5880 \\ 0 & -0.6667 & -6.5883 & 0 & 0 & 0 \\ 0.5774 & 0.3333 & -6.5883 & 0 & 0 & 0 \\ -0.5774 & 0.3333 & -6.5883 & 0 & 0 & 0 \end{bmatrix} \begin{bmatrix} f_x \\ f_y \\ \tau_\phi \\ f_z \\ \tau_\psi \\ \tau_\theta \end{bmatrix} \tag{3.7}$$

The zeros in the diagonal sub-matrices reveal decoupling between vertical and horizontal modes which was intended in the design. However, due to the error in the assembly of actuators, the horizontal actuators are not located exactly in the same plane as that of the CM, and hence, there are unwanted couplings and stray torques, as we will see in Section 3.2.3. These couplings may be significantly reduced by using feedback linearization in the closed-loop control as demonstrated in Section 2.5.

D. Displacement Transformation

Modal displacement transformation is required in order to obtain the position information of the CM of the platen from the measurement data from sensors. This transformation comes from the sensor equations. Laser interferometry is used for horizontal motion sensing and was discussed on Section 2.4.1. It gives the position and velocity

measurements for x, y and ϕ. The translation in z and rotations about x- and y-axes are obtained from the measurements from three capacitance sensors fixed on the base plate through triangulation method. Fig. 3.3 shows the definitions of the geometric parameters used in the modal transformation. With these definitions, the displacement transformation matrix for the Δ-stage was obtained as follows.

$$\begin{bmatrix} \Delta L_1 \\ \Delta L_2 \\ \Delta L_3 \\ V_1 \\ V_2 \\ V_3 \\ C_1 \\ C_2 \\ C_3 \end{bmatrix} = \begin{bmatrix} 0 & 1 & Y_2 & 0 & 0 & 0 & 0 & 0 & 0 \\ 0 & 1 & -Y_1 & 0 & 0 & 0 & 0 & 0 & 0 \\ -\sqrt{3}/2 & -1/2 & X_1 & 0 & 0 & 0 & 0 & 0 & 0 \\ 0 & 0 & 0 & 0 & 1 & Y_2 & 0 & 0 & 0 \\ 0 & 0 & 0 & 0 & 1 & -Y_1 & 0 & 0 & 0 \\ 0 & 0 & 0 & -\sqrt{3}/2 & -1/2 & X_1 & 0 & 0 & 0 \\ 0 & 0 & 0 & 0 & 0 & 0 & 1 & -Z_{1y} & Z_{1x} \\ 0 & 0 & 0 & 0 & 0 & 0 & 1 & Z_{2y} & -Z_{2x} \\ 0 & 0 & 0 & 0 & 0 & 0 & 1 & Z_{3y} & Z_{3x} \end{bmatrix} \begin{bmatrix} \tilde{x} \\ \tilde{y} \\ \tilde{\phi} \\ \tilde{u} \\ \tilde{v} \\ \tilde{r} \\ \tilde{z} \\ \tilde{\psi} \\ \tilde{\theta} \end{bmatrix} \tag{3.8}$$

Substituting the values of parameters and inverting the matrix, we get

$$\begin{bmatrix} \tilde{x} \\ \tilde{y} \\ \tilde{\phi} \\ \tilde{u} \\ \tilde{v} \\ \tilde{r} \\ \tilde{z} \\ \tilde{\psi} \\ \tilde{\theta} \end{bmatrix} = \begin{bmatrix} 0 & -0.5774 & -1.1547 & 0 & 0 & 0 & 0 & 0 & 0 \\ 0 & 1 & 0 & 0 & 0 & 0 & 0 & 0 & 0 \\ 18.1818 & 0 & 0 & 0 & 0 & 0 & 0 & 0 & 0 \\ 0 & 0 & 0 & 0 & -0.5774 & -1.1547 & 0 & 0 & 0 \\ 0 & 0 & 0 & 0 & 1 & 0 & 0 & 0 & 0 \\ 0 & 0 & 0 & 18.1818 & 0 & 0 & 0 & 0 & 0 \\ 0 & 0 & 0 & 0 & 0 & 0 & 0.3234 & 0.4119 & 0.2648 \\ 0 & 0 & 0 & 0 & 0 & 0 & -45.2305 & 14.9638 & 30.2666 \\ 0 & 0 & 0 & 0 & 0 & 0 & 0 & -44.8833 & 44.8833 \end{bmatrix} \begin{bmatrix} \Delta L_1 \\ \Delta L_2 \\ \Delta L_3 \\ V_1 \\ V_2 \\ V_3 \\ C_1 \\ C_2 \\ C_3 \end{bmatrix}$$

(3.9)

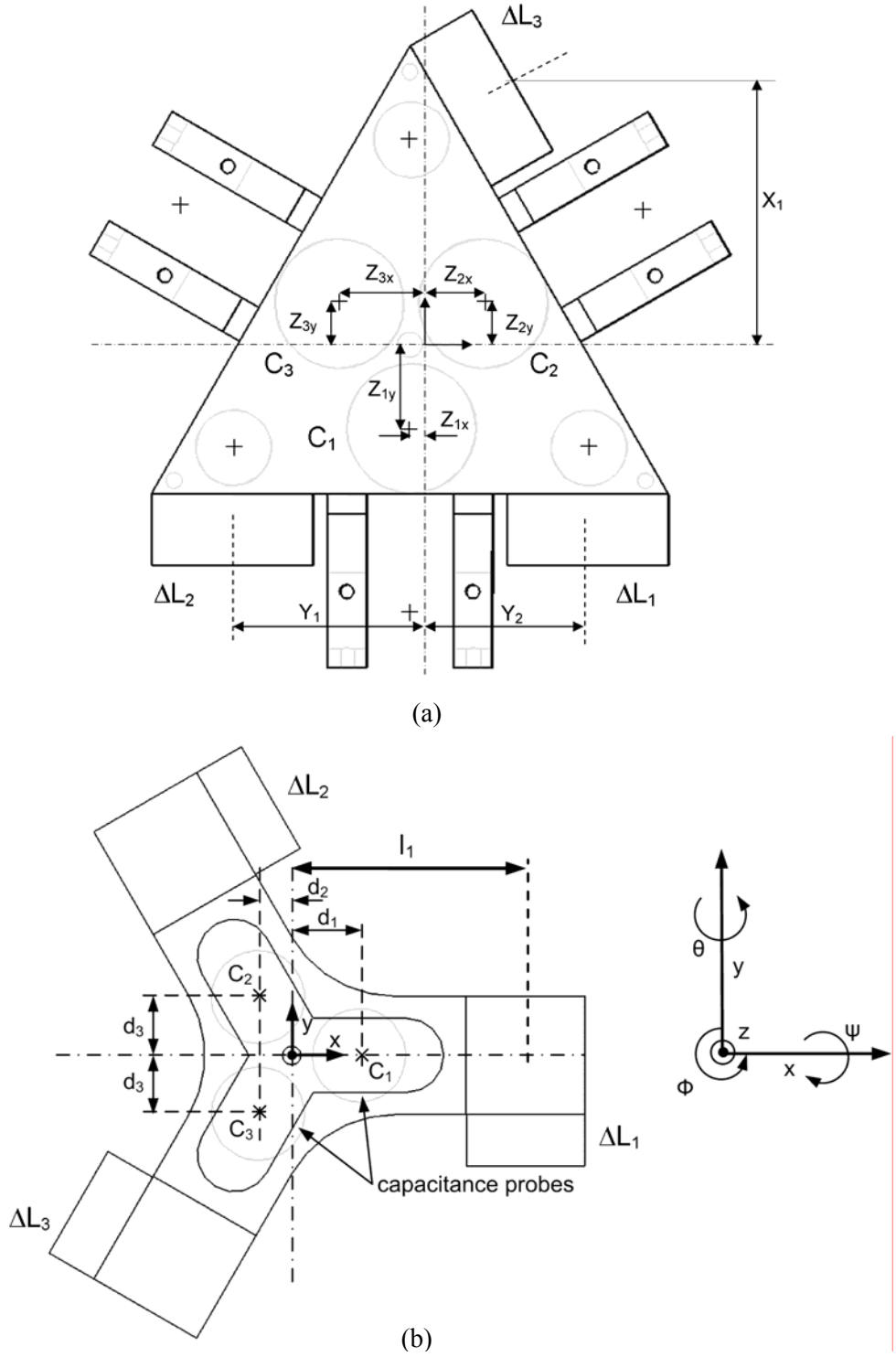

Fig. 3.3. Axis convention and definition of parameters for modal displacement transformation for (a) the Δ-stage and (b) the Y-stage [62]

Similarly, for Y-stage we get the following displacement transformation matrix.

$$\begin{bmatrix} \Delta L_1 \\ \Delta L_2 \\ \Delta L_3 \\ V_1 \\ V_2 \\ V_3 \\ C_1 \\ C_2 \\ C_3 \end{bmatrix} = \begin{bmatrix} 0 & 1 & l_1 & 0 & 0 & 0 & 0 & 0 & 0 \\ -\sqrt{3}/2 & -1/2 & l_1 & 0 & 0 & 0 & 0 & 0 & 0 \\ \sqrt{3}/2 & -1/2 & l_1 & 0 & 0 & 0 & 0 & 0 & 0 \\ 0 & 0 & 0 & 0 & -1 & l_1 & 0 & 0 & 0 \\ 0 & 0 & 0 & \sqrt{3}/2 & 1/2 & l_1 & 0 & 0 & 0 \\ 0 & 0 & 0 & -\sqrt{3}/2 & 1/2 & l_1 & 0 & 0 & 0 \\ 0 & 0 & 0 & 0 & 0 & 0 & 1 & 0 & -d_1 \\ 0 & 0 & 0 & 0 & 0 & 0 & 1 & d_3 & d_2 \\ 0 & 0 & 0 & 0 & 0 & 0 & 1 & -d_3 & d_2 \end{bmatrix} \begin{bmatrix} \tilde{x} \\ \tilde{y} \\ \tilde{\phi} \\ \tilde{u} \\ \tilde{v} \\ \tilde{r} \\ \tilde{z} \\ \tilde{\psi} \\ \tilde{\theta} \end{bmatrix} \tag{3.10}$$

Substituting the values of parameters and inverting the matrix, we get

$$\begin{bmatrix} \tilde{x} \\ \tilde{y} \\ \tilde{\phi} \\ \tilde{u} \\ \tilde{v} \\ \tilde{r} \\ \tilde{z} \\ \tilde{\psi} \\ \tilde{\theta} \end{bmatrix} = \begin{bmatrix} 0 & 0.5774 & -0.5774 & 0 & 0 & 0 & 0 & 0 & 0 \\ -0.6667 & 0.3333 & 0.3333 & 0 & 0 & 0 & 0 & 0 & 0 \\ 6.5928 & 6.5928 & 6.5928 & 0 & 0 & 0 & 0 & 0 & 0 \\ 0 & 0 & 0 & 0 & 0.5774 & -0.5774 & 0 & 0 & 0 \\ 0 & 0 & 0 & -0.6667 & 0.3333 & 0.3333 & 0 & 0 & 0 \\ 0 & 0 & 0 & 6.5928 & 6.5928 & 6.5928 & 0 & 0 & 0 \\ 0 & 0 & 0 & 0 & 0 & 0 & 0.3333 & 0.3333 & 0.3333 \\ 0 & 0 & 0 & 0 & 0 & 0 & 0 & 40.0128 & -40.0128 \\ 0 & 0 & 0 & 0 & 0 & 0 & -46.2000 & 23.1000 & 23.1000 \end{bmatrix} \begin{bmatrix} \Delta L_1 \\ \Delta L_2 \\ \Delta L_3 \\ V_1 \\ V_2 \\ V_3 \\ C_1 \\ C_2 \\ C_3 \end{bmatrix}$$

(3.11)

In these transformations, ΔL_1, ΔL_2, and ΔL_3 are the changes in the optical paths of laser (Fig. 3.4), and V_1, V_2, and V_3 are the horizontal velocity measurements, sensed by the laser interferometers, and C_1, C_2, and C_3 are the vertical displacement measurements by the capacitance sensors. $\begin{bmatrix} \tilde{x} & \tilde{y} & \tilde{\phi} & \tilde{u} & \tilde{v} & \tilde{r} & \tilde{z} & \tilde{\psi} & \tilde{\theta} \end{bmatrix}^T$ is the state vector representing the perturbations of the position and velocity of the platen from its operating point.

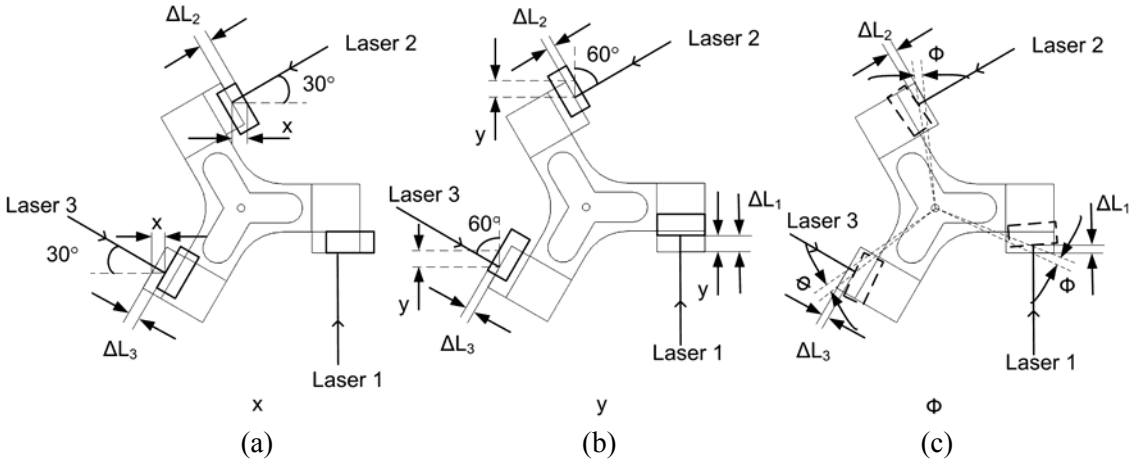

Fig. 3.4. Displacement of plane mirrors while motion in the (a) x, (b) y and, (c) ϕ [62]

3.1.3 Decoupled SISO Control

In the previous subsection, dynamic model of the two maglev stages were developed using decoupled 6-axis motions and identified modal force and displacement transformations for discrete-time closed-loop implementation of the controllers. In this section I describe the design of six individual PID controllers developed by Gu and Verma [61, 62] for preliminary motion-testing of the platens.

A. Sampling Frequency

The controller is implemented on the DSP. The control loop is illustrated in the Fig. 3.5. Each control loop consists of (a) sampling the sensor data, (b) transforming it to the modal translation and rotation, (c) calculating the control outputs using the reference signal, (d) converting the controller output in the form of modal forces and torques to the plant input in the

form of voltage across the six actuating coils, and (e) applying the designated output voltage to the maglev stage. This control loop repeats at the sampling frequency of the system.

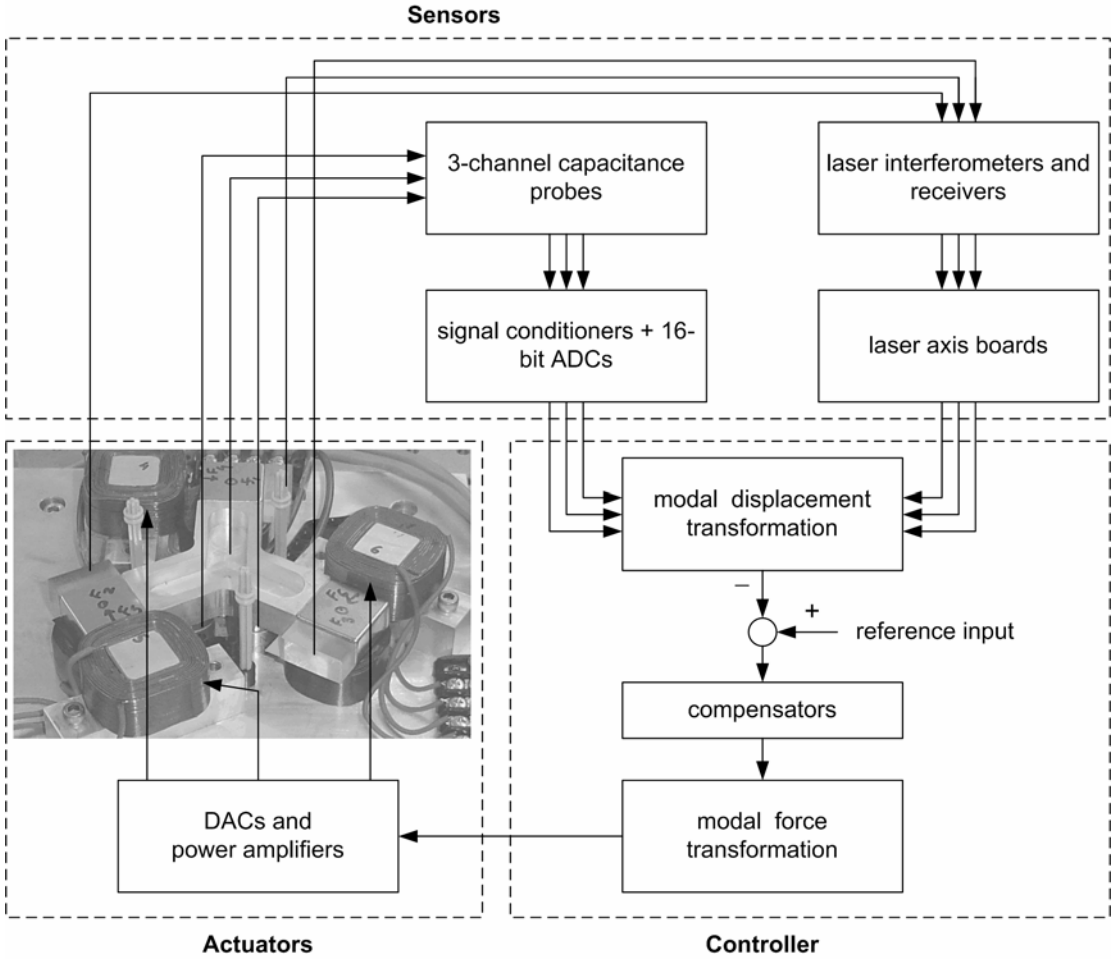

Fig. 3.5. Control loop for the real-time control of maglev system

The selection of sampling frequency depends on a number of factors, viz., the sensor sampling rate, system resonant frequency, system bandwidth, and computing power. The sampling frequency must be higher than Nyquist frequency in digital control to avoid aliasing. A higher sampling frequency is preferred so that the discrete-time dynamics can emulate the

continuous time without much error. A typical choice of the sampling frequency could be around 20 times the closed-loop bandwidth [75]. However, a high sampling frequency means less time per cycle for the DSP to complete all the designated calculations. The choice of sampling frequency requires a trade-off between these two conflicting conditions. Based on the system clock speed, the sampling frequency was decided to be 5 kHz.

B. Controller TFs

Magnetostatic levitation in free space is inherently unstable. This is because the permeability of any material is always greater than that of free space [76]. In order to stabilize and control the maglev system, six independent are required for each of the 6 axes with the assumption that the axes are decoupled. Gu and Verma designed SISO PID controllers with modified differential terms for preliminary testing of the two maglev positioners [61, 62]. I modified these controllers using MATLAB toolbox `SISOTOOL` and the plant models presented in the previous section. Each controller has a free pole at the origin of the *s*-plane to eliminate steady-state error. The differentiator term is modified by adding a pole at high-frequency to reduce the effect of high frequency noise amplification. For the Δ-stage, a controller was designed a phase margin (PM) of 50º at the crossover frequency 48 Hz. The discrete-time transfer function for this compensator with a 5-kHz sampling frequency and bilinear method of conversion is given by

$$G(z) = \frac{K(z-0.9984)(z-0.9743)}{(z-1)(z-0.7970)} \tag{3.12}$$

The controller gain $K = 61846$ N/m for translational motion control. Its value for the rotational control about *x*-, *y*-, and *z*-axes were 38.655, 35.572, and 68.616 N-m/rad, respectively.

Modified PID controllers were designed for Y-stage in the same way. The controllers for horizontal motion control were designed with a PM of 70° at the crossover frequency of 110 Hz. The designed compensator is given by

$$G(z) = \frac{K(z-0.9978)(z-0.9770)}{(z-1)(z-0.4271)} \tag{3.13}$$

The value of control gain K for x and y is 5.328×10^5 N/m and 1.304×10^3 N-m/rad for ϕ. For vertical motion control, a controller was designed with a PM of 70° at crossover frequency of 65 Hz. The discrete-time compensator TF is given by

$$G(z) = \frac{K(z-0.9988)(z-0.9886)}{(z-1)(z-0.6525)} \tag{3.14}$$

The value of K is 1.929×10^5 N/m for z and 2.458×10^2 N/m^2 for ψ and θ. Experimental results presented in the following sections are obtained using these controllers.

3.2 Set-Point Change Tests

Several experiments were conducted to illustrate the nanoscale multi-axis motion control of the maglev devices in terms of position regulation, step responses, and multi-axis contouring. These results have been reported in detail in [62]. Here I present some of the experimental results to validate the values reported in the Table 2.1. Position regulation and step responses for horizontal motion were taken using the x-axis motion in both the stages. Since the performance of the y-axis is not much different from that of the x-axis, the corresponding results are omitted.

3.2.1 Regulation

The experimental results on the position regulation for horizontal and vertical motion of the Δ-stage are shown in Fig. 3.6(a). Fig. 3.6(b) shows the position noise profiles of the Y-stage. The position noise is around 2 and 3 nm rms for horizontal motion for Δ- and Y-stage, respectively. Vertical motion noise is about the same for both the positioners and is around 50 nm rms. The position noise for the vertical motion is higher due to the capacitance sensor noise, ADC noise, and ADC quantization. Despite the noise in the vertical axes the horizontal motion profiles are relatively very quiet.

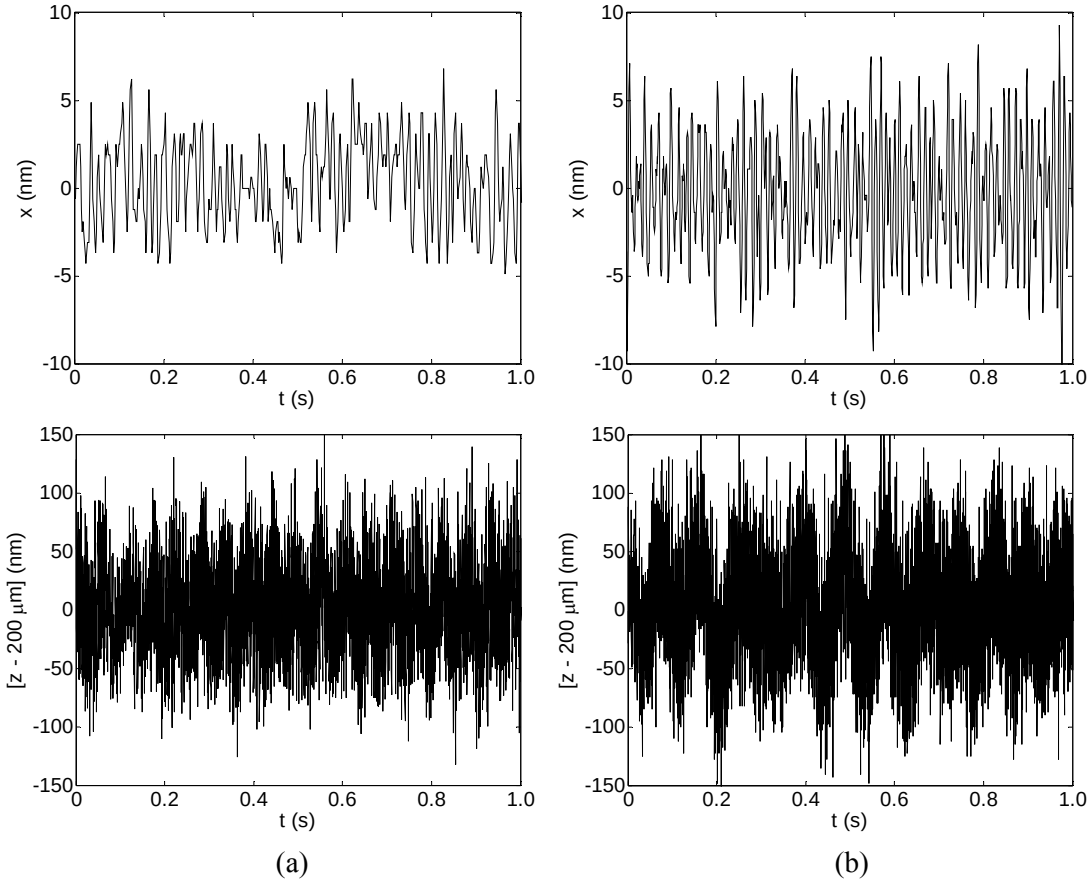

Fig. 3.6. Position regulation in (a) the Δ-stage and (b) the Y-stage

3.2.2 Positioning

Fig. 3.7(a) shows a 10-nm step response of the Δ-stage in the *x*-axis. The positional resolution is clearly better than 2 nm. Fig. 3.7(b) shows a 10-nm step response of the Y-stage in the *x*-axis. The position resolution is again maintained under 3 nm. The reason for the Δ-stage to have a better resolution is due to the viscoelastic and constraint layers provided in its mechanical design. These layers provide certain amount of damping to the external vibrations and hence the regulated response has a lower noise level compared to the Y-stage. In terms of position resolution, this improved noise performance translates into a smaller discernible step-size.

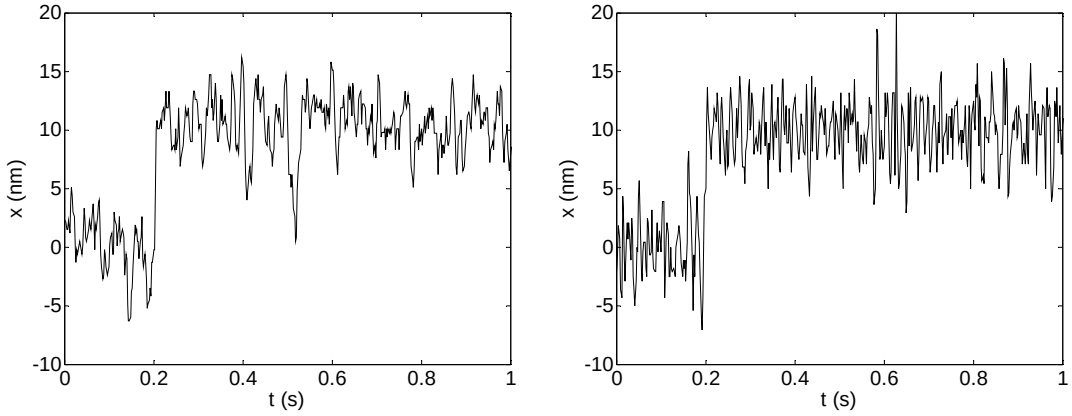

Fig. 3.7. 10-nm step response of (a) the Δ-stage and (b) the Y-stage

Figs. 3.8 and 3.9 respectively shows the step response of 250 μm in *x* with the Δ- and Y-stages with coupled motions in the other axes. It may be observed that there is significant coupling in the system. This is primarily because of the factors discussed earlier in Section 3.1. The two plots were taken using the controllers given by (3.12)–(3.13). The control bandwidths for these two controllers were 48 Hz and 110 Hz, respectively. Since the masses of the two stages do not differ significantly, a faster response was expected from the Y-stage. A close

inspection of the *x*-axis responses of the two stages shows a contradiction. Further investigation of the two plots reveals that there are significant deviations of the closed-loop responses compared to the simulations. This has been shown in Fig. 3.10. For the Δ-stage, although the rise and settling times match closely with the simulated responses, there is a significant difference in the overshoot. This is because the effect of damping present inherently in the Δ-stage platen. This damping was not modeled as indicated earlier in the Section 3.1.2-B. Likewise, the Y-stage has several unmodeled dynamics which results in significant mismatch between simulation and experiment results. The source of these mismatches will be explored in details in Chapter V. These differences in the performances of the two positioners motivate the need to develop more accurate plant models for better controller design.

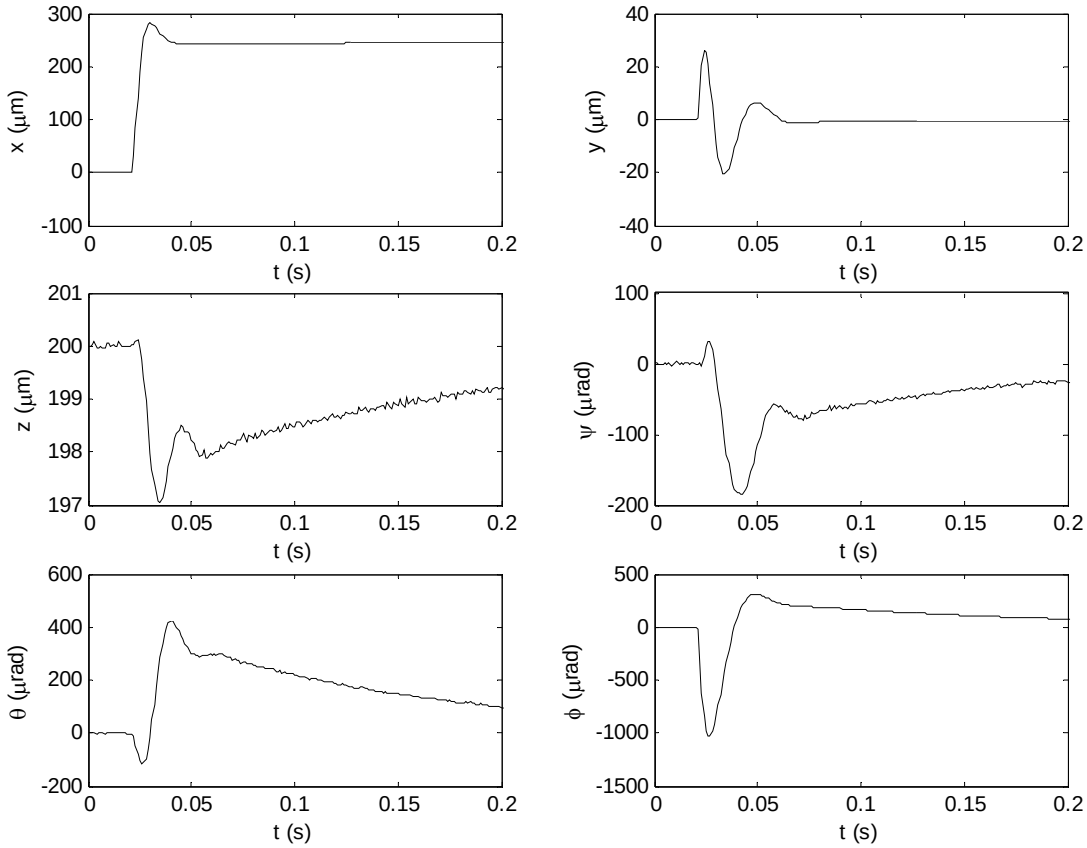

Fig. 3.8. 250-μm step response of the Δ-stage with coupled motions in the other 5 axes

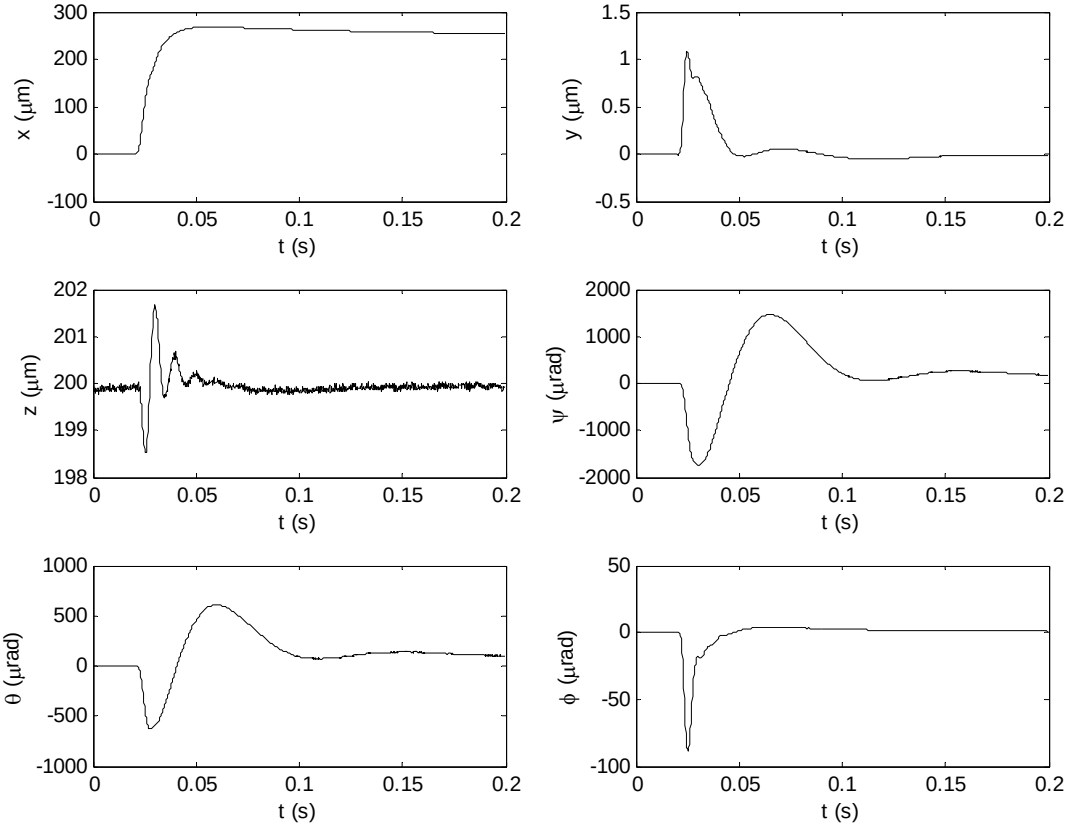

Fig. 3.9. 250-μm step response of the Y-stage with coupled motion in the other 5 axes

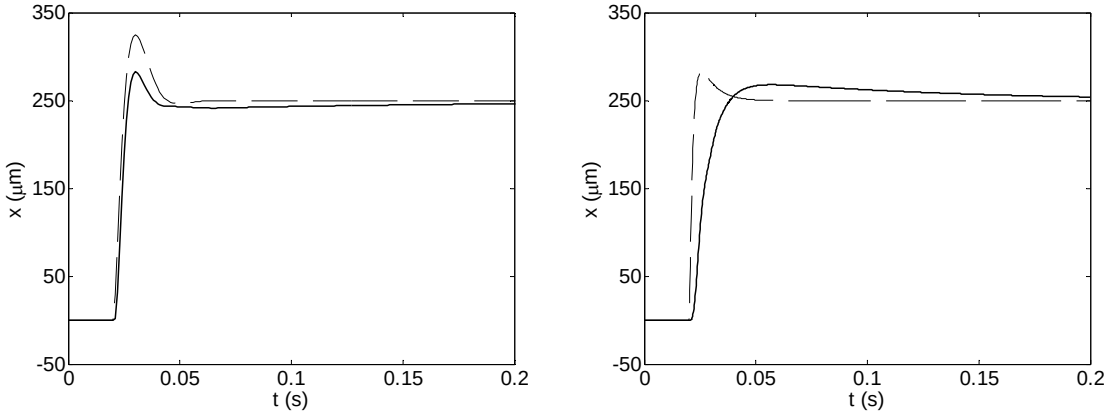

Fig. 3.10. Simulated (dashed) and experimental (solid) responses to a 250-μm step with (a) the Δ-stage and (b) the Y-stage

3.2.3 Multi-Axis Tracking

In the real-time control code written in the C language as an ISR, a set of data points in more than one axis can be allocated with respect to time so that the platen can follow a multi-axis trajectory. In Fig. 3.11(a), a commanded path of a 50-nm-radius circle, the response of the Δ-stage and the position errors in the *x*- and *y*-axes are shown. Fig. 3.11(b) shows a 0.5-mm-radius circular path traversed by the Y-stage and the position errors in the *x*-*y* plane. The motions of the platens were very close to a perfect circle in both the cases. These test results demonstrate the small multi-axis motion capabilities of the two maglev devices. Note that the time taken by the two platens to traverse the respective circular trajectories is also different. The nanoscale trajectory was traversed at a slower rate compared to the 0.5-mm one. This was necessary to obtain discernible results. The effect of speed on motion planning will be further emphasized in Chapter VI. In addition to its multi-axis contouring capabilities, Fig. 3.11(b) also demonstrates the larger travel range positioning capabilities of the Y-stage. Larger travel range is also demonstrated by a ramp response of 5 mm in the *x*-axis, which covers the entire travel range. The ramp response is shown in Fig. 3.12.

It may be seen from Figs. 3.6(b), 3.9, 3.11(b), and 3.12 that although Y-stage demonstrates superior positioning capabilities in position regulation and small scale motion on the order of a few nanometers, the performance deteriorates on larger scales. In a 0.5-mm-radius circle, for example, the position error can be as large as 21 μm. Similarly, in ramp response, the 3-nm position resolution can no longer be achieved. This is because of several reasons. Firstly, the plane of application of actuator forces is not perfectly aligned with the CM. This difference was not modeled while deriving the plant model for controller design, and thus results in undesired coupling forces and moments. Secondly, the plant model (3.3) was assumed linear and derived about an operating point (plant modeling and linearization will be covered in further

details in Chapter IV.) The actuator forces were calculated assuming that the perturbations in position from this operating point are small. However, as discussed in Section 2.5, the effect of actuator nonlinearities become significant as the coil-magnet gap changes, or in other words, as the platen position deviates significantly from the operating point. Thus, the position resolution is not comparable at millimeter- and nanometer-level precision. This motivates the need to develop advanced control schemes and motion planning methodologies in order to achieve identical performances on macroscale as well as nanoscale levels. These control schemes and motion and path planning methods will be discussed in the following chapters.

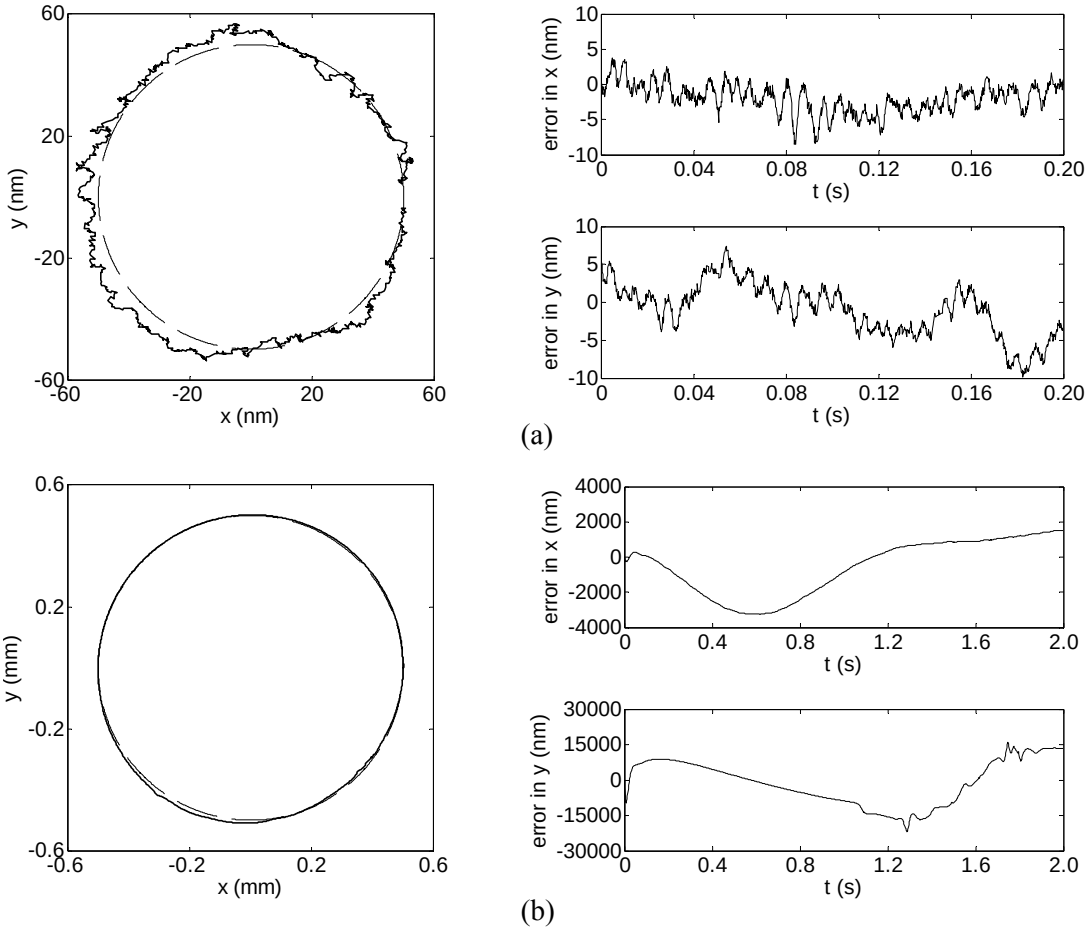

Fig. 3.11. (a) 50-nm-radius circle traversed by the Δ-stage and errors in the *x*- and *y*-axes, and (b) 0.5-mm-radius circle traversed by the Y-stage and errors in the *x*- and *y*-axes

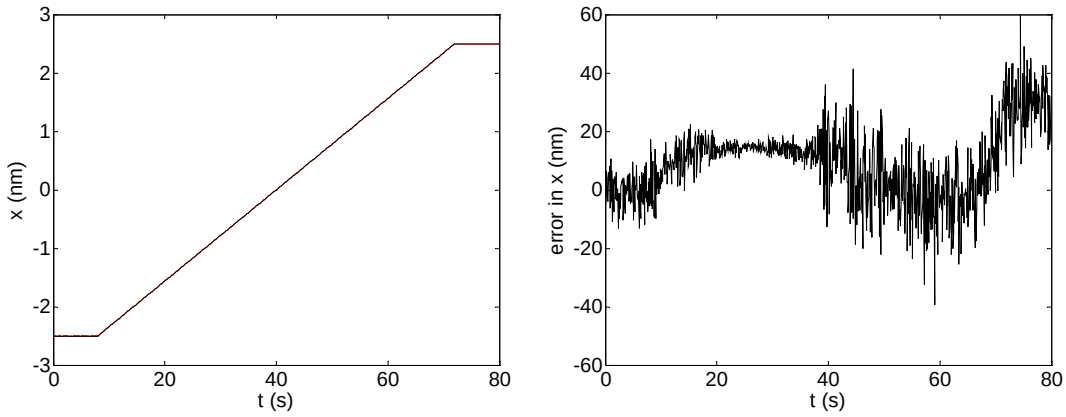

Fig. 3.12. 5-mm ramp response by the Y-stage and error in the *x*-axis

3.3 Load Tests

It is important to analyze the dynamic behavior of the maglev nanopositioner under load changes in order to be able to use it in practical applications like μSTL, scanning, and indentation. These load changes may appear in the form of payload variations in μSTL or as instantaneous force disturbance due to the insertion of a tool or probe tip in contact-type scanning or indentation. Accordingly, a number of load-tests were designed and performed on the two maglev stages to prove their precision-positioning capabilities under load changes. Controllers (3.12) and (3.13–3.14) were used for vertical motion control for the Δ-stage and the Y-stage, respectively.

3.3.1 Payload Capacity

In order to test the dynamic performance of the positioner for its payload capacity, set-point-change tests were performed with different payloads. The experimental setup is shown in Fig. 3.13. The experimental results of these tests are reported in Fig. 3.14(a) and (b). The two

stages were able to levitate and position additional payloads of 0.3 kg and 0.2 kg, respectively, on the platen. The additional payload increases the mass, keeping the system stiffness about the same, which lowers the natural frequency of the moving platen. Due to this lower natural frequency the rise time and the settling time are longer for the larger payloads as shown in the figure. The percentage overshoot was reduced as the payload increased. With the payloads more than the maximum, the positioner went out of the range of the laser interferometer sensors for horizontal motion sensing due to excessive rotations about the *x*- and *y*-axes. This is because of the fact that the dead-weights could not be placed exactly at the center of the platen. Hence, a step motion in *z* generates stray torques about the *x*- and *y*-axes. However, with the sensors capable of sensing large linear and rotational motions, the current actuator design would allow additional payloads of more than the maximum shown in Fig. 3.14.

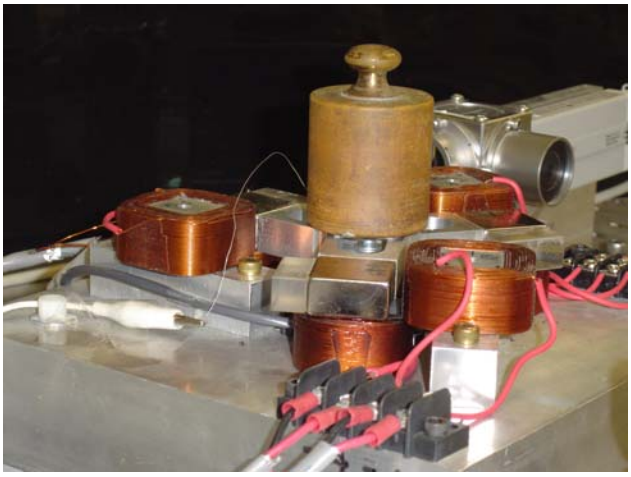

Fig. 3.13. Experimental setup to determine the payload capacity

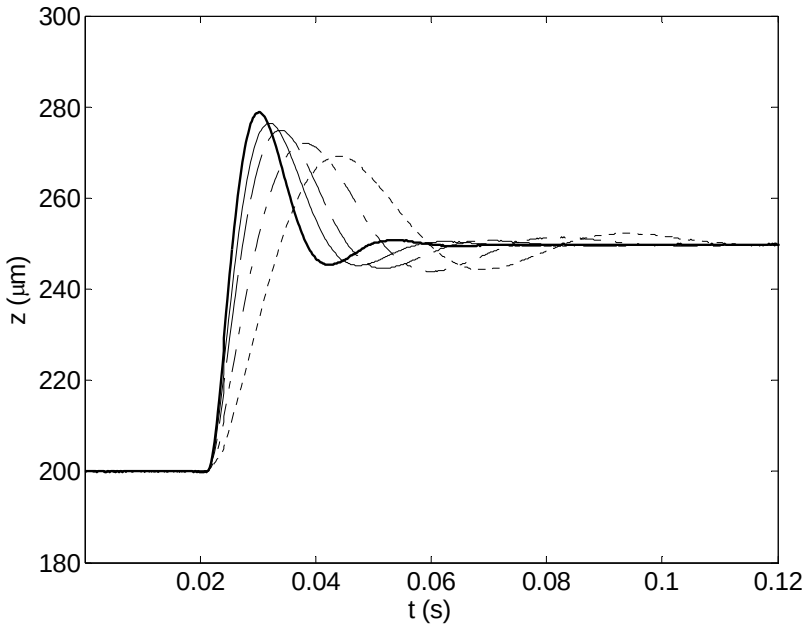

(a)

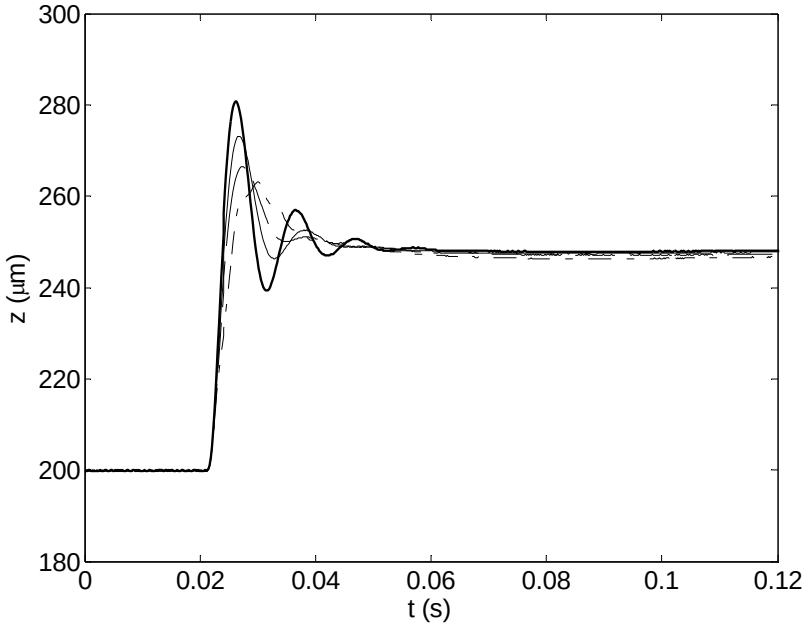

(b)

Fig. 3.14. No-load (thick solid line) and load test with additional payloads of 50 g (thin solid line), 100 g (dashed line), 200 g (dash-dotted line), and 300 g (dotted line) with (a) the Δ-stage and (b) the Y-stage

3.3.2 Performance under Abrupt Load Changes

In the applications like contact-probe-based scanning, the instantaneous disturbance due to the engagement and disengagement of the probe tip with the specimen surface may be emulated as a disturbance resulting from abrupt load changes. In nano-indentation, a stiff AFM tip may be fixed to the base to make indents or scratches and write small letters or draw tiny shapes on a silicon substrate mounted on the moving platen. In such an application, the process of making indents with the cantilever tip may be treated as load disturbance. Although the disturbance is not expected to exceed more than a few milli-newtons in these applications, the maglev positioner demonstrates precision positioning under the abrupt load variations on the order of one hundred milli-newtons.

To test the response of the two maglev stages for sudden load changes I used small cylinders as additional payloads. The experimental setup for this experiment for Y-stage is shown in Fig. 3.15. Fig. 3.16(a) shows the plots of the z-axis position and the control effort by the controller to recover the position of the Δ-stage when the two cylinders were taken off one at a time. The load removal generated perturbations in z. In the beginning of this experiment, the vertical actuators supplied the forces to precisely balance the weight of the platen and the payload. As soon as the additional payload was removed, the applied force instantaneously became greater than that is required to balance the weight of the platen and the payload. This excessive force gave the platen an instantaneous upward push, which was recovered by the controller over a period of 0.6 s. The maglev system's dynamic behavior was found to be repeatable for the second load removal. It can be observed from Fig. 3.16(a) that the control effort in z decreased as soon as a cylinder was removed. The drop in the control effort was measured to be 0.14 N for first cylinder and 0.135 N for the second cylinder. The mass of each

cylinder was 14 g, i.e. its weight is 0.137 N. This shows that the error between the experimental control effort and the actual force is only around 2%.

Fig. 3.16(b) shows the performance of the Y-maglev stage with abrupt load changes. Small 7.5-g cylinders were used in this case as additional loads. The performance of this stage was found to be similar to the previous one. It can be observed from Fig. 3.16(b) that the drop in the control effort as each cylinder was removed was approximately 0.07 N. This matches with the actual weight of the cylinders with an error of merely 5%. The difference in the nominal control effort in two cases is due to the larger mass of the Y-platen compared to the Δ-platen. The position response and control effort required for the Y-stage are noisier compared to the Δ-stage. This is partly because of the use of viscoelastic and constraint layers in the design of Δ-stage which provides damping. The use of different controllers in the two cases might also have resulted in the different performances. Nevertheless, the two positioners demonstrate the effectiveness in recovering from abrupt load changes within a short interval and without loosing stability, which was the central objective of these experiments.

3.3.3 Performance under Continuously Varying Loads

External forces may also appear in the form of continuous payload variation or mass fluctuation. For instance, in μSTL, the mass of the substrate varies as the photopolymer is solidified. In this subsection, the effectiveness of the maglev positioners to recover from such load variations is demonstrated. Apparently, the anticipated load variation in any of the practical applications working at micro- or nano-scale is much less than the demonstrated load capacity of the maglev stage under continuously varying loads.

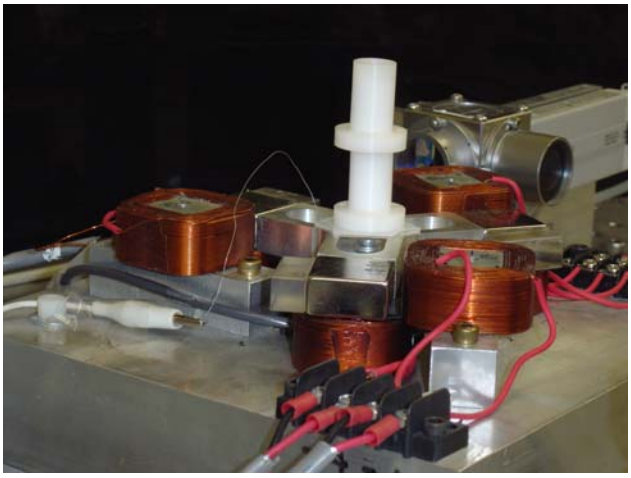

Fig. 3.15. Experimental setup to determine the payload capacity under abrupt load changes

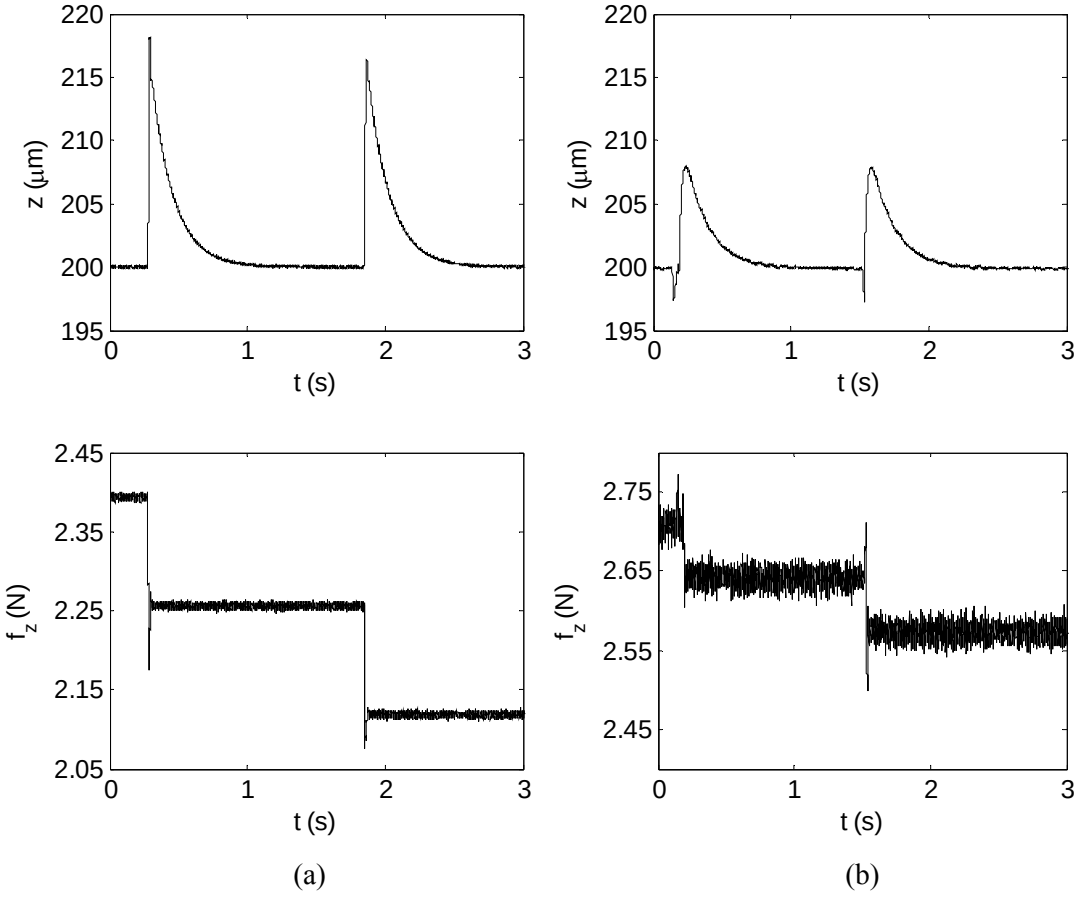

Fig. 3.16. Position in z and control effort f_z by the controllers under abrupt load changes with (a) the Δ-stage and (b) the Y-stage

To emulate the effect of the continuously varying mass in nanomanufacturing applications, I used a continuous flow of salt falling into a small bucket placed on the platen. The experimental setup is shown in Fig. 3.17. The z position of the Δ-platen and the corresponding control effort required are shown in Fig. 3.18(a). Fig. 3.18(b) shows the analogous results for the Y-platen. The platens were levitated at a height of 200 μm. From this initial steady-state position, the mass inflow was initiated and stopped intermittently. Since the rate of the mass change was almost constant, the control effort linearly increased in both the cases to balance the additional mass on the platen and to recover the vertical position of the platen to the steady state. However, there was a small steady-state error in the vertical position during the mass in-flow, which may be considered as a constant force disturbance. This is attributed to the fact that the plant poles are not located precisely at the origin in the complex plane. A detailed analysis of the actual plant model identified using closed-loop system identification will be given in Chapter V. Additionally, the controllers (3.12–3.14) for the two platens were designed with a single pole at the origin, to meet the zero-steady-state error requirement for the position inputs only. Accordingly, for ramp or acceleration/force inputs, the tracking error is not zero. However, immediately after the force disturbance was removed, the steady-state error became zero, which demonstrates the controllers' effectiveness and the fast closed-loop dynamics.

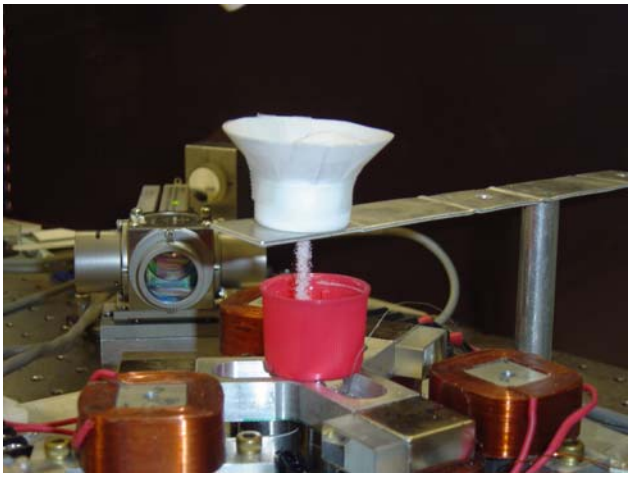

Fig. 3.17. Experimental setup to determine the payload capacity under continuously varying loads

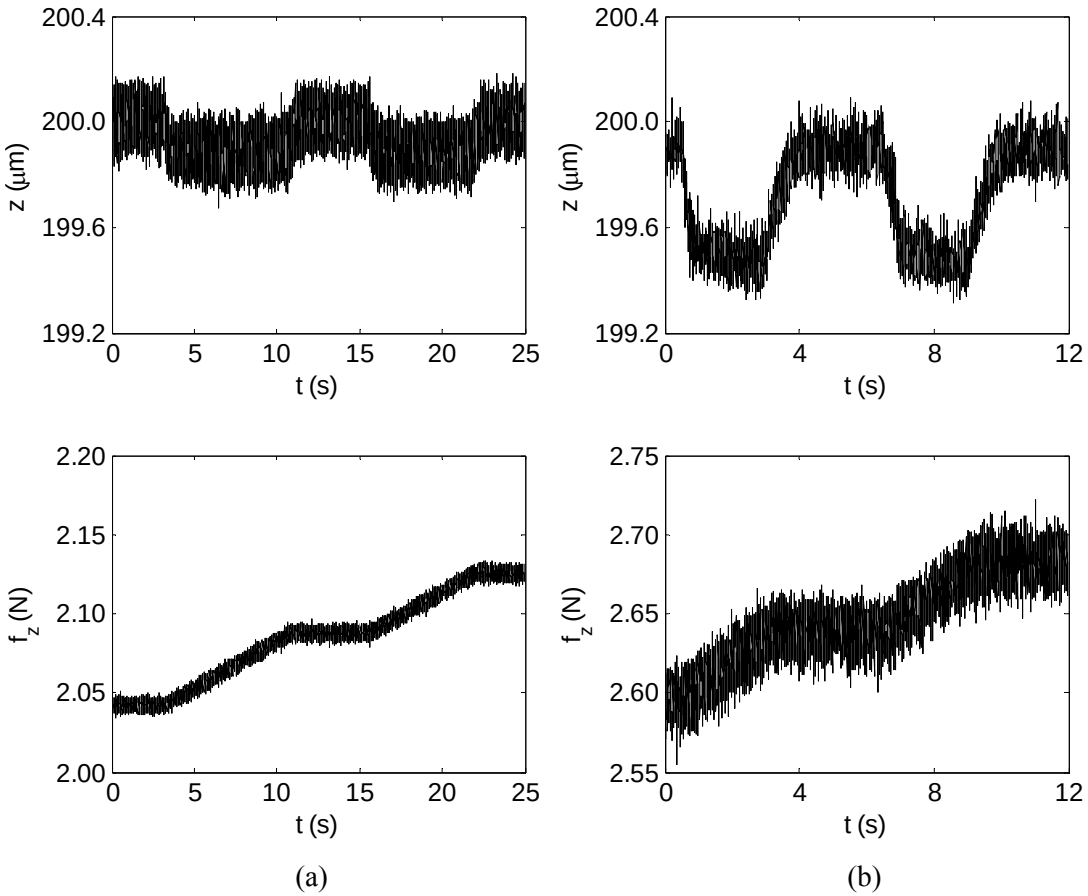

Fig. 3.18. Position in z and control effort f_z by the controller under continuously varying loads with (a) the Δ-stage and (b) the Y-stage

CHAPTER IV

MULTIVARIABLE CONTROL

4.1 Introduction

In Chapter III, the preliminary testing results for the two maglev nanopositioners were presented with the decoupled SISO lead-lag controllers. These controllers gave good regulation and tracking performance with nanometer-precision positioning capabilities. However, for large scale motion, there was significant amount of coupling present in the system. This was apparent from Figs. 3.11(b) and 3.12. Even for steps as small as 250 μm, the effect of coupling in the other axes may be vividly seen (Figs. 3.8–3.9). This is because a single-piece moving part is used to generate all the 6-axis motions. Additionally, due to inaccuracies in the assembly of the actuator units relative to the platen, the plane of application of forces is not exactly aligned with the platen's plane of CM.

In this chapter, a systematic procedure for modeling, linearization, and multivariable optimal control of the two maglev positioners will be presented. The final state-space equations differ for the two positioners due to the differences in their physical parameters. However, the modeling and controller design processes are the same for both due to similar actuator placements and sensing methods. I will resume the use of decoupled lead-lag controllers for the vertical control. The system equations will be derived using the Euler angle methodology and linearized about an operating point. The performance of this multivariable control will be analyzed and compared with that of six decoupled SISO controllers. The effect of adding the

integrators to eliminate the steady-state error will also be discussed and the performance of the LQR controller with different weight matrices will be compared.

4.2 Plant Modeling and Linearization

Since the single-moving platen generates all the required motions, its dynamics is coupled in all the 6 DOFs. In order to understand the observed dynamic behavior and develop high-performance controllers, precise dynamic modeling is required. The full equations of motion are nonlinear because of the nonlinear current-force characteristics of the coil as well as the dependence of motion of the platen on the trigonometric functions of the angles of rotation with respect to the inertial frame. In this section, linearized state-space equations of motion of the platen are derived starting with the nonlinear equations of motion with no approximations, followed by linearization of those equations about an operating point.

A. Euler Angles

One can carry out the transformations from a given cartesian coordinate system to another (in this case, from the stationary frame, *xyz* to the body frame, $x'y'z'$) by means of three successive rotations performed in a specific sequence. The Euler angles are then defined as the three successive angles of rotation. The main convention that is followed in this chapter is the *xyz* convention which is commonly used in most engineering applications [77]. The sequence used in this convention is started by rotating the initial frame of axes, *xyz*, by an angle ϕ counterclockwise about the *z*-axis. The resultant coordinate system is called the $\xi\eta\zeta$ axes. Then, the second angle of rotation around the intermediate ξ-axis in the counterclockwise rotation is defined as θ. The new intermediate coordinate system thus obtained is called $\xi'\eta'\zeta'$ axes.

Finally, the rotation by an angle ψ about the ξ'-axis in counterclockwise direction results in the desired $x'y'z'$ coordinate frame. The Euler angles ϕ, θ, and ψ thus completely specify the orientation of the $x'y'z'$ system relative to the *xyz*. The complete transformation matrix $\mathbf{\Omega}$ can be obtained by multiplying the three rotation transformations. The inverse of this matrix gives the desired transformation from body to inertial frame and is given by

$$\mathbf{\Omega}^{-1} = \begin{bmatrix} \cos\theta\cos\phi & \sin\psi\sin\theta\cos\phi - \cos\psi\sin\phi & \cos\psi\sin\theta\cos\phi + \sin\psi\sin\phi \\ \cos\theta\sin\phi & \sin\psi\sin\theta\sin\phi + \cos\psi\cos\phi & \cos\psi\sin\theta\sin\phi - \sin\psi\cos\phi \\ -\sin\theta & \sin\psi\cos\theta & \cos\psi\cos\theta \end{bmatrix}.$$

B. Linearized Equations of Motion

The state variable to describe the general motions of the platen completely in 6 DOFs are chosen as follows.

$$\boldsymbol{x} = \begin{bmatrix} x & y & z & u & v & w & \psi & \theta & \phi & p & q & r \end{bmatrix}^T. \tag{4.1}$$

The first six states are the position (in m) and velocity (in m/s) components of the center of mass of the platen with respect to the origin of the inertial frame described in the inertial frame. The seventh, eighth, and ninth states are the Euler angles (in rad) and the last three states are the angular velocity (in rad/s) components of the platen described in the body frame. For small angular motions of the levitator, the Euler angles ψ , θ , and ϕ can be considered as rotational angles around the *x*-, *y*-, and *z*-axes respectively. The angular velocity components described in the inertial frame are approximately the same as those described in the body frame in case of a small signal linearized equations of motion. However, for the time being, the angles are assumed to be large enough to treat unprimed and primed coordinates separately. We have the following kinematic relationships among the state variables.

$$\dot{x} = u \tag{4.2a}$$

$$\dot{y} = v \tag{4.2b}$$

$$\dot{z} = w \tag{4.2c}$$

$$\dot{\psi} = p' + \left(\frac{\sin\theta\sin\psi}{\cos\theta}\right)q' + \left(\frac{\sin\theta\cos\psi}{\cos\theta}\right)r' \tag{4.2d}$$

$$\dot{\theta} = \left(\cos\psi\right)q' - \left(\sin\psi\right)r' \tag{4.2e}$$

$$\dot{\phi} = \left(\frac{\sin\psi}{\cos\theta}\right)q' + \left(\frac{\cos\psi}{\cos\theta}\right)r' \tag{4.2f}$$

Using the conservation of linear momentum in the inertial frame, $\Sigma \boldsymbol{f} = m\dot{\boldsymbol{v}}$, we get the following nonlinear equations of motion.

$$\dot{u} = \left(\frac{1}{m}\right)\begin{Bmatrix} f_x\left(\cos\theta\cos\phi\right) + f_y\left(\sin\psi\sin\theta\cos\phi - \cos\psi\sin\phi\right) \\ + f_z\left(\cos\psi\sin\theta\cos\phi + \sin\psi\sin\phi\right) \end{Bmatrix} \tag{4.3a}$$

$$\dot{v} = \left(\frac{1}{n}\right)\begin{Bmatrix} f_x\left(\cos\theta\sin\phi\right) + f_y\left(\sin\psi\sin\theta\sin\phi + \cos\psi\cos\phi\right) \\ + f_z\left(\cos\psi\sin\theta\sin\phi - \sin\psi\cos\phi\right) \end{Bmatrix} \tag{4.3b}$$

$$\dot{w} = \left(\frac{1}{m}\right)\left\{-f_x\sin\theta + f_y\cos\theta\sin\psi + f_z\cos\theta\cos\psi\right\} - g \tag{4.3c}$$

where g is the acceleration due to gravity. From the Euler's equation,

$$\Sigma\boldsymbol{\tau} = \left(\frac{\partial \boldsymbol{L}'}{\partial t}\right)_{body} + \boldsymbol{\omega}' \times \boldsymbol{L}' . \tag{4.4}$$

The angular momentum represented in the body frame is $\boldsymbol{L}' = \boldsymbol{I}\boldsymbol{\omega}'$, where

$$\boldsymbol{I} = \begin{bmatrix} I_{xx} & I_{xy} & I_{xz} \\ I_{yx} & I_{yy} & I_{yz} \\ I_{zx} & I_{zy} & I_{zz} \end{bmatrix} \tag{4.5}$$

and

$$\omega' = \begin{bmatrix} p' \\ q' \\ r' \end{bmatrix} = \begin{bmatrix} \dot{\psi} - \dot{\phi}\sin\theta \\ \dot{\theta}\cos\psi + \dot{\phi}\cos\theta\sin\psi \\ -\dot{\theta}\sin\psi + \dot{\phi}\cos\theta\cos\psi \end{bmatrix} \tag{4.6}$$

Using the relations (4.4)–(4.6) component-wise, we get the following relations for the angular velocities.

$$\dot{p}' = \left(\frac{1}{I_{xx}}\right)\begin{Bmatrix} \tau_x \cos\theta\cos\phi \; + \tau_y \left(\sin\theta\sin\psi\cos\phi - \cos\psi\sin\phi\right) \\ +\tau_z \left(\cos\psi\sin\theta\cos\phi + \sin\psi\sin\phi\right) \end{Bmatrix} \tag{4.7a}$$

$$\dot{q}' = \left(\frac{1}{I_{yy}}\right)\begin{Bmatrix} \tau_x \cos\theta\sin\phi \; + \tau_y \left(\sin\theta\sin\psi\sin\phi + \cos\psi\cos\phi\right) \\ +\tau_z \left(\cos\psi\sin\theta\sin\phi - \sin\psi\cos\phi\right) \end{Bmatrix} \tag{4.7b}$$

$$\dot{r}' = \left(\frac{1}{I_{zz}}\right)\left\{-\tau_x \sin\theta + \tau_y \cos\theta\sin\psi + \tau_z \cos\theta\cos\psi\right\} \tag{4.7c}$$

Using the perturbation formulae and the physical parameters for the Δ-platen from Table 3.1 and [61], the full state equations for small linear and angular position variations around the operating point $\boldsymbol{x}^* = \mathbf{0}$ for the levitator can be obtained and are given by

$$\begin{aligned} \dot{\boldsymbol{x}} &= A\boldsymbol{x} + B\boldsymbol{u} \\ \boldsymbol{y} &= C\boldsymbol{x} \end{aligned}, \tag{4.8}$$

In (4.8), $\boldsymbol{u} = \begin{bmatrix} \tilde{i}_1 & \tilde{i}_2 & \tilde{i}_3 & \tilde{i}_4 & \tilde{i}_5 & \tilde{i}_6 \end{bmatrix}^T$, where $\tilde{i}_{1-3}$ and $\tilde{i}_{4-6}$ are the currents in the vertical and horizontal actuators, respectively as indicated in Fig. 3.1(a). The tilde (~) above the state variables indicates that they are small-signal variables about an operating point.

$$A = \begin{bmatrix} 0 & 0 & 0 & 1 & 0 & 0 & 0 & 0 & 0 & 0 & 0 & 0 \\ 0 & 0 & 0 & 0 & 1 & 0 & 0 & 0 & 0 & 0 & 0 & 0 \\ 0 & 0 & 0 & 0 & 0 & 1 & 0 & 0 & 0 & 0 & 0 & 0 \\ 0 & 0 & 0 & 0 & 0 & 0 & 0 & 9.8100 & 0 & 0 & 0 & 0 \\ 0 & 0 & 0 & 0 & 0 & 0 & -9.8100 & 0 & 0 & 0 & 0 & 0 \\ 0 & 0 & 0 & 0 & 0 & 0 & 0 & 0 & 0 & 0 & 0 & 0 \\ 0 & 0 & 0 & 0 & 0 & 0 & 0 & 0 & 0 & 1 & 0 & 0 \\ 0 & 0 & 0 & 0 & 0 & 0 & 0 & 0 & 0 & 0 & 1 & 0 \\ 0 & 0 & 0 & 0 & 0 & 0 & 0 & 0 & 0 & 0 & 0 & 1 \\ 0 & 0 & 0 & 0 & 0 & 0 & 0 & 0 & -4.1670 & 0 & 0 & 0 \\ 0 & 0 & 0 & 0 & 0 & 0 & 0 & 0 & 12.2462 & 0 & 0 & 0 \\ 0 & 0 & 0 & 0 & 0 & 0 & 2.3475 & -6.3487 & 0 & 0 & 0 & 0 \end{bmatrix} \tag{4.9}$$

$$B = \begin{bmatrix} 0 & 0 & 0 & 0 & 0 & 0 \\ 0 & 0 & 0 & 0 & 0 & 0 \\ 0 & 0 & 0 & 0 & 0 & 0 \\ 0 & 0 & 0 & 7.8921 & -3.9460 & -3.9460 \\ 0 & 0 & 0 & 0 & 6.8347 & -6.8347 \\ 3.9460 & 3.9460 & 3.9460 & 0 & 0 & 0 \\ 0 & 0 & 0 & 0 & 0 & 0 \\ 0 & 0 & 0 & 0 & 0 & 0 \\ 0 & 0 & 0 & 0 & 0 & 0 \\ -95.6987 & -95.6987 & 204.9965 & 0 & 36.5803 & -36.5803 \\ 191.5164 & -185.7671 & -0.2849 & -45.9008 & 22.9504 & 22.9504 \\ 0 & 0 & 0 & 287.2842 & 292.3654 & 297.4250 \end{bmatrix} \quad (4.10)$$

B matrix was obtained using the linearized relations between the modal force and the perturbed states, the force transformation matrix (3.5) and the force-to-current conversion contacts. For horizontal actuator, this constant is 0.596 A/N and for vertical actuator, it is 1.192 A/N.

C. State-Space Equations for Lateral Control

To design the multivariable optimal controller for the plant, the plant model derived above is decoupled into two modes, vertical and lateral. An LQR is designed for the lateral modes (x, y and angle around the z-axis, ϕ), keeping the decoupled SISO lead-lag controllers for the vertical modes (z, angle around the x-axis, ψ and angle around the y-axis, θ). The reason for this choice is that we do not need to differentiate the position data or build a state estimator for velocity feedback, as full state feedback is provided by the laser-interferometer electronics for the lateral control.

The state vector for the lateral mode is given by $\boldsymbol{x}_p = \begin{bmatrix} x & y & \phi & u & v & r \end{bmatrix}^T$. The coupling terms between the vertical mode and the lateral mode for this choice of state vectors come due to the relations $\dot{\tilde{u}} = 9.81\tilde{\theta} + f(\boldsymbol{u})$ and $\dot{\tilde{v}} = -9.81\tilde{\psi} + f(\boldsymbol{u})$. However, both $\tilde{\theta}$ and $\tilde{\psi}$

have the maximum values on the order of 1.75 mrad and their influence on the velocities $\dot{\tilde{u}}$ and $\dot{\tilde{v}}$ are less than 1.5%. Thus, the effect of these coupling terms between the vertical and the horizontal modes can be neglected and the linearized small-signal lateral mode dynamics can be represented as follows:

$$\begin{bmatrix} \dot{\tilde{x}} \\ \dot{\tilde{y}} \\ \dot{\tilde{\phi}} \\ \dot{\tilde{u}} \\ \dot{\tilde{v}} \\ \dot{\tilde{r}} \end{bmatrix} = \begin{bmatrix} 0 & 0 & 0 & 1 & 0 & 0 \\ 0 & 0 & 0 & 0 & 1 & 0 \\ 0 & 0 & 0 & 0 & 0 & 1 \\ 0 & 0 & 0 & 0 & 0 & 0 \\ 0 & 0 & 0 & 0 & 0 & 0 \\ 0 & 0 & 0 & 0 & 0 & 0 \end{bmatrix} \begin{bmatrix} \tilde{x} \\ \tilde{y} \\ \tilde{\phi} \\ \tilde{u} \\ \tilde{v} \\ \tilde{r} \end{bmatrix} + \begin{bmatrix} 0 & 0 & 0 \\ 0 & 0 & 0 \\ 0 & 0 & 0 \\ 7.8921 & -3.9460 & -3.9460 \\ 0 & 6.8347 & -6.8347 \\ 287.2842 & 292.3645 & 297.4250 \end{bmatrix} \begin{bmatrix} \tilde{i}_4 \\ \tilde{i}_5 \\ \tilde{i}_6 \end{bmatrix}. \quad (4.11)$$

All the open-loop poles are at the origin and hence the plant is not open-loop stable. This is because of the pure-mass assumption. A more accurate plant model with coupling TFs will be derived using a closed-loop system identification method in Chapter V.

4.3 Linear Quadratic Regulation

The dynamic system in (4.11) may be represented as follows.

$$\begin{aligned} \dot{\boldsymbol{x}}_p &= A_p \boldsymbol{x}_p + B_p \boldsymbol{u}_p \\ \boldsymbol{y}_p &= C_p \boldsymbol{x}_p \end{aligned}, \quad (4.12)$$

where $\boldsymbol{x_p}$ and $\boldsymbol{u_p}$ are the state and the input vectors, respectively, and C_p is an identity matrix. Define the performance index as

$$\boldsymbol{J}(\boldsymbol{x}(\cdot), \boldsymbol{u}_p(\cdot), t_0) = \int_{t_0}^{\infty} \left(\boldsymbol{u}_p^T(t) R \boldsymbol{u}_p(t) + \boldsymbol{x}_p^T(t) Q \boldsymbol{x}_p^T(t) \right) dt \,. \quad (4.13)$$

This time-invariant infinite-time regulator problem is a minimization problem to find an optimal control $\boldsymbol{u}_p^*$ to minimize $\boldsymbol{J}$. The solution of this problem is well-known and can be found in texts on optimal control such as [78].

$$\boldsymbol{u}_p^* = -R^{-1}B^T P\boldsymbol{x}_p \tag{4.14}$$

where P is a positive-definite matrix that solves the algebraic Riccati equation,

$$PA + A^T P - PBR^{-1}B^T P + Q = 0\,. \tag{4.15}$$

The weight matrices were chosen to be

$$Q = diag\left(\begin{bmatrix} 2\times10^6 & 2\times10^6 & 2\times10^6 & 1\times10^3 & 1\times10^3 & 1\times10^3 \end{bmatrix}\right) \tag{4.16a}$$

$$R = diag\left(\begin{bmatrix} 0.1 & 0.1 & 0.1 \end{bmatrix}\right) \tag{4.16b}$$

These values were obtained after a few design iterations, starting with using acceptable values of $\boldsymbol{x}_p$ and $\boldsymbol{u}_p$ such that $Q_{ii} = 1/max\|x_{ii}\|^2$, $R_{ii} = 1/max\|u_{ii}\|^2$ in order to avoid actuator saturation and keep the state variables within the sensor limits. The optimal controller associated with the cost function defined above using the following values of weight matrices defined by (4.16) is given by

$$K = \begin{bmatrix} 3338.90 & 16.37 & 310.50 & 78.38 & 0.39 & 6.99 \\ -1626.60 & 2883.40 & 315.21 & -38.18 & 67.69 & 7.09 \\ -1626.30 & -2850.30 & 319.89 & -38.18 & -66.91 & 7.20 \end{bmatrix} \tag{4.17}$$

The closed-loop poles are placed at –50643, –965.44, –965.44, –44.77,–44.77, and –44.72 rad/s. Thus the closed-loop system has been stabilized. Since the controller is to be implemented digitally on a 320C40 DSP, we need the control gain in a discrete-time domain. The discrete feedback gain is calculated with the '`lqrd`' function in MATLAB with sampling rate of 5 kHz. Figure 4.1 shows the position, control effort required and the velocity for a 50-μm step in the *y*-direction.

It can be observed from Fig. 4.1 that there was a steady-state error of about 2 μm. This is because of the fact that the traditional LQR does not have an integrator. With the pure-mass model without friction being used, the plant transfer function should have a double pole at the

origin of the *s*-plane theoretically. However in practice, the plant poles may not be located precisely at the origin, and consequently, there can be a non-zero steady-state error. To deal with this problem, the plant model was augmented with integrators to eliminate this steady-state error. In case of maglev positioners, we are interested in position-command tracking, so I use three integrators, each for x, y, and φ.

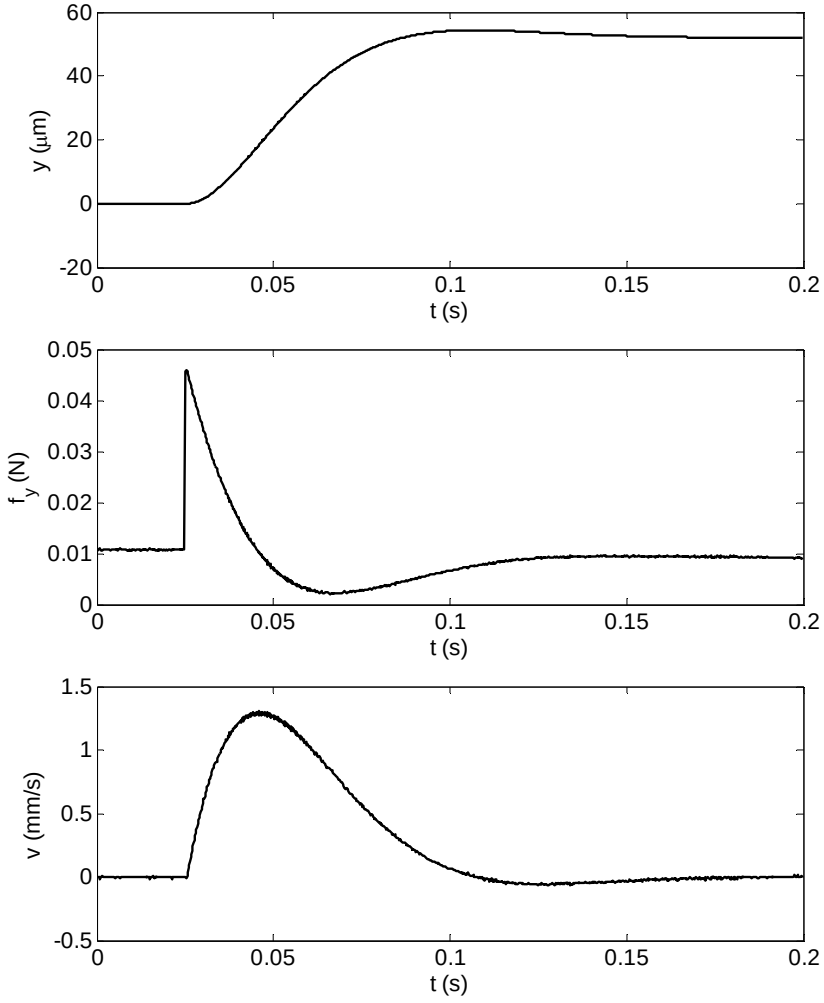

Fig. 4.1. 50-μm step response in y with an LQR without integrators

Consider again the plant represented by the differential equations in state-space form defined by (4.12). Defining the new state vector $\boldsymbol{\xi}_p$ as

$$\dot{\boldsymbol{\xi}}_p = \boldsymbol{y}_p = C_p \boldsymbol{x}_p , \tag{4.18}$$

we get the augmented system dynamics as

$$\begin{aligned} \dot{\boldsymbol{x}} &= \begin{bmatrix} \dot{\boldsymbol{x}}_p \\ \dot{\boldsymbol{\xi}}_p \end{bmatrix} = \begin{bmatrix} A_p & 0 \\ C_p & 0 \end{bmatrix} \begin{bmatrix} \boldsymbol{x}_p \\ \boldsymbol{\xi}_p \end{bmatrix} + \begin{bmatrix} B_p \\ 0 \end{bmatrix} \boldsymbol{u}_p \\ \boldsymbol{y}_p &= \begin{bmatrix} C_p & 0 \end{bmatrix} \begin{bmatrix} \boldsymbol{x}_p \\ \boldsymbol{\xi}_p \end{bmatrix} \end{aligned} . \tag{4.19}$$

To analyze the effect of the integrators and the weight matrices, I designed three different LQ controllers with the following set of Q and R.

$$Q = diag\left(\begin{bmatrix} 2\times10^6 & 2\times10^6 & 2\times10^6 & 10^3 & 10^3 & 10^3 & 10^9 & 10^9 & 10^9 \end{bmatrix}\right) \tag{4.20a}$$

$$R = diag\left(\begin{bmatrix} 1 & 1 & 1 \end{bmatrix}\right) \tag{4.20b}$$

$$Q = diag\left(\begin{bmatrix} 2\times10^6 & 2\times10^6 & 2\times10^6 & 10^3 & 10^3 & 10^3 & 10^6 & 10^6 & 10^6 \end{bmatrix}\right) \tag{4.21a}$$

$$R = diag\left(\begin{bmatrix} 0.1 & 0.1 & 0.1 \end{bmatrix}\right) \tag{4.21b}$$

$$Q = diag\left(\begin{bmatrix} 10^7 & 10^7 & 10^7 & 10^3 & 10^3 & 10^3 & 10^7 & 10^7 & 10^7 \end{bmatrix}\right) \tag{4.22a}$$

$$R = diag\left(\begin{bmatrix} 0.1 & 0.1 & 0.1 \end{bmatrix}\right) \tag{4.22b}$$

Fig. 4.2 gives a comparison among the above three controllers. As the weight on the R matrix is reduced, the required control effort increases. So is the case when the weight on the integrators is emphasized since it takes larger control effort to reach the steady state faster. Furthermore, the settling time decreases as the weight on the position states is increased, but this increase also

results in larger control effort and higher speed. Thus there exists a trade-off between the tracking and the control effort requirement, which depends on the nature of application.

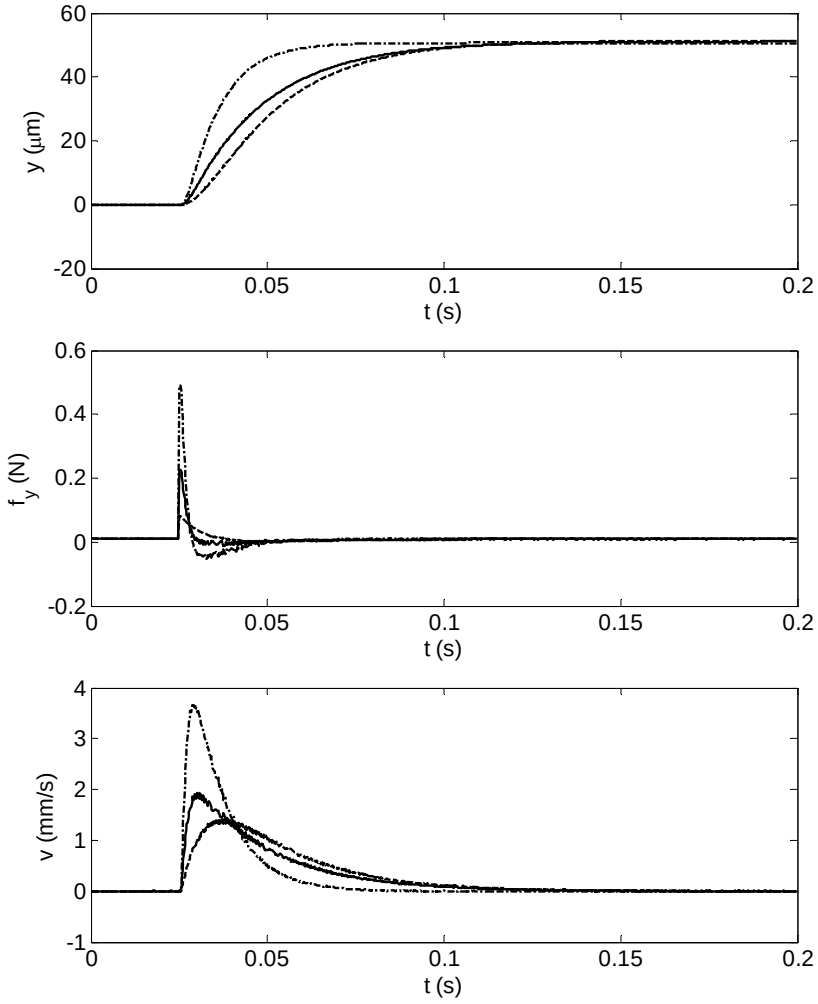

Fig. 4.2. Effect of varying the weight matrices on system response – LQ control with pair (4.20) (dashed), (4.21) (solid) and (4.22) (dash-dotted)

Fig. 4.3 shows the position, required control effort, and velocity for a 50-μm step in the *y*-axis with the weight matrices given by (4.21). With the introduction of the integrators, the steady-state error has been eliminated and the dynamic performance has been improved in terms

of the rise time, settling time, damping and overshoot as compared with the LQR without integrators. Fig. 4.4 shows the 50-µm step response in x and y, and a 50-µrad step response in the ϕ-direction with the LQR with integrators. The three plots are almost identical, thus showing that the plant model is linear and consistent in all the three axes.

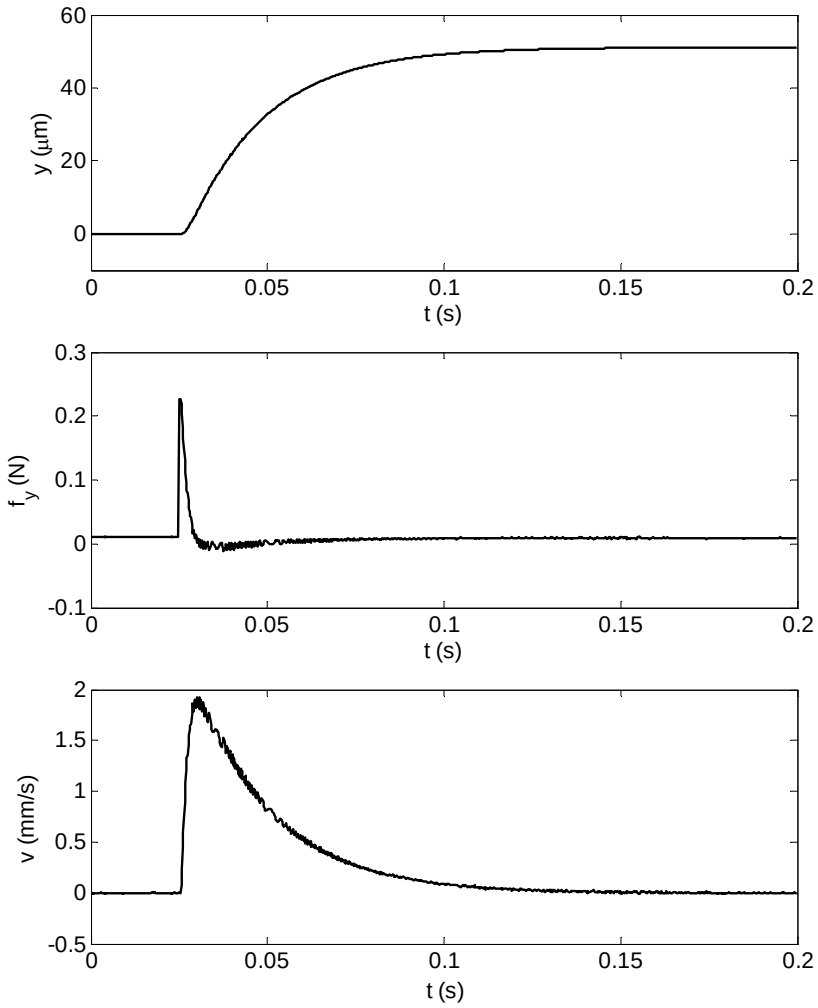

Fig. 4.3. 50-µm step response in y with the LQR with integrators

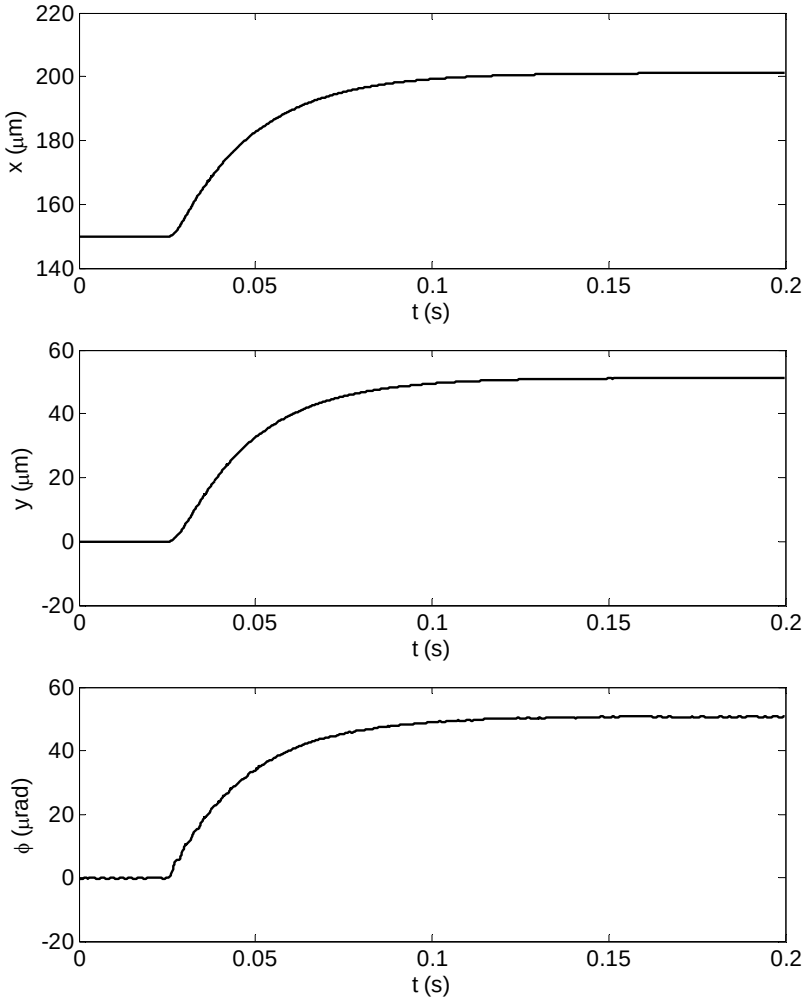

Fig. 4.4. 50-μm step responses in x and y and 50-μrad step response in ϕ with the LQR with integrators

Fig. 4.5 shows the comparison between a 48-Hz decoupled lead-lag controller given by (3.12) and the LQR with the weight matrices given by (4.21) for a 50-μm step response in the x-axis. The multivariable LQ control significantly reduced the dynamic coupling by 91.6% in y and 97.1% in ϕ. This reduction in the dynamic coupling was calculated by the percentage change in the maximum perturbation from the commanded position in y and ϕ when a step-command is given in x.

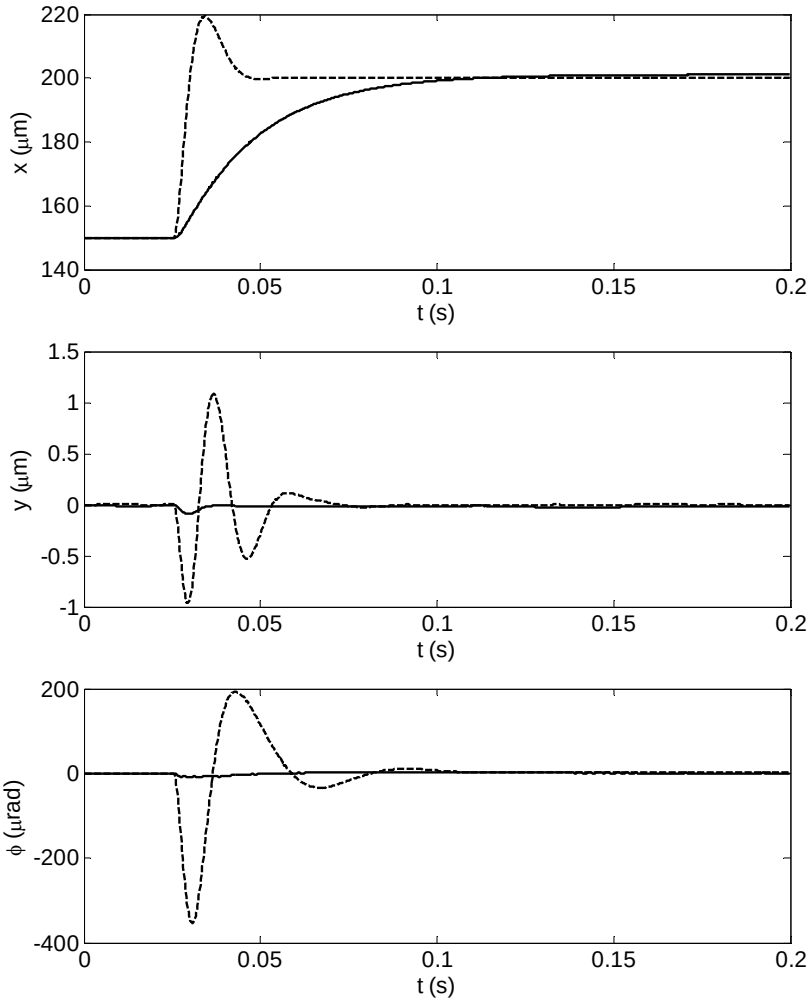

Fig. 4.5. Coupling reduction with multivariable optimal control – step response in *x* with coupled responses in *y* and rotation about *z* with LQR (solid) and decoupled SISO lead-lad control (dashed)

The control effort required and the peak velocities have also been reduced. This can be seen from Figs. 4.6 and 4.7, respectively. The maximum force required for a 50-μm step was reduced from 3.53 N for the SISO lead-lag control to 0.35 N for the LQ control. This ten-fold reduction is expected because of the choice of the *R* matrix in the controller design, whose function is to suppress the control-effort requirement. Likewise, the peak velocity was reduced

by 85.89% from 14.03 mm/s for the lead-lag control to 1.98 mm/s for the LQ control. The reduction in coupling in the other two axes, namely y and ϕ, is also commensurate to the reduction observed in the Fig. 4.5.

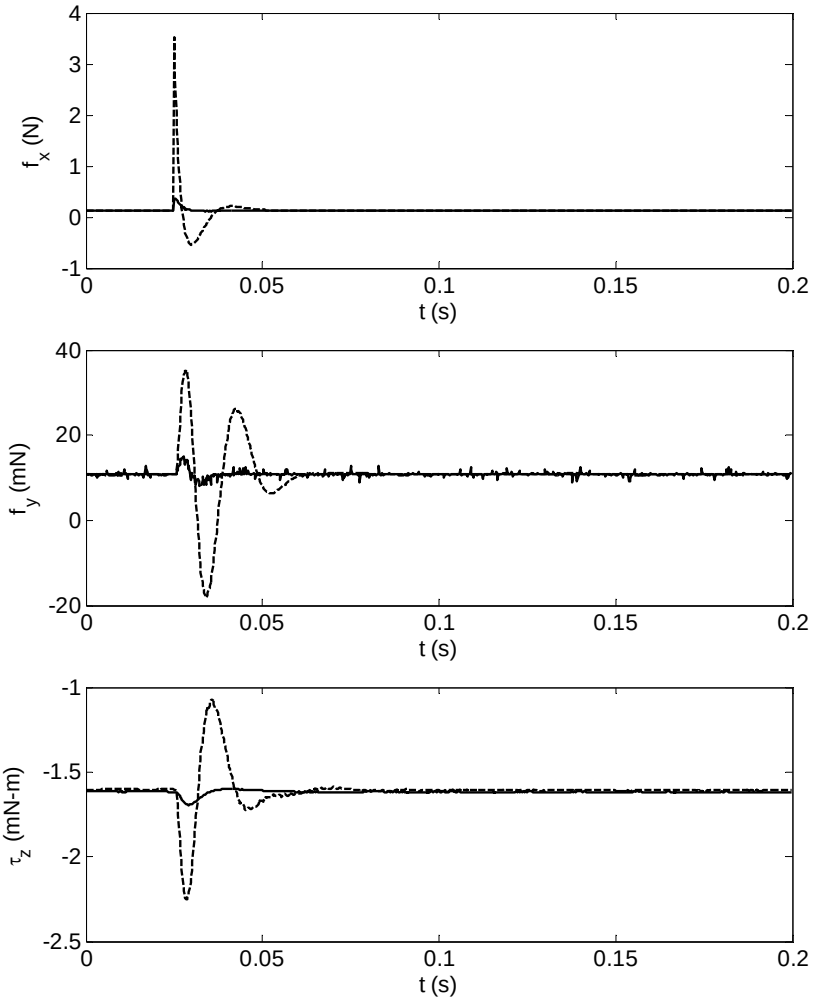

Fig. 4.6. Reduction in control effort required with multivariable optimal control – step response in x with LQR (solid) and decoupled SISO lead-lag control (dashed)

One of the shortcomings of the multivariable control is that it has adversely affected the dynamic performance in terms of the settling time. It takes 86 ms using the LQR to reach the

steady-state using a 5% criterion against 43 ms in case of the lead-lag control. However, this time difference is insignificant for the practical applications that work at a much slower rate. This will be demonstrated in further details using some examples in Chapter VI.

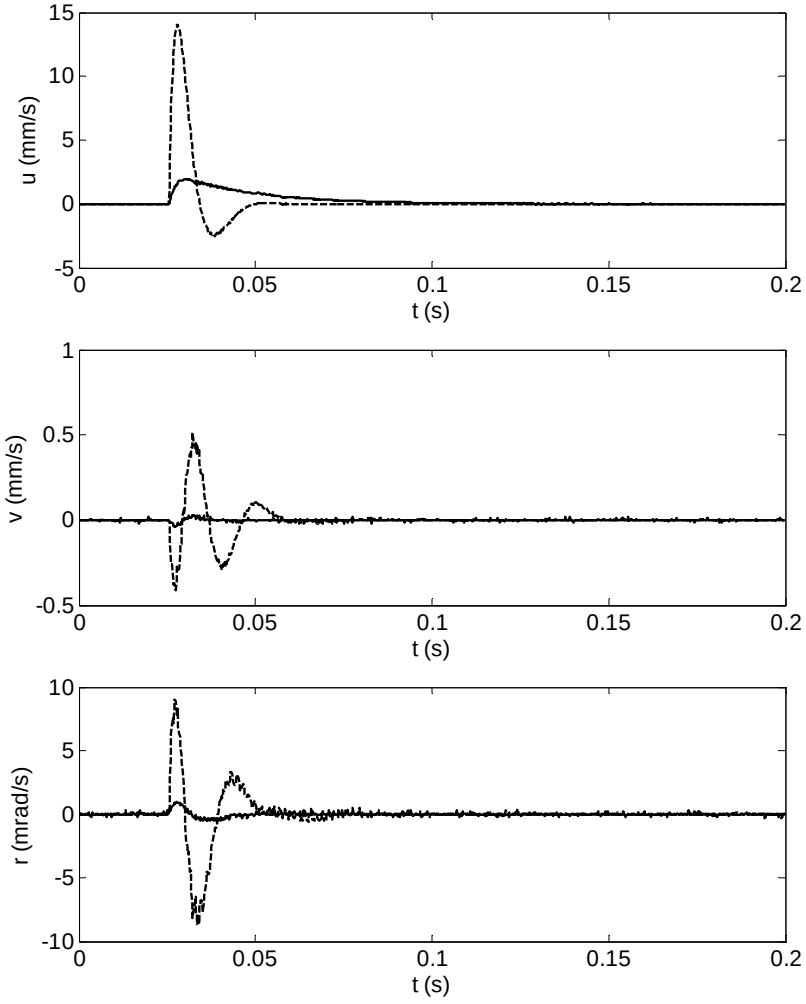

Fig. 4.7. Reduction in the peak velocities with multivariable optimal control – step response in *x* with LQR (solid) and decoupled SISO lead-lag control (dashed)

4.4 Summary

In this chapter, primary focus was to reduce the coupling among the axes for two maglev nanopositioners. Multivariable optimal control is a natural choice for this purpose. Nonlinear equations of motion were derived using the Euler-angle approach, and a linearized plant model in state-space form was developed about an operating point. For position regulation, I designed and implemented a multivariable LQR for lateral dynamics, continuing to use the decoupled SISO lead-lag controllers for the vertical motion control. An augmented system was also designed with integrators to reduce the steady-state errors in the x-, y- and ϕ-axis. Step responses using the designed controllers without and with integrators were presented, and the performance of the controllers with different weight matrices was compared.

A comparison between the multivariable LQ controller and the decoupled SISO lead-lag controller reveals a reduction in coupling by about 97%. The control effort required for a given step size was reduced by a factor of 10. The peak velocity was also found to be reduced by 85.89%. It may be concluded from the experimental results that the objectives of reduction in coupling as well as the control effort requirement were met with the designed LQ control. However, the performance was found to be adversely affected in terms of settling time. In fact, there is inherently a trade-off between position accuracy and response time, which cannot be resolved using the traditional optimal control techniques discussed in this chapter. This issue of conflicting time-domain performance specifications will be addressed in Chapter VII. Conventional optimal PI techniques discussed in this chapter will be revisited to derive motivation for what will be called *multiscale* control.

CHAPTER V

SYSTEM IDENTIFICATION

5.1 Introduction

As demonstrated in the Chapter III (Figs. 3.8 and 3.9), the developed maglev positioners have inherent coupling among the axes since a single part is used to generate all 6-axis motions. This problem is more prominent in the extended-range Y-stage since it allows large travel ranges and consequently more coupling. Since the rotational sensing range of the laser interferometers being used for the horizontal motion sensing is limited to 3.5 mrad, this cross-talk among the axes may result in the system instability due to loss of sensing data, in addition to producing undesired motions. One of the objectives of this research is to have a working space as large as the designed travel range, which implies that the performance of the positioner must be uniform throughout the working space. System identification is necessary in order to analyze and model the plant behavior accurately and to subsequently develop effective control strategies. It is also required to reduce the effect of unmodeled dynamics and nonlinearity in the actuators which may be difficult to model precisely using analytical methods.

In case of maglev systems being used, system identification is not only crucial but also challenging because of their inherently unstable nature. Thus the system identification needs to be performed in closed loop. In this research, I carry closed-loop identification one step ahead of the traditionally used input-output identification techniques in order to obtain a more reliable, consistent, and complete plant model. The BJ method with a closed-loop framework and a known controller structure will be used to obtain the closed-loop TF [22, 23]. A plant TF will be

then derived from the identified closed-loop TF and controller TF. An order-reduction algorithm will be presented to obtain a TF which gives a close match in the frequency range of interest without loosing any significant plant dynamics. The entire analysis will be performed in discrete time in order to avoid any errors due to continuous-to-discrete-time conversion and vice versa. Continuous time TFs will be used only for order-reduction and performance analysis of the identified plant TFs.

5.2 Analytical Model

Elementary plant modeling performed for the maglev positioners was presented in Chapter IV using the Newtonian method with the Euler angles. The dynamic model for the horizontal mode of the positioners used in the current analysis remains the same in principle. This linearized analytical model is given by

$$\begin{bmatrix} \tilde{X}(s) \\ \tilde{Y}(s) \\ \tilde{\Phi}(s) \end{bmatrix} = \begin{bmatrix} G_{xx}(s) & G_{xy}(s) & G_{x\phi}(s) \\ G_{yx}(s) & G_{yy}(s) & G_{y\phi}(s) \\ G_{\phi x}(s) & G_{\phi y}(s) & G_{\phi\phi}(s) \end{bmatrix} \begin{bmatrix} \tilde{F}_x(s) \\ \tilde{F}_y(s) \\ \tilde{T}_\phi(s) \end{bmatrix} + \begin{bmatrix} H_x(s) & 0 & 0 \\ 0 & H_y(s) & 0 \\ 0 & 0 & H_\phi(s) \end{bmatrix} \begin{bmatrix} E_x(s) \\ E_y(s) \\ E_\phi(s) \end{bmatrix}, \quad (5.1)$$

where $\tilde{X}(s)$, $\tilde{Y}(s)$, and $\tilde{\Phi}(s)$ are the Laplace transforms of the perturbations of the horizontal positions and the yaw angle from their respective operating points; $\tilde{F}_x(s)$, $\tilde{F}_y(s)$, and $\tilde{T}_\phi(s)$ are the respective transforms of the plant inputs; $E_x(s)$, $E_y(s)$, and $E_\phi(s)$ are the output noises; and $G(s)$ and $H(s)$ are plant and noise TFs, respectively. In an ideal linearized dynamic model, each diagonal term of the plant TF matrix could be considered as a double integrator,

$$G_{xx}(s) = G_{yy}(s) = \frac{1}{ms^2}, \; G_{\phi\phi}(s) = \frac{1}{I_{zz}s^2}, \quad (5.2)$$

where m is the mass of the platen and I_{zz} is the principal moment of inertia about the z-axis. The off-diagonal terms and noise TF terms might be ignored in an ideal model.

5.3 Closed-Loop System Identification

5.3.1 BJ Method

System identification is required to validate the analytical model (5.1)–(5.2) and to identify the dynamic coupling among the axes due to the non-ideal actuators and mechanical structure of the positioner, and uncertainties in its assembly. Open-loop tests cannot be performed due to the inherently unstable nature of the maglev system. Subsequently, the identification of the experimental system is carried out on the closed-loop system after the maglev positioner is stabilized around the operating point with decoupled lead-lag controllers. The BJ identification method for this closed-loop framework with a known controller dynamics was used for each DOF [22, 23]. The schematic of this method is shown in Fig. 5.1. Since the system identification procedure is carried out in discrete time, the continuous-time model in (5.1) was transformed into difference equations using the zero-order-hold (ZOH) method and with a sampling frequency of 5 kHz. The discrete-time TF for $\tilde{x}$, for example, is given by

$$\begin{aligned}\tilde{X}(k) &= \frac{B_x(q)}{A_x(q)}R_x(k) + \frac{C_x(q)}{D_x(q)}E_x(k) \\ &= \frac{G_{xx}(q)M_x(q)}{1+G_{xx}(q)M_x(q)}R_x(k) + \frac{H_x(q)}{1+G_{xx}(q)M_x(q)}E_x(k)\end{aligned} \tag{5.3}$$

under certain assumptions [22, 23, and 24], where $G(q)$, $H(q)$, and $M(q)$ are rational TFs, $R(k)$ is the reference input signal, $M(q)$ is the known controller TF, and $q = z^{-1}$. Due to the

chosen structure for the parameterization of the plant and noise models, namely the BJ method, the TFs $G(q)$ and $H(q)$ are parameterized independently.

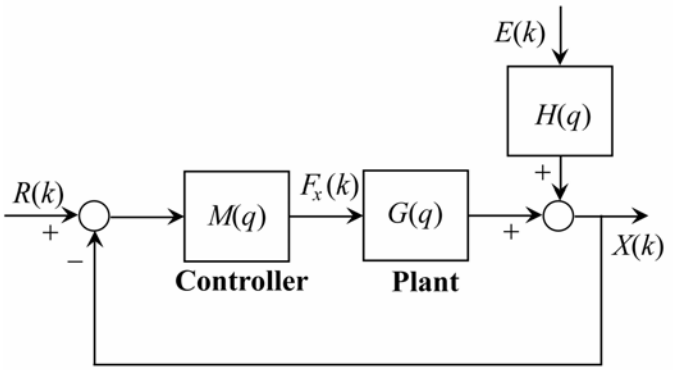

Fig. 5.1. Block diagram representing the BJ method for identification in closed loop with a known controller dynamics

Since we have full control over the excitation signal, it is desired to use the signals that persistently excite the plant [24]. Thus, the model validation was performed with two different experiments using (1) a zero-mean, white-Gaussian noise (WGN) and (2) a chirp signal. In the first case, I applied a stochastic system identification methodology that uses a random reference input. A detailed treatment of stochastic modeling is covered in classical texts such as [79]. The random disturbance was generated in software using the "`rand()`" function in the C language. The magnitudes of the random signals were chosen to be linearly increasing from 0.1 to 10 μm. In a second experiment, I used a chirp signal with a magnitude of 1 μm, starting from DC and crossing 2500 Hz at 2 s. These numbers were chosen to excite the plant persistently without loosing stability. The total time of the excitation in both the cases was 2 s with a sampling rate of 5 kHz. It is to be noted that these experiments were performed about the operating point, which is $\begin{bmatrix} \tilde{x}_0 & \tilde{y}_0 & \tilde{\phi}_0 \end{bmatrix}^T = \mathbf{0}$. Due to feedback linearization, the model is essentially position-invariant in the operating travel range.

The experimental results of the system identification using the two above-mentioned methods are presented in Fig. 5.2. The figure shows the closed-loop system responses to the two reference signals, the respective identified TFs, and the ideal closed-loop TFs. It is evident from the figure that the chirp signal gives a much better and neater fit to the identified TFs. Thus, I decided to pursue further analysis on system identification with the chirp signal using the BJ method. Another reason for choosing the chirp signal is that it meets the condition of persistent excitation on the reference input signal better than the stochastic signal. Besides, the stochastic modeling is based on the assumption that the signal is zero-mean WGN, and this theoretical assumption may not be applicable to the conducted experiment.

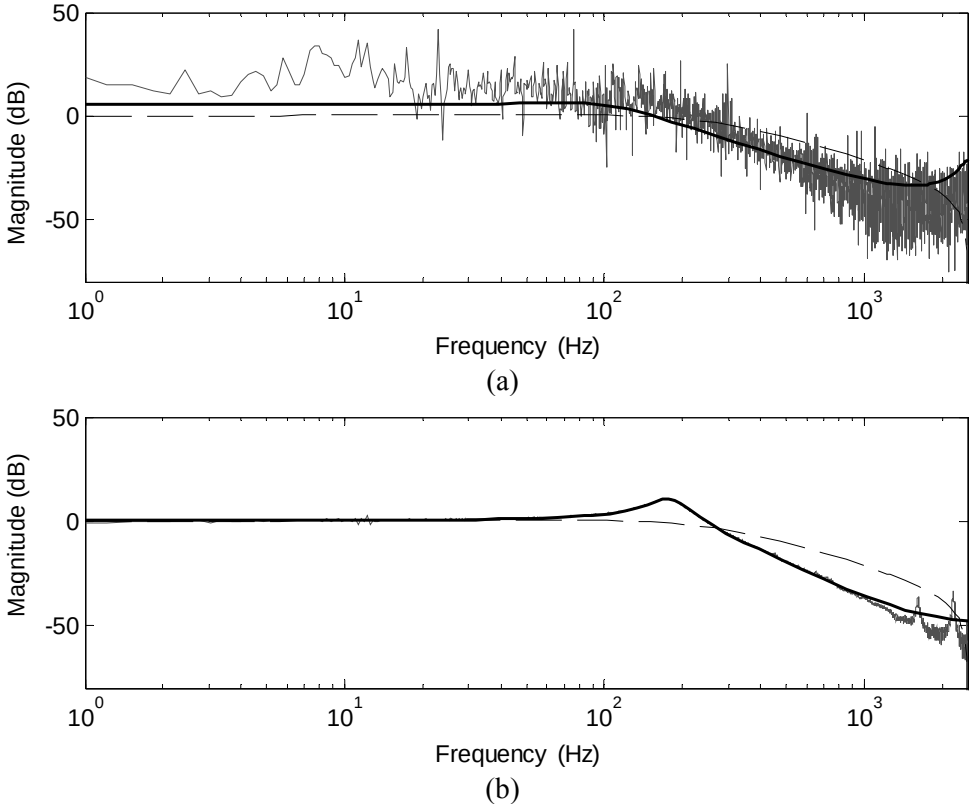

Fig. 5.2. Closed-loop system frequency responses in x with (a) the stochastic input signal and (b) the chirp input signal – Bode magnitude plots of the analytical model (dashed line), the plant TFs from the FFTs of the input-output signals (thin solid line), and the identified TFs using the BJ method (thick solid line)

Fig. 5.3 shows the 1-μm chirp signal given in x, with frequencies ranging from DC to 2500 Hz and the response of the system in x, y, and ϕ. The total time of excitation was 2 s. Figs. 5.4 and 5.5 show similar plots with excitation in y and ϕ, the responses in the respective axes and the coupled responses. It may be seen from these plots that the plant follows the chirp signal closely in the low-frequency range, around [0, 50] Hz. It, however, amplifies the input in the intermediate-frequency range, and attenuates, in the high-frequency range. This is in agreement with the closed-loop TF identified in Fig. 5.2(b), which shows a resonance in the frequency range of [50, 250] Hz and a steep roll-off thereafter.

It may be noted from Figs. 5.3 and 5.4 that coupling in x for excitation in y is more compared to coupling in y for excitation in x. This may be attributed to the fact that the forces in y which gets cancelled are the smaller ($1/2\times$) components of the actuator forces F_5 and F_6 (refer to Fig. 3.1). However, the canceling components for x for a desired effective motion in y come from the larger ($\sqrt{3}/2\times$) components of the forces F_5 and F_6. Therefore, if there is any net non-zero force in the coupling axes due to misalignments or modeling uncertainties, the effect of such a force will be more prominent in x compared to y. Contrarily, the coupling in ϕ is more for excitation in x compared to excitation in y. The reason for this may be explained as follows. The amount of canceling forces in ϕ is the same for both the cases. However, in case of x, components from two forces, namely F_5 and F_6, get cancelled, while in case of y, components from F_4 and F_5, and F_6 get cancelled. Therefore, if there is any misalignment in the actuators or position of the maglev stage with respect to the actuators, the effect of such misalignments and modeling uncertainties will be averaged over two forces in case of x while three forces in case of y. Accordingly, the net coupling will be less in case of the y-excitation. Finally, from Fig. 5.5, it may be noted that the coupling in x and y is minimal for the excitation in ϕ, and the responses in

these two axes is almost the same as that of regulation. This comparison will be discussed in more detail in terms of the frequency response, and plant and coupling TFs later in this chapter.

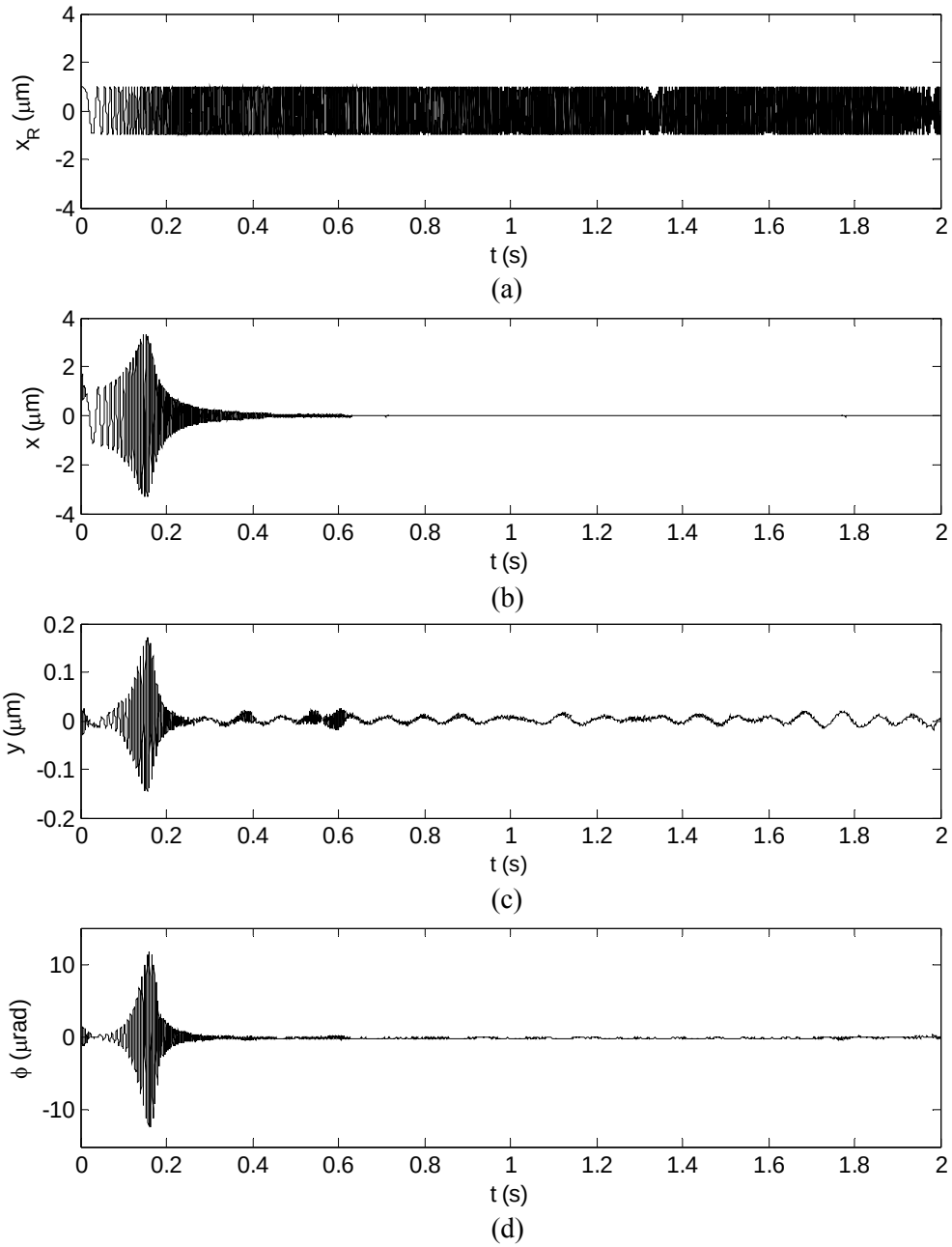

Fig. 5.3. System time response to a chirp signal. (a) Input chirp signal given in x with a frequency range of [0, 2500] Hz, (b) response in x, (c) coupled response in y, a factor of 20 smaller in magnitude compared with x, and (d) coupled response in ϕ

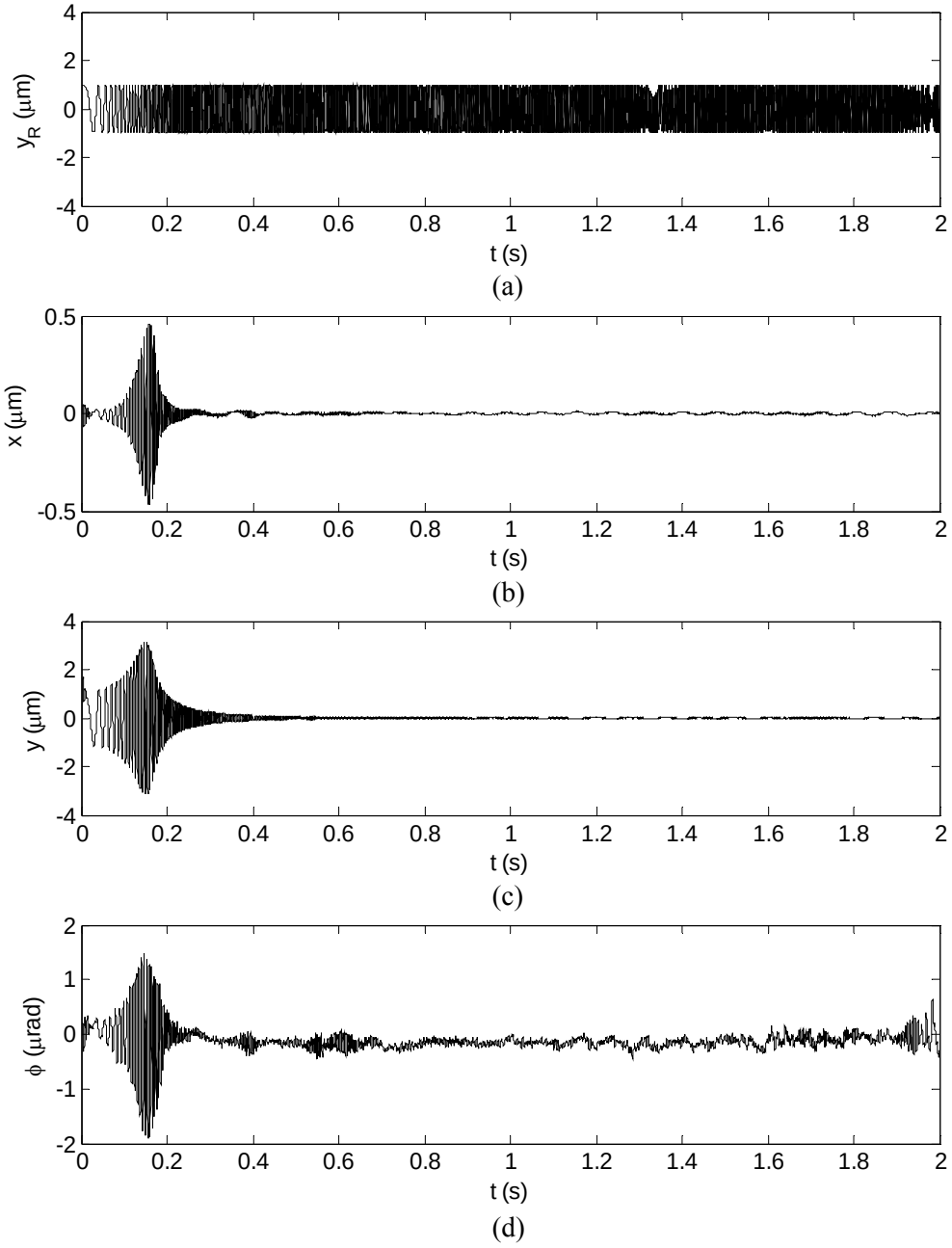

Fig. 5.4. System time response to a chirp signal. (a) Input chirp signal given in y with a frequency range of [0, 2500] Hz, (b) coupled response in x, a factor of 8 smaller in magnitude compared with y, (c) response in y, and (d) coupled response in ϕ

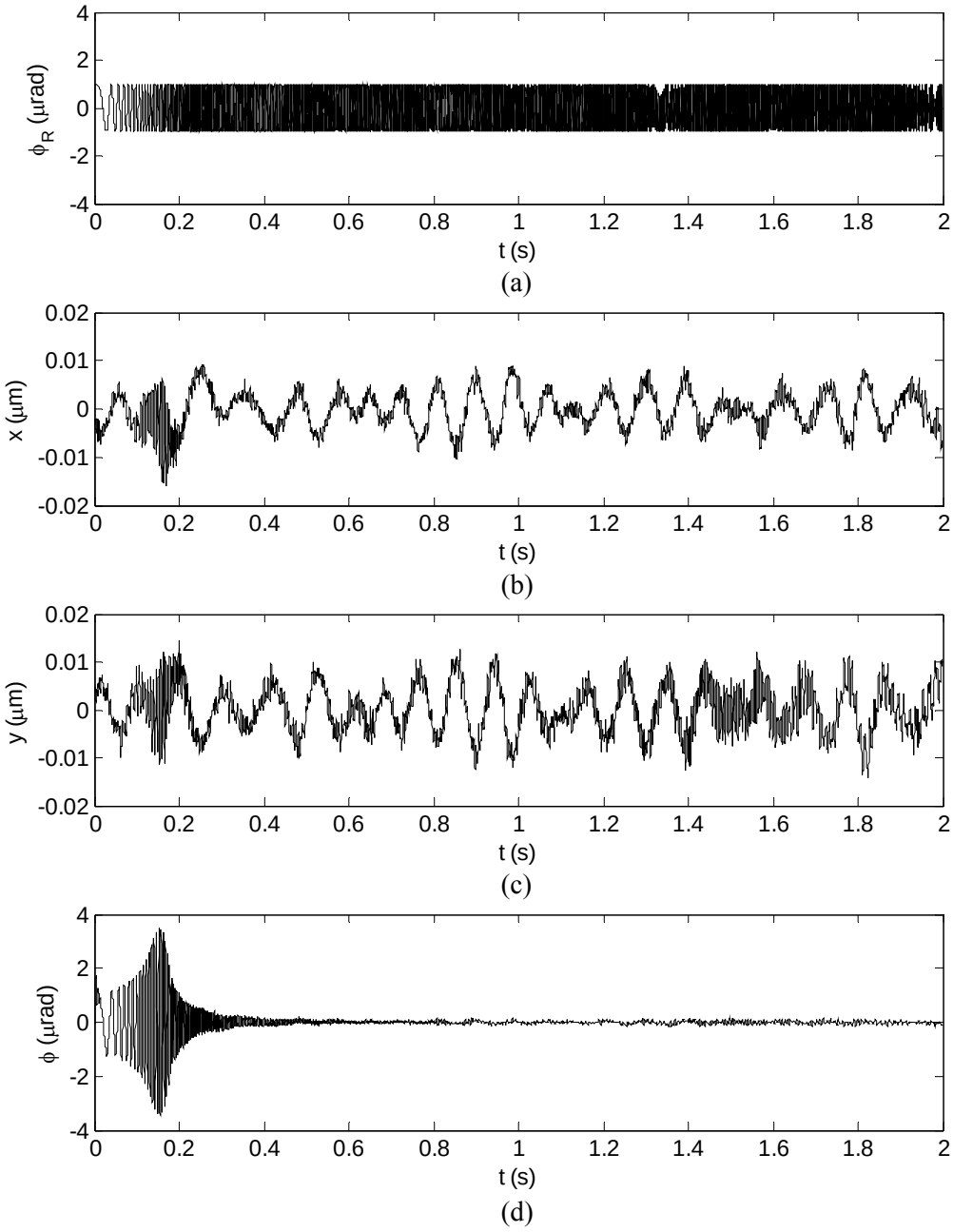

Fig. 5.5. System time response to a chirp signal. (a) Input chirp signal given in ϕ with a frequency range of [0, 2500] Hz, (b) coupled response in x, (c) coupled response in y, and (d) response in ϕ

5.3.2 Closed-Loop Identification Algorithm

From the reference input signal in the three axes and measured output in the respective axes as well as coupled axes, all 9 TFs of the system matrix in (5.1) may be identified. Model identification was performed with MATLAB using an algorithm consisting of following steps.

Step-1: *Data packaging* – MATLAB function `iddata(y,u,Ts)` is used to package the input-output data into a data object to be subsequently used for identification. *u* and *y* in this function are input and output column vectors, respectively, and T_s is the sampling interval.

Step-2: *Identification of closed-loop TF* – In the this step, the parameters of the polynomials *A*, *B*, *C*, and *D* given in (5.3) are identified using the MATLAB function `pem(data,orders)`. The argument *data* of this function is the packaged data from Step-1. The model orders may be specified as `orders = [nf, nb, nc, nd, na, nk]`, where n_a, n_b, n_c, n_d and n_f are the desired orders of the auto-regressive moving average with exogenous input (ARMAX) model, and n_k is the delay. The MATLAB function `pem` essentially uses the same algorithm for identification as ARMAX model, with modifications in the computation of prediction errors and gradients. It returns an identified polynomial object with the resulting parameter estimates, together with estimated covariances using a prediction error method.

The structure of the model to be identified is given by

$$F(q)Y(k)=\frac{B(q)}{A(q)}U(k-n_k)+\frac{C(q)}{D(q)}E(k). \tag{5.4}$$

It may be noted that (5.3) is a special case of the general structure given by (5.4). Furthermore, the ratio of the norms of the sensor noise sequence $E(k)$ to output sequence $R(k)$ is about 0.0079. Thus the contribution from the sensor noise in (5.3) may be ignored. Let's define the closed-loop TF as $T(q)$, where

$$T(q) = \frac{G(q)M(q)}{1 + G(q)M(q)} = \frac{B(q)}{A(q)}. \tag{5.5}$$

Here the subscripts used in (5.3) were dropped for simplicity. Let $[n_G^c,\ d_G^c]$ and $[n_M^c,\ d_M^c]$ be the orders of the numerator and denominator polynomials of the continuous-time plant and controller TFs, respectively. Then, from the analytical plant model given by (5.2) and the stabilizing lead-lag controller design, we have

$$\begin{aligned} [n_G^c,\ d_G^c] &= [0,\ 2] \\ [n_M^c,\ d_M^c] &= [2,\ 2] \end{aligned}. \tag{5.6}$$

Therefore, the order for the desired discrete-time closed-loop TF from (5.5) is

$$\texttt{[na, nb]} = [n_A^d,\ n_B^d] = [3,\ 4]. \tag{5.7}$$

Here the superscripts *c* and *d* signify continuous-time and discrete-time TFs, respectively, and the subscripts *A* and *B* signify the numerator and denominator polynomials of the closed-loop TF $\frac{B(q)}{A(q)}$ in (5.3). Then n_k is set to 1.

Step-3: *Deduction of plant TF* – The discrete-time plant model was obtained from the closed-loop TF identified in Step 2 as follows. Rearranging (5.5), we get

$$G(q) = T(q)\left(M(q) - M(q)T(q)\right)^{-1}, \tag{5.8}$$

Using (5.3) with the closed-loop TF orders (5.7) and the relation (5.8), we obtain the high-order identified plant TFs. For the purpose of order reduction and analysis of the frequency-domain behavior of the identified plant model, the TF was converted to continuous time model using zero-order-hold (ZOH) method. The high-order continuous-time TF for *x*, for example, is given by

$$G_{xx}(s) = 3.1435\times10^{-5}\frac{\begin{array}{r}\left[s^2(s+4014)^2\left(s^2+335s+1.2750\times10^6\right)\left(s^2+6102+1.1090\times10^7\right)\right]\\ \cdot\left[(s+13123)(s+18202)\left(s^2-9947s+3.4330\times10^7\right)\right]\end{array}}{\begin{array}{r}\left[s(s+11.4763)(s+4014)(s+4042)\right.\\ \left.\cdot\left(s^2+335s+1.2750\times10^6\right)\left(s^2+6102+1.1090\times10^7\right)\right]\\ \cdot\left[(s-54.6250)(s+76.9111)\right]\left[s^2+2450s+4.2460\times10^6\right]\end{array}} \tag{5.9}$$

The pole-zero map of this TF is shown in Fig. 5.6(a) and the magnitude of the TF is shown in Fig. 5.7(a) with a thin solid line.

Step-4: *Order reduction* – Although the identified TF (5.9) is 12-th order, there are several pole-zero pairs at the same locations as seen in Fig. 5.6(a) because of the way in which the TF was deduced in Step 3. These pole-zero cancellations reduce the order of the plant significantly. The order may be further reduced by eliminating the zeros much faster than the closed-loop system dynamics, and making the required adjustments in the TF magnitude. Finally, with the remaining poles and zeros, the dynamics of the system can be divided into two modes – the first mode is the slowest and very close to a double-integrator. This mode is of greatest interest in the design of a controller since it represents the rigid-body dynamics of the maglev positioner. The second mode corresponds to the mechanical vibrations of the maglev positioner with resonant frequency around 325 Hz and can be ignored in the plant model since the designed

controller has a control bandwidth of about 60 Hz and is not expected to excite these high frequency modes.

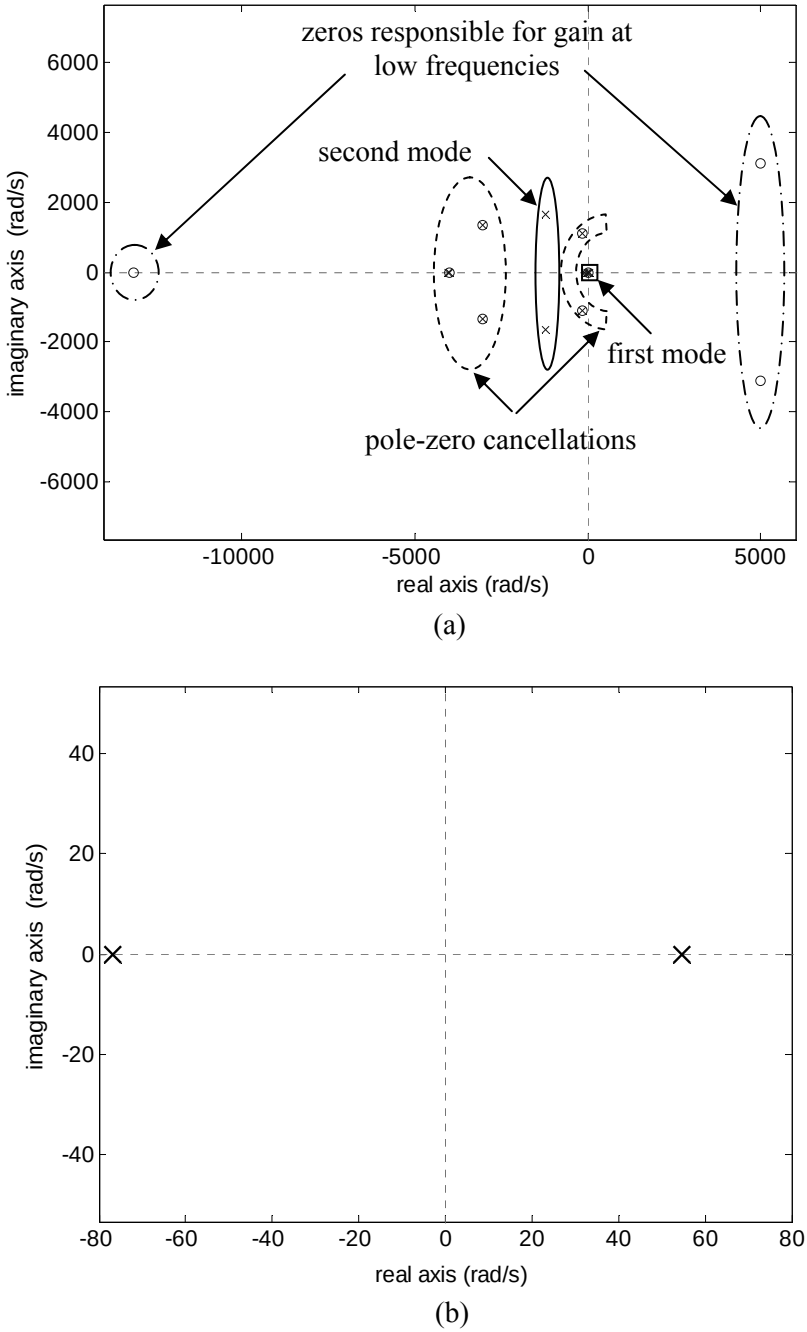

Fig. 5.6. Pole-zero map of (a) the identified TF and (b) the reduced-order TF (first mode) in *x*

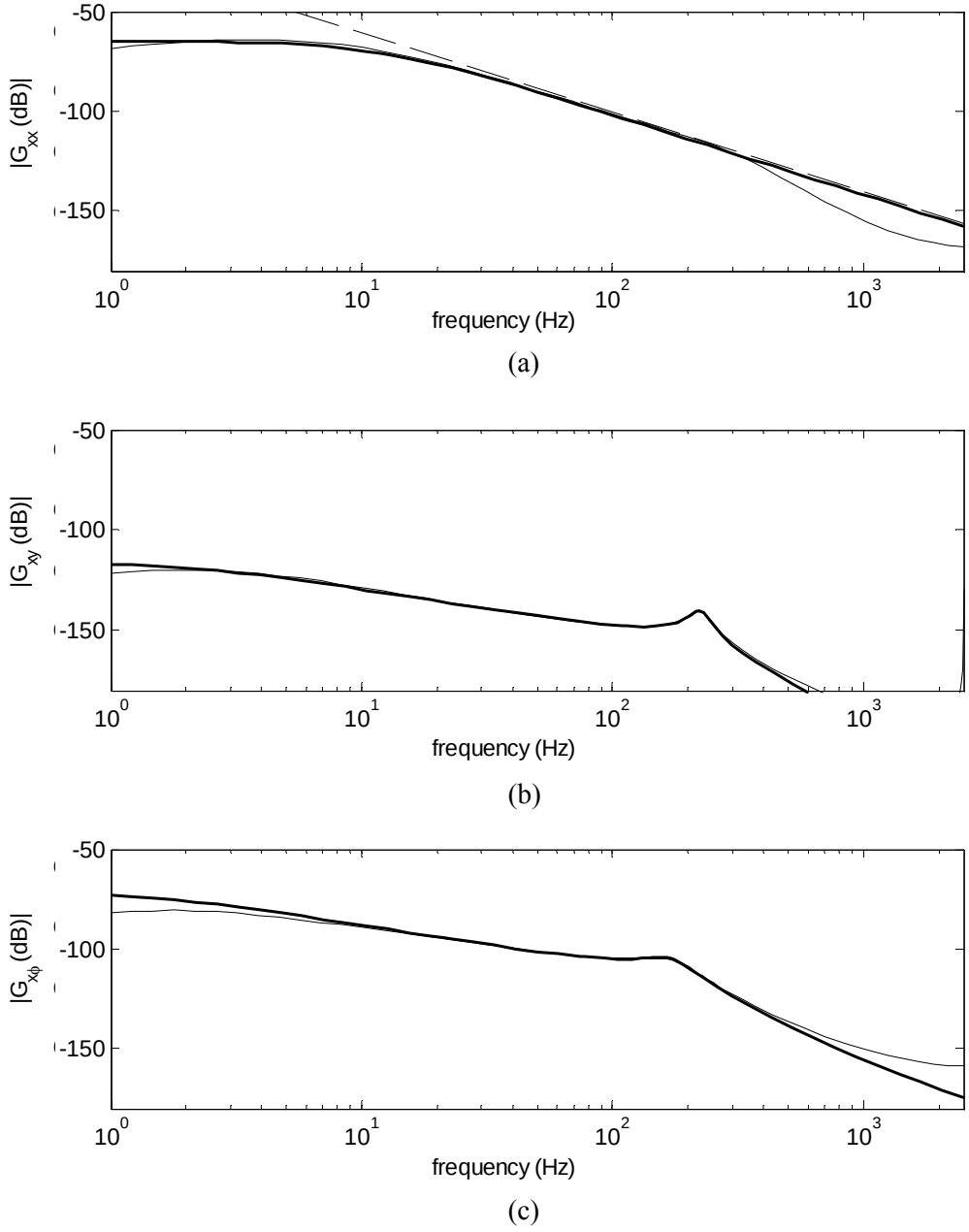

Fig. 5.7. Analytical plant TFs (dashed line), identified plant TFs (thin solid line) and reduced-order fit (thick solid line) from (a) x to x, (b) x to y, and (c) x to ϕ

5.3.3 Reduced-Order Identified TF models

With the order reduction described in the previous subsection, the order of the plant TF becomes $[n_G^c,\ d_G^c]_{identified} = [0,\ 2]$. The reduced-order TF fit so obtained is shown in the Fig. 5.7(a) with a thick solid line. It matches the identified TF in the frequency range of [20, 300] Hz within an error of 1%. This error is defined as $\varepsilon = \left|\left(P_i - P_r\right)/P_i\right|$, where P_i and P_r are the magnitudes of the identified plant TFs and their corresponding reduced-order fits. The TFs for the coupled terms are obtained in a similar manner and are shown in the Fig. 5.7(b) and (c). The plant and coupling TFs for y and ϕ are shown in Figs. 5.8 and 5.9, respectively. These identified continuous-time TFs are given by

$$G_{xx}(s) = 3.1845\frac{1}{(s-54.62)(s+76.91)} \tag{5.10a}$$

$$G_{xy}(s) = 42.4017\frac{1}{(s+13.83)\left(s^2+219.40s+1.98\times10^6\right)} \tag{5.10b}$$

$$G_{x\phi}(s) = 0.4266\frac{(s-6977.00)}{(s-9.74)\left(s^2+451.50s+1.17\times10^6\right)} \tag{5.10c}$$

$$G_{yy}(s) = 3.1623\frac{1}{(s-82.21)(s+76.91)} \tag{5.11a}$$

$$G_{yx}(s) = 114.9298\frac{1}{(s+105.91)\left(s^2+131.00s+1.09\times10^6\right)} \tag{5.11b}$$

$$G_{y\phi}(s) = 964.3725\frac{1}{(s+322.80)\left(s^2+65.59s+7.29\times10^5\right)} \tag{5.11c}$$

$$G_{\phi\phi}(s) = 1530.1985\frac{1}{(s-86.73)(s+76.91)} \tag{5.12a}$$

$$G_{\phi x}(s) = 0.1411 \frac{(s - 934.60)}{(s + 76.91)(s^2 + 586.20s + 2.53 \times 10^5)} \tag{5.12b}$$

$$G_{\phi y}(s) = 0.9065 \frac{1}{(s + 76.91)(s + 315.60)} \tag{5.12c}$$

The right-half-plane poles identified in (5.10a), (5.11a), and (5.12a) correctly reflect the maglev system's open-loop instability due to the negative spring constants of the magnetic origin. The frequency responses of the identified plant models are represented in Figs. 5.7, 5.8, and 5.9. These plots show the analytical plant models (thin dashed lines) from (5.2), the identified plant models (thin solid lines) from (5.9) using the BJ method from the input-output time sequences, and the reduced-order fits (thick solid lines) from (5.10)–(5.12). From these frequency responses, it is apparent that there are certain mismatches between the analytical and identified models. The mismatch in the low-frequency range is due to the fact that the plant TFs are indeed not of pure double-integrators but consist of two real poles at different locations with the existence of magnetic springs in the actuators. In the high-frequency range, the mismatch may be due to unmodeled dynamics. However, in the interesting frequency range of [20, 300] Hz, the two models exhibit an almost perfect match. In addition to this match in frequency domain, time-domain behavior, particularly the transient response, of the order-reduced TFs is also important. This match will be demonstrated later in this subsection (Fig. 5.10).

Other identified TFs of interest are the off-diagonal ones in (5.1) that may be used to reduce the dynamic coupling among the axes. These TFs are also presented in Figs. 5.7, 5.8, and 5.9. The order of the reduced-order TFs are identically chosen to be 3 for all the coupling terms for consistency and ease of controller design using this information. A comparison between the TFs $G_{xy}(s)$ and $G_{yx}(s)$ shows that the peak value of the plot is greater for $G_{yx}(s)$, particularly in the frequency range [50, 250] Hz. Similarly, comparing $G_{x\phi}(s)$ and $G_{y\phi}(s)$, it may be

observed that the magnitude of the $G_{x\phi}(s)$ TF is greater. This is in agreement with the response plots (5.3)–(5.5) discussed earlier in this chapter.

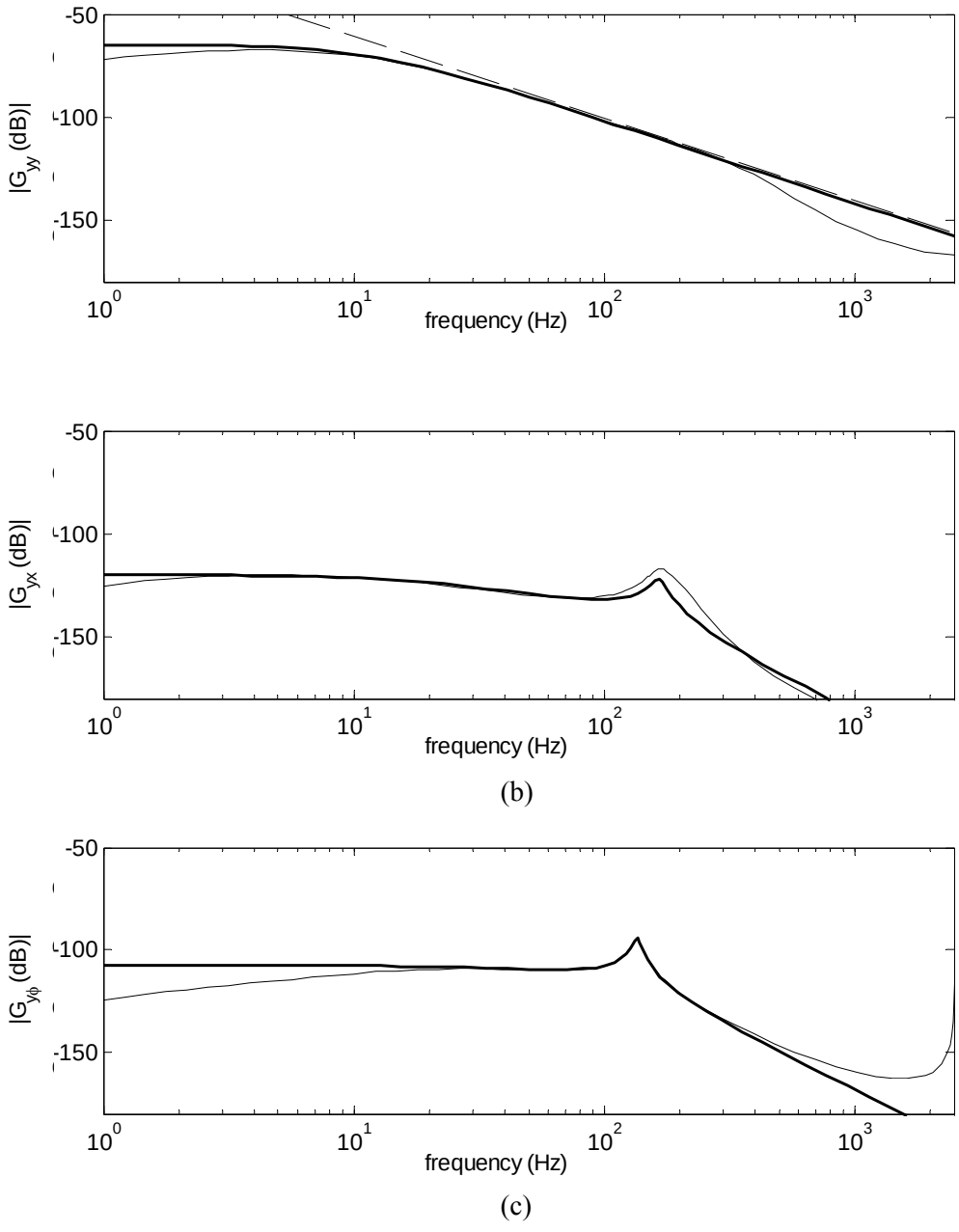

Fig. 5.8. Analytical plant TFs (dashed line), identified plant TFs (thin solid line) and reduced-order fit (thick solid line) from (a) *y* to *y*, (b) *y* to *x*, and (c) *y* to ϕ

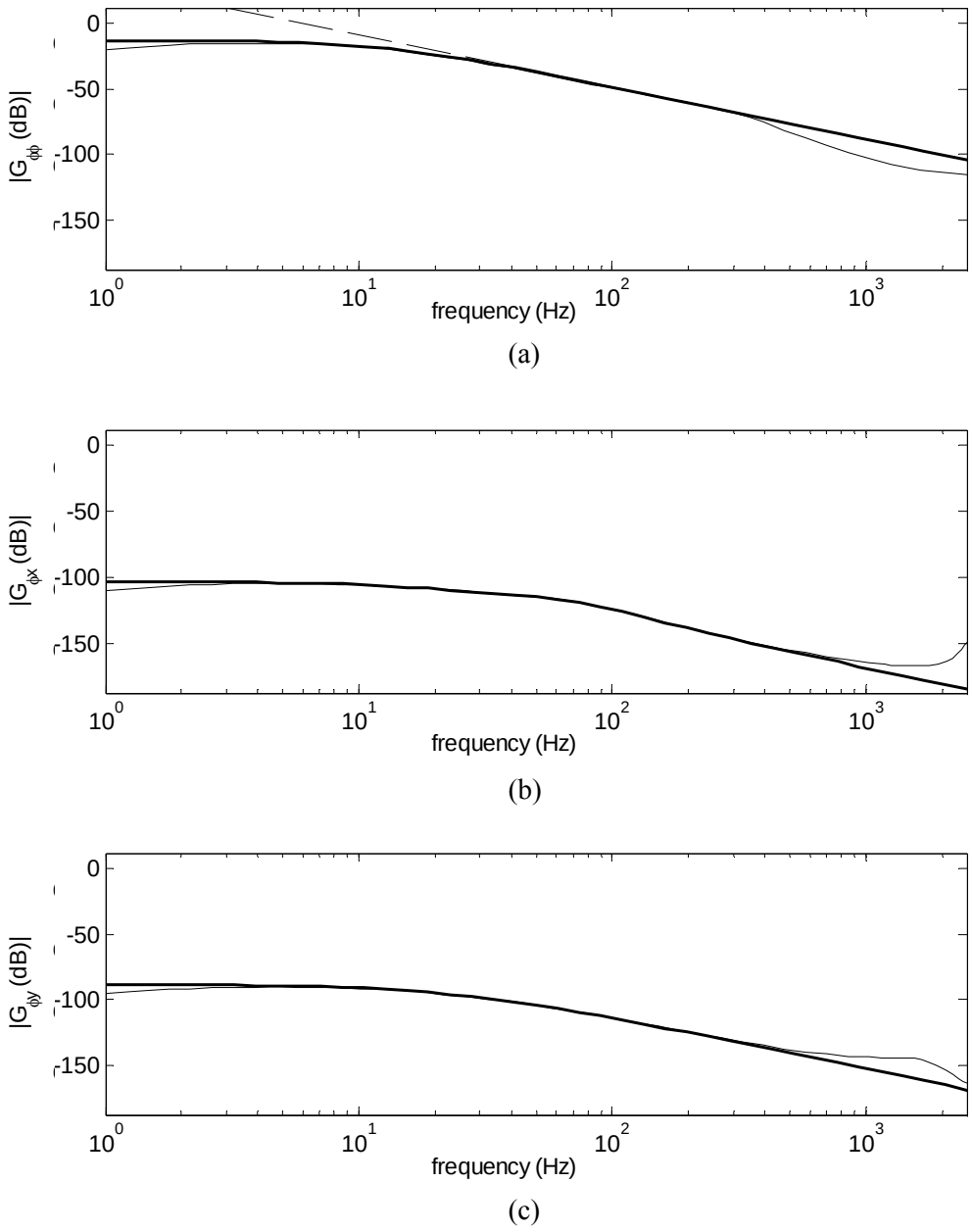

Fig. 5.9. Analytical plant TFs (dashed line), identified plant TFs (thin solid line) and reduced-order fit (thick solid line) from (a) ϕ to ϕ, (b) ϕ to x, and (c) ϕ to y

In order to test the effect of the identified model on the controller design, I conducted experiments with analytical and identified TF models in x. Fig. 5.10 shows the step responses

taken from maglev positioner with optimal LQ controller designed using the analytical plant TF model (3.3), the identified model (5.10a) and the simulated response for a step of 100 μm, normalized to 1. It is apparent from the figure that the identified model gives a closer match with the simulated results and hence is more reliable. The small mismatch between the simulated response and the response using identified TF model might be because of order reduction and coupling with other axes, as in this experiment, the coupling TF as well as identified TFs in other axes were ignored. Incorporating all 9 identified TFs in the controller design is expected to give a much closer match.

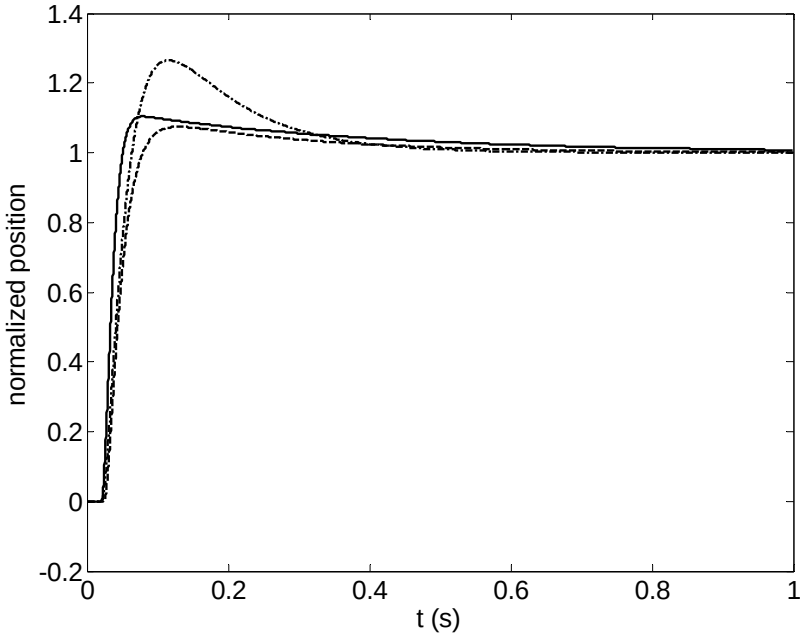

Fig. 5.10. Experimental evaluation of the identified plant TFs – step responses with identified model (solid), analytical model (dashed) and simulated response (dash-dotted)

5.4 Summary

In this chapter, system identification was performed to obtain the system models and coupling terms of the developed Y-stage. The BJ method with a closed-loop framework and a

known controller structure was used to derive the closed-loop TF from the input-output time sequences. A zero-mean WGN and a chirp signal were used in two separate experiments as persistently excited reference inputs, and the effectiveness of each was discussed in identifying the plant behavior with fidelity. Since the control structure was known perfectly, the open-loop TF and the coupling terms were determined from the closed-loop and controller TFs. The entire analysis was performed using discrete-time equations to avoid any digitization errors from continuous-time. The continuous-time analyses in terms of Bode magnitude plots and pole-zero maps were performed to check the effectiveness of the system identification and order-reduction algorithms and to interpret the physical meanings of the identified models. The closed-loop system responses with these models were found to have a significantly close match with simulated results within the control bandwidth. In the subsequent chapters, I will be using these identified models for the Y-stage instead of the analytical ones for controller design. For the Δ-stage, however, I will continue using the analytical plant model.

CHAPTER VI

NANOSCALE PATH PLANNING AND MOTION CONTROL

6.1 Introduction

This chapter addresses nanoscale path planning and motion control with the two maglev nanopositioners. Although these nanopositioners have been demonstrated to have nanoscale-positioning and load-carrying capabilities as demonstrated in Chapter III, the performance of the positioners remains to be proven for any practical applications such as μSTL, DPN, and scanning applications for imaging and manipulation of nanoscale surface phenomena. Motion trajectories commonly used in industrial applications are identified along with the challenges in optimal path planning to meet the nanoscale motion-control objectives and achieve precise positioning and maximum throughput simultaneously. Key control parameters in path planning are determined, and control design methodologies including a well-damped lead-lag controller are proposed to satisfy the positioning requirements. The proposed methodologies, individually and collectively, are implemented. Experimental results are presented in this chapter to illustrate their effectiveness in planning optimal trajectories. With these techniques, the maglev stage demonstrated excellent performances for the chosen nanomanufacturing applications in terms of position resolution, accuracy, and speed, and with tracking errors as small as 4.5 nm.

Note that the physical properties and behavior of the material under manufacturing change at nanoscale. This scale effect exists in a device which is actually scaled down to a micro/nano-level size, for instance, an electrostatic microelectromechanical-system (MEMS) motor. In the maglev system, however, there was no such physical scaling of the actual

positioning device. The size of the moving platen is on the order of a few hundred millimeters. Due to the benefits of the maglev technology we are able to achieve nanoscale precision in path planning and motion control. Thus, by considering the facts that (a) the forces acting on the positioner are too small (on the order of a few millinewtons) to produce any significant distortion in the structure of the platen, and (b) the laser-interferometer sensor provides averaged measured data over the beam diameter and due to multiple passes on the reflecting surfaces, it may be concluded that the platen structure is rigid for all practical purposes. This means that each point on the entire platen actually moves by the exact same amount when the sensor senses the movement of a particular point on the platen.

6.2 Nanoscale Path Planning Techniques

Fig. 6.1 shows a motion trajectory followed by the platen that can be employed in a μSTL application with the controllers given by (3.12). As shown in the figure, the actual path significantly overshot the commanded trajectory. This is because the controller was not optimized for speed, and the platen did not begin the corner turns until the actual path overshot the command. Furthermore, since the controllers were simple lead-lag compensators, there was no direct control over the velocity. Coupling between the x- and y-axes was also significant as seen in Fig. 6.1(b) since the controllers were decoupled SISO ones. In the following subsections, several attempts are made to reduce these shortcomings for better trajectory-tracking.

6.2.1 Overshoot Reduction

There are various ways through which the overshoot may be reduced.

A. Using Smaller Yet Uniform Position-Command Steps

Since the plant model is assumed to be linear, the overshoot is linearly proportional to the step size. Hence the overall overshoot can be significantly reduced by using successive smaller position-command steps instead of a single large one. Fig. 6.2(a) shows the path (solid line) followed by the stage using smaller uniform steps of 5 μm against the larger 20-μm and 25-μm steps shown in Fig. 6.1(a) to cover the same distance. The error in *x* is shown in Fig. 6.2(b) with solid line. The overall percentage overshoot was reduced from 39.35% to 6.58% in *x* and from 31.99% to 5.05% in *y*. The percentage overshoot was calculated by dividing the maximum amount the platen overshoots its final value divided by its final value expressed as a percentage. As shown in the error plot, the position noise is maintained within 12 nm pp (peak-to-peak) except at the corners.

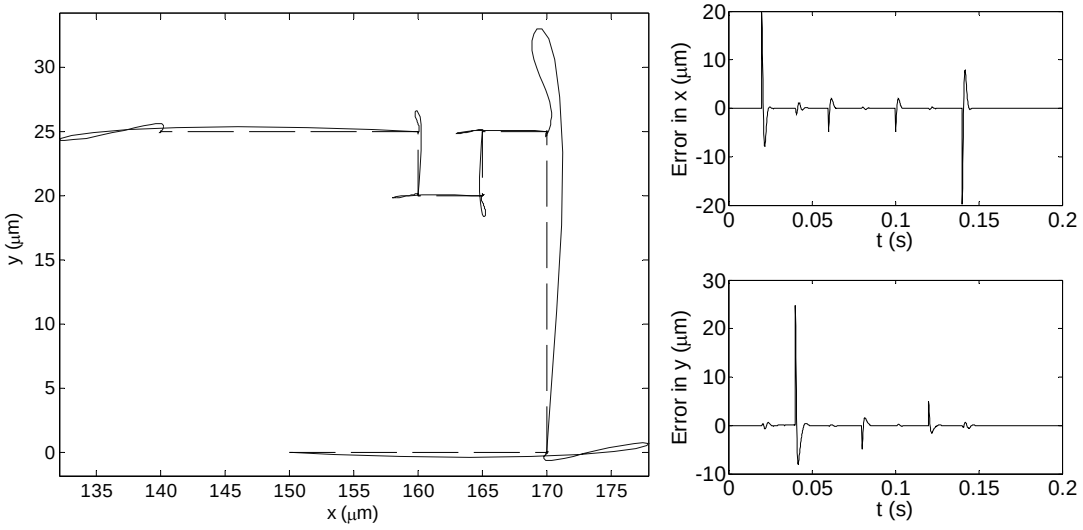

(a) (b)

Fig. 6.1. (a) Commanded trajectory (dashed line) and path traversed by the platen without using path-planning methodologies (solid line). (b) Errors in *x* and *y*.

B. Using Decreasing Position-Command Steps

An alternate method is to use decreasing step-command sizes. It, in effect, slows down the platen as it approaches the corners. Fig. 6.2(a) (dashed line) shows the path followed by the stage using the step-sizes decreasing in a geometric progression (12.5000, 6.2500, 3.1250, 1.5625, and 1.5625 μm). The error in *x* is shown in Fig. 6.2(b) with a dashed line. The overall percentage overshoot was reduced prominently to 2.32% from 39.35% in *x* and 2.12% from 31.99% in *y*.

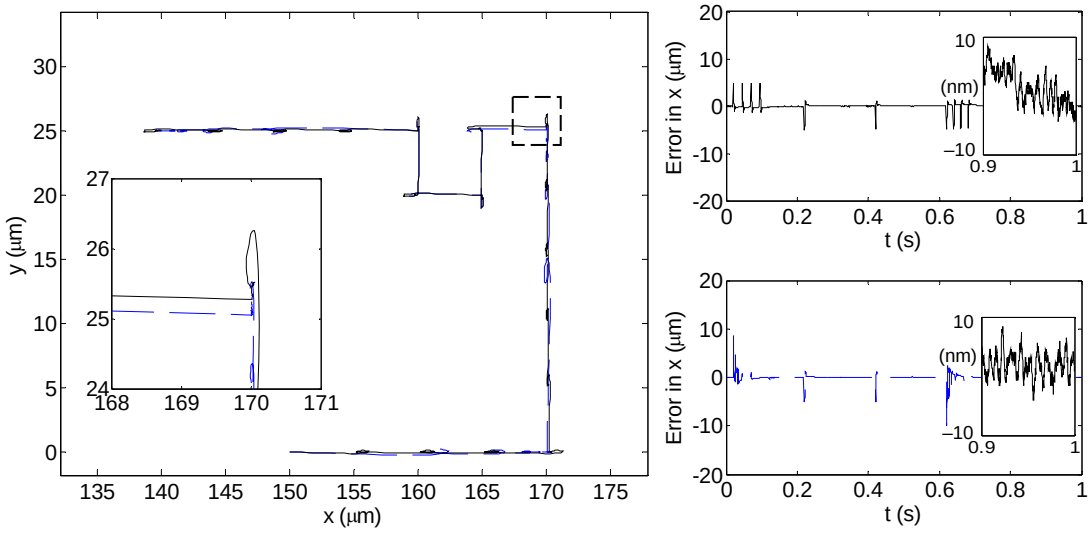

Fig. 6.2. (a) Path traversed by the platen using path-planning methodologies with smaller uniform steps of 5 μm (solid), and with decreasing step commands (dashed). (b) Errors in the corresponding trajectories.

The performance of the maglev positioner is almost identical in *x* and *y* and hence, the *y*-axis error results are omitted. In this error plot, the main source of error in the trajectory tracking is the sudden change in the commanded path around the corners which is our main concern. In the steady state, the position resolution for the trajectory using path planning methodologies

remains better than 12 nm pp. For the above two trajectory-planning experiments, I used a controller with a 48-Hz cross-over frequency and 51° PM given by (3.12).

C. Using a Damped Controller

Although the above two methods are capable of providing significant improvements in the dynamic performance of the maglev platen, they depend on the nature of the trajectory, and hence give little flexibility. Furthermore, applications like scanning demands a much better transient response and any overshoot is unacceptable. A better way to tackle this problem is to design a controller capable of giving a damped response to a step command and hence little or no overshoot. I designed another controller with this objective with a larger cross-over frequency of 85.8 Hz and 73° PM which meets the conflicting requirements of lesser overshoot and faster dynamic responses simultaneously. The TF for the resulting compensator is given by

$$G(s) = \frac{K(s+73.51)(s+8.53)}{(s+2.30)(s+4014)} \tag{6.1}$$

The controller gain $K = 4.5997 \times 10^5$ N/m. The step responses in x with this controller and the one being used in the previous two methods (with a crossover frequency of 48 Hz and 51° PM) have been compared in the Fig. 6.3. The percentage overshoot was reduced from 39.35% to 11.85%. Additionally, due to the larger crossover frequency, the rise time decreased from 4.5 to 2.2 ms using a 10% criterion.

6.2.2 Velocity Control

Another parameter to be controlled in trajectory-tracking is the velocity. The platen needs to be slowed down as it approaches the corners (as shown in Fig. 6.1(a)) for sharper

maneuvers. One way to control the velocity is, again, through controlling the command step size. The implementation of the controller in the form of difference equations requires steps at fixed time intervals (0.2 ms for our case at the sampling rate of 5 kHz). Varying the step size for the fixed time intervals is thus equivalent to varying the speed of the platen. Note that in using the smaller steps as in the previous section, the motion was more like a staircase. For velocity control, the motion is essentially a ramp, which is what we need. In discrete-time control, the two motions may be related by the fact that as the step size gets smaller and smaller, the staircase motion imitates a ramp.

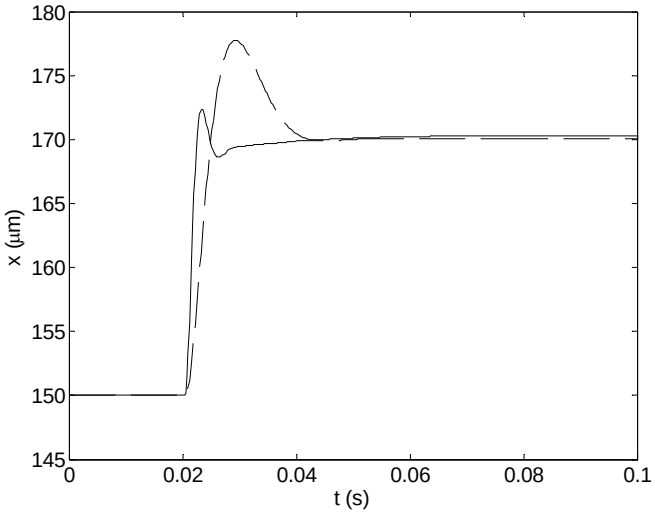

Fig. 6.3. Step responses in the *x*-axis with the 85.8-Hz (solid) and 48-Hz (dashed) controllers

Fig. 6.4(a) shows the effect of varying the platen speed on the accuracy in trajectory tracking. It shows the same trajectory followed by the platen as shown in Fig. 6.1(a) but with the spatial scale reduction by a factor of 100. As the platen speed was reduced from 50 μm/s to 5 μm/s, the position accuracy of the platen was dramatically improved. Fig. 6.4(b) shows the error in *x* and *y*. The position-noise level varied from the best of 4.5 nm to the worst of 10.5 nm pp. The maximum deviation from the trajectory was 8.5 nm.

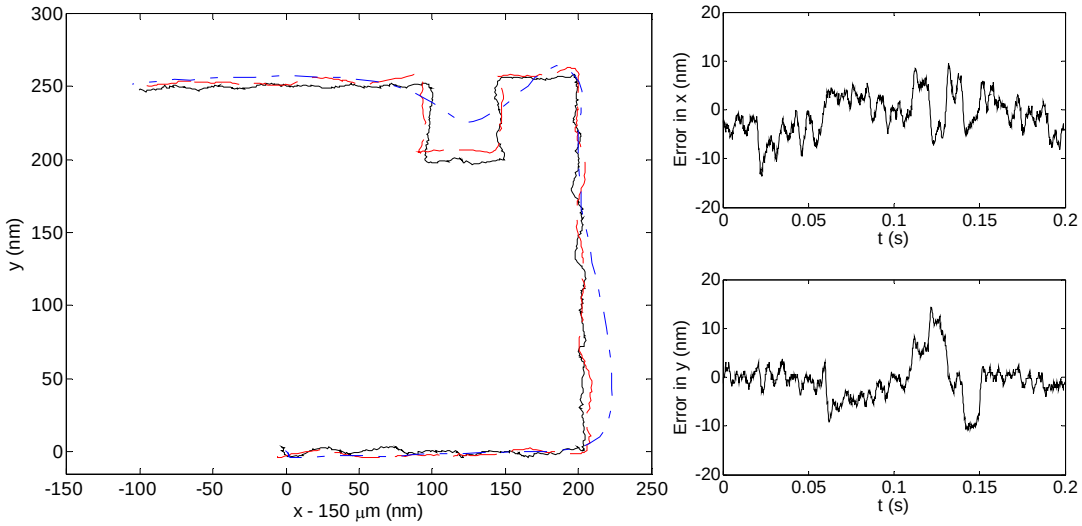

(a) (b)

Fig. 6.4. (a) Paths traversed by the platen at nanoscale at 50 μm/s (dash-dotted line), 25 μm/s (dashed line), and 5 μm/s (solid line). (b) Error in *x* in the path traversed at 5 μm/s (solid line in Fig. 6.4(a)).

6.2.3 Trajectory Tracking

The above two methodologies combined together can drastically improve trajectory-tracking. In this section the effectiveness of the presented nanoscale path planning methods is demonstrated on three spatial scales differing by a factor of 100.

Fig. 6.5 shows the nanoscale trajectory tracking with the Δ-stage and the Y-stage. The path was traversed at a constant velocity of 5 μm/s in both the cases. Error plots of the profile traced by Δ-stage shows that the position-noise level varied from the best of 4.5 nm pp to the worst of 10.5 nm pp. The percentage overshoot was 2.50% and coupling among the *x*-*y* axes was 1.85%. The coupling was calculated by dividing maximum deviation in an axis by the length traversed by the platen in the other axis expressed as percentage. Likewise, for the Y-stage, the position-noise level varied from the best of 8.4 nm pp to the worst of 15.6 nm pp. The

percentage overshoot was 3.85% and coupling among the *x*-*y* axes was 1.32%. These values are summarized in Table 6.1.

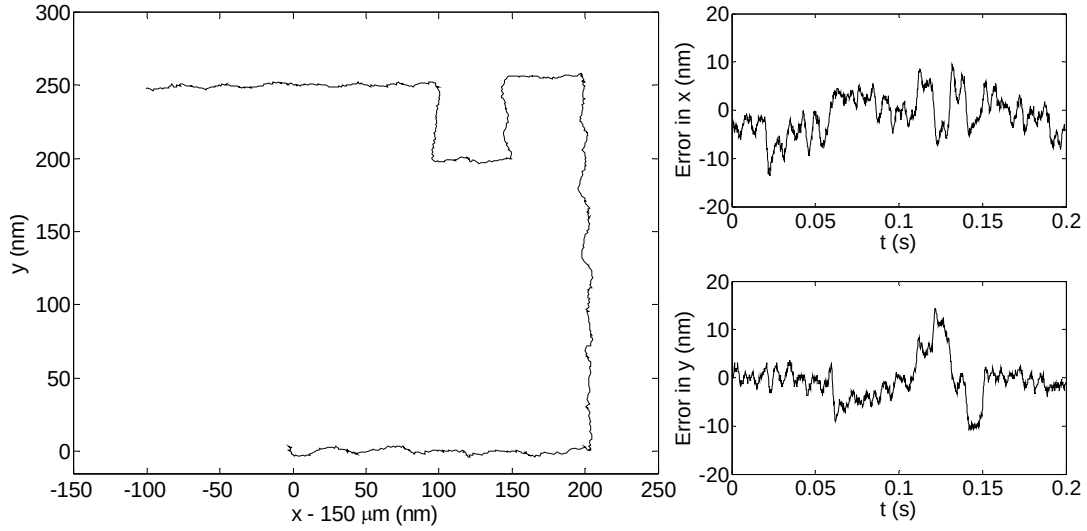

(a)

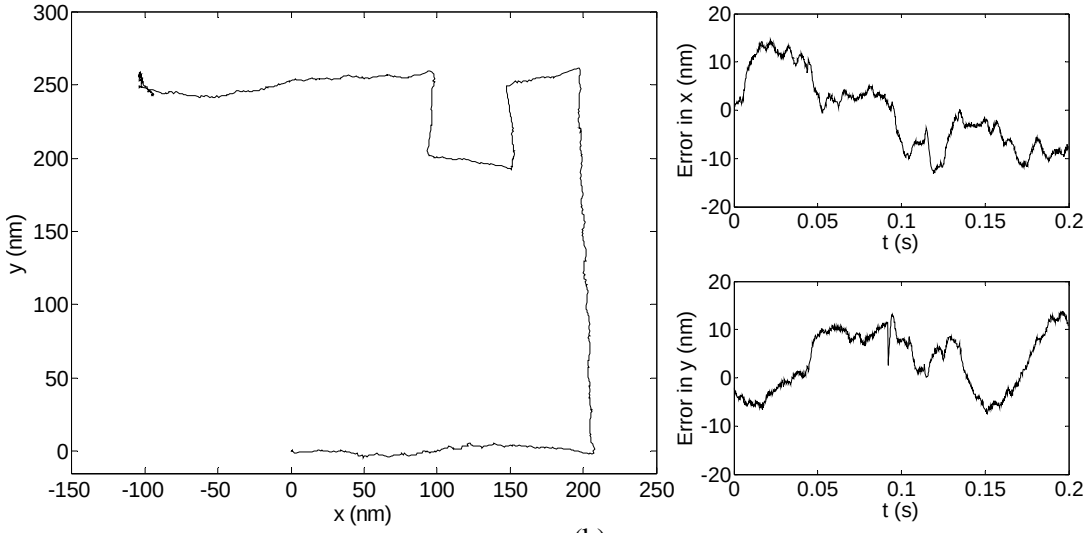

(b)

Fig. 6.5. Nanoscale trajectory tracking using the combined path-planning methodology and errors in *x* and *y* with (a) the Δ-stage and (b) the Y-stage

Table 6.1. Performance of the two maglev stages with nanoscale path planning and motion control

Parameter	Nanoscale		Microscale		Milliscale	
	Δ-stage	Y-stage	Δ-stage	Y-stage	Δ-stage	Y-stage
Velocity (μm/s)	5	5	50	50	–	500
Overshoot (%)	2.50	3.85	0.37	0.54	–	0.06
Coupling (%)	1.85	1.32	0.02	0.04	–	0.81
Noise (nm)	10.5	15.6	18.2	19.3	–	20.8

A direct comparison of the trajectory originally presented in Fig. 6.1 without using and with using path planning methods is given in Fig. 6.6. It shows the microscale trajectory tracking with the two maglev nanopositioners. The path was traversed at a constant velocity of 50 μm/s in both the cases. A comparison between this trajectory and the one shown in Fig. 6.1(a) shows that the percentage overshoot was reduced from 39.35% to 0.45% in *x* and 31.99% to 0.37% in *y*. The maximum steady-state error was reduced from 20.6 nm to 18.2 nm. Coupling among the axes was reduced from 4.74% to 0.05% in *x* and 1.80% to 0.02% in *y*. However, the total time taken to trace the entire trajectory increased from 0.17 s to 1.7 s. This time increase is, however, acceptable for an application like μSTL that works at a much slower rate [47]. The values are summarized in Table 6.1. A comparison showing the improvement in the dynamic performance of the maglev nanopositioner is given in Table 6.2.

Table 6.2. A comparison between the microscale performance of the Δ-stage without and with using nanoscale path planning methods

Parameter	Without	With
Overshoot (%), *x*	39.35	0.45
Overshoot (%), *y*	31.99	0.37
Coupling (%), *x*	4.74	0.05
Coupling (%), *y*	1.80	0.02
Noise (nm)	20.6	18.2
Time (s)	0.17	1.70

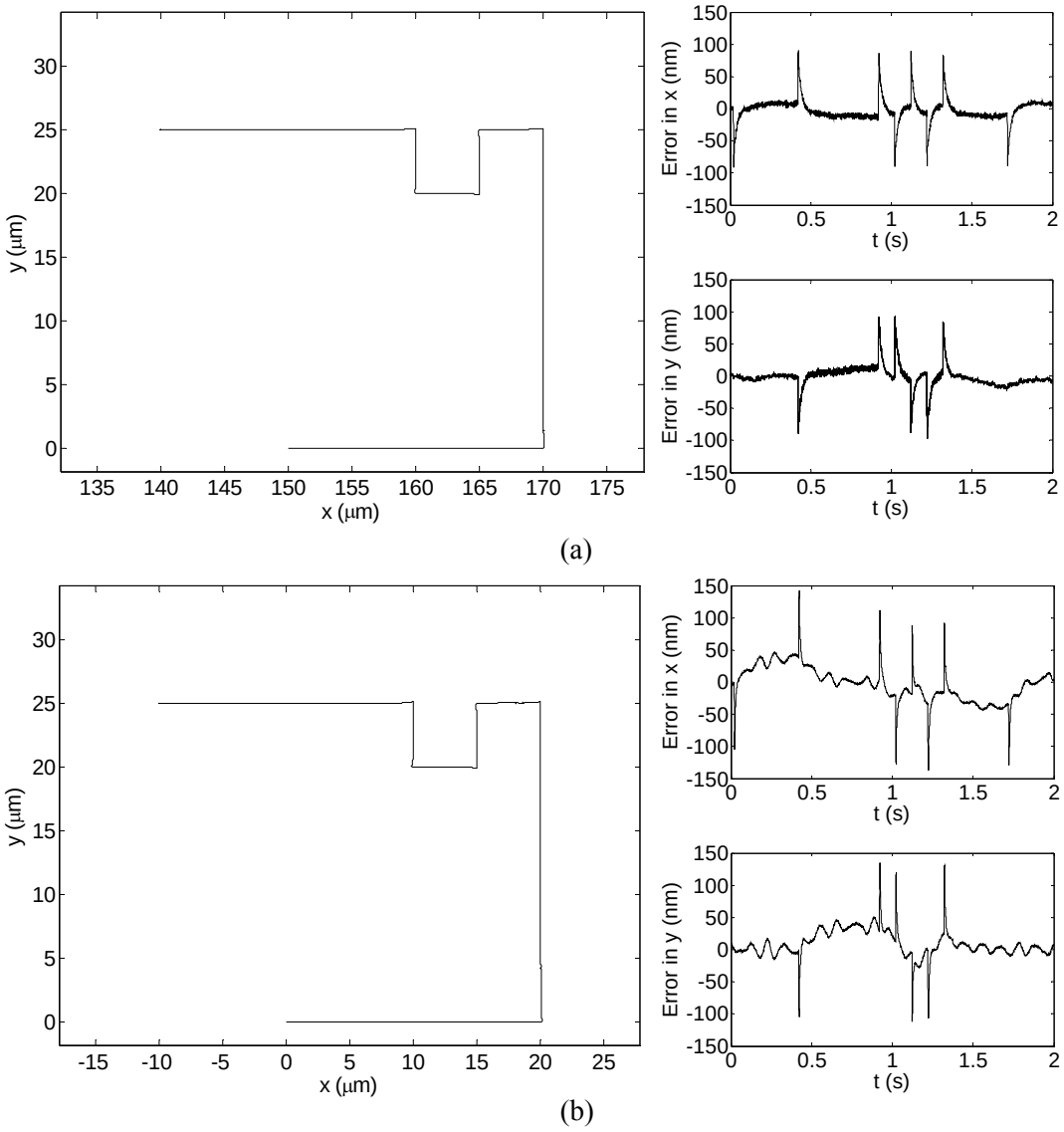

Fig. 6.6. Microscale trajectory tracking using the combined path-planning methodology and errors in x and y with (a) the Δ-stage and (b) the Y-stage

Finally, the results of nanoscale path planning and motion control are extended to milliscale. Since the Δ-stage does not have the large travel capabilities, this result is shown only for the Y-stage. Fig. 6.7 shows the trajectory traced by the Y-stage using path planning methods. The path was traversed at a constant velocity of 500 μm/s. The most noticeable part of this

profile is that in spite of the a spatial order difference of 10000× compared to the nanoscale trajectory shown in Fig. 6.5, the position error is maintained at around 20 nm pp except at the corner maneuvers. Furthermore, the percentage overshoot was 0.06% which is comparable to the corresponding microscale and nanoscale values. This confirms that the performance of the maglev nanopositioner is linear as it was assumed in plant modeling.

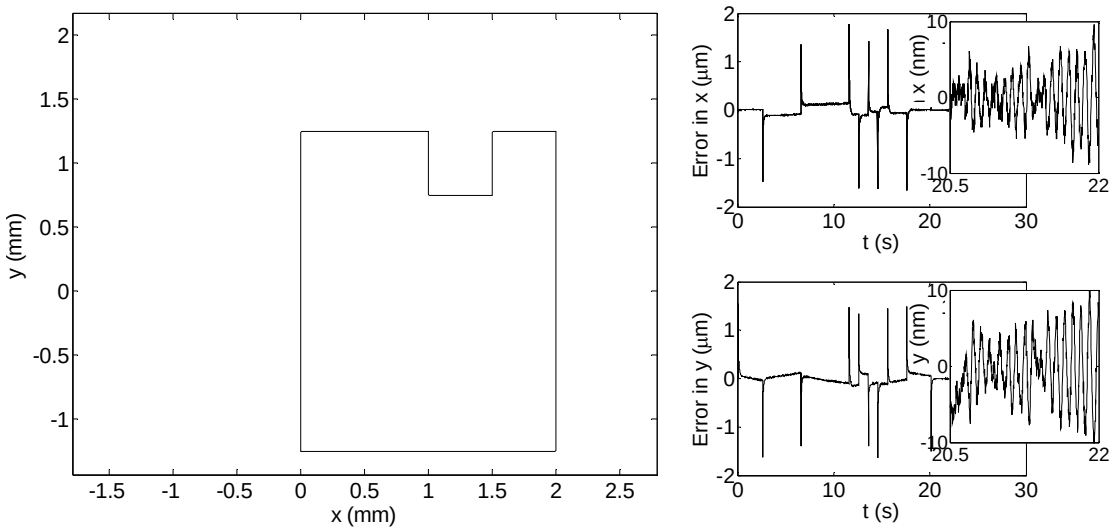

Fig. 6.7. Milliscale trajectory tracking using the combined path-planning methodology and errors in *x* and *y* with the Y-stage

The findings from the trajectory tracking can be summarized as follows.

1. From Fig. 6.5, the performance of the Δ-stage was found to be better compared to the Y-stage. The difference in the performances arises because of their different regulation performances as shown earlier in the Fig. 3.6. In particular, there was a low-frequency disturbance present in the Y-stage response, which can be seen from Fig. 6.7. A detailed analysis of this disturbance component is given in the following subsection.
2. The maximum tracking error occurs in all the trajectories presented above (Figs. 6.5–6.7) while cornering a profile. A pre-specified upper bound can be put on these maximum

tracking errors depending on the application at hand. This can be done by controlling the step-sizes and/or velocity as the platen approaches the corners. The effectiveness of both these techniques was shown in the Sections 6.2.1 and 6.2.2. For continuously varying trajectories such as circles, this problem is insignificant.

3. The profile in Fig. 6.7 was tracked with maximum velocity among the three profiles presented above at various spatial scales. As the velocity is increased, the results using nanoscale path planning techniques gets closer to the ones following a direct single step. Consequently, it took the Y-stage longer to settle to the steady-state values. Here, I reiterate that there is a trade-off between the position accuracy and the process throughput; high position accuracy can be achieved for large travel if the travel speed is kept very slow. Accordingly, the steady-state error can again be controlled by limiting the tracking speed. The problem of handling conflicting performance specifications will be tackled in Chapter VII.

From the conclusions derived above, it is recommended that the Δ-stage is more suitable for nanoscale applications with small (several hundred micrometers) travel range, where there are stringent requirements on the position resolution. The Y-stage, on the other hand, is more appropriate for large range (several millimeters) motion applications with resolutions requirements on the order of at most few tens of nanometers.

6.2.4 Noise Analysis

It may be noted from Fig. 6.7 that there is a distinct frequency component of disturbance present in the tracking response of the Y-stage. By counting the number of peaks per second, this frequency is expected around 14 Hz. I performed power spectral density (PSD) analysis of the

regulation with the Y-stage with a sampling frequency of 40 Hz in order to identify exact frequency of this disturbance and to locate its source. Fig. 6.8 shows the results of this analysis.

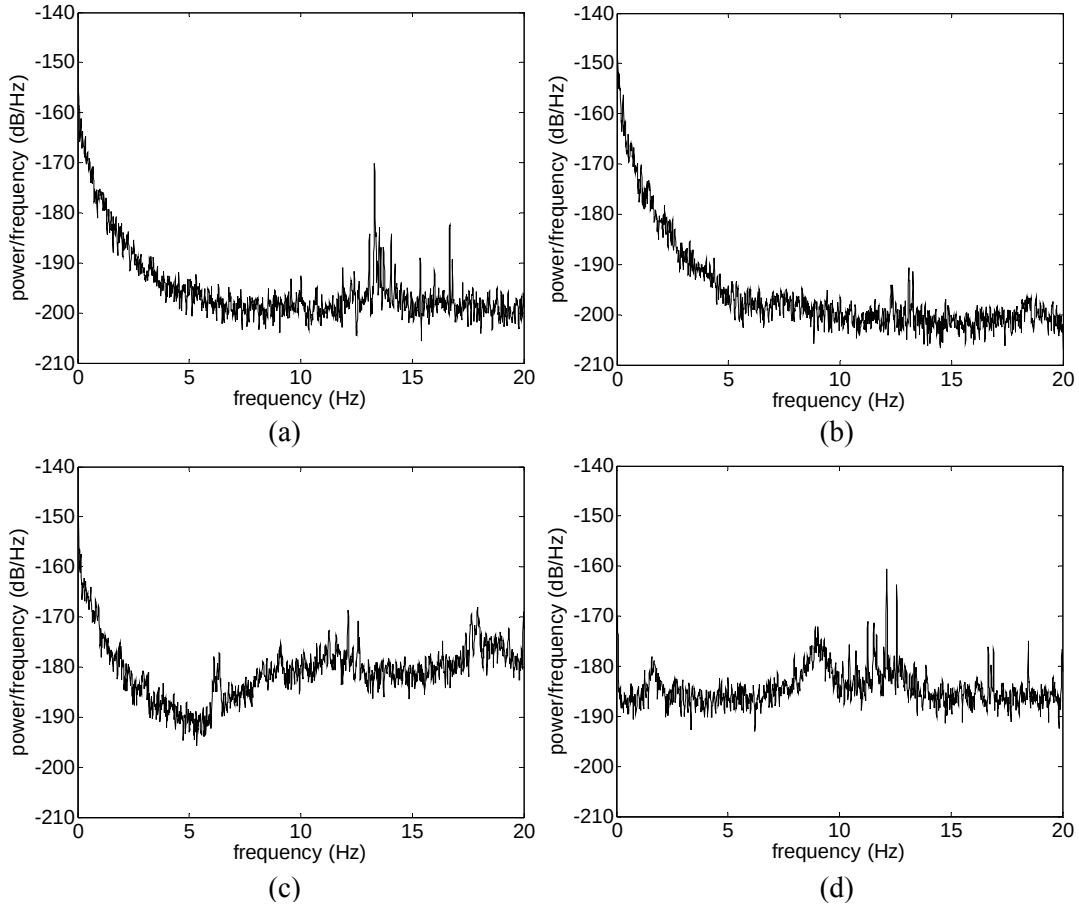

Fig. 6.8. Results of the PSD analysis of disturbance coming in the closed-loop response of the Y-stage (a) without using optical table, (b) using optical table, (c) replacing the laser interferometer, and (d) with the platen in 6-axis magnetic levitation

Fig. 6.8(a) shows the PSD of the data from one of the laser interferometer receivers without using the optical table for passive vibration isolation. The platen was not levitated in this experiment. Therefore, this plot shows the disturbances being transmitted primarily from the floor. A peak at around 14 Hz confirms the prediction made from Fig. 6.7. With the use of optical table, I was able to attenuate this frequency by about 20 dB. This has been shown in the Fig. 6.8(b).

Another possible source of this disturbance might be the mechanical vibrations in the interferometer itself. To test this, I replaced one of the interferometer. Fig. 6.8(c) shows the PSD of the data taken with this new interferometer. All other conditions were identically the same as those of Fig. 6.8(b). The amplitude and frequency content of the two plots are significantly different. This implies that if there are loose parts in the interferometer system or if the components of the sensor system, including the mirrors, interferometer and receiver, are not fixed firmly, the sensor itself can be major source of erratic readings. This error is in addition to the sensor noise originated due to its electronics. Particularly, since we are working with a nanopositioning device and its accuracy depends on the accuracy of sensed data, even small vibrations in the sensor system may be significantly detrimental to the fidelity of the reading.

Finally, I checked the response of the maglev stage using closed-loop control. The PSD analysis of this data is presented in the Fig. 6.8(d). The platen was in 6-axis magnetic levitation for this experiment with all other conditions being the same as those of Fig. 6.8(b). This figure shows that while the controller dynamics attenuates the frequencies under 4 Hz, it actually amplifies the frequencies higher than that by about 15 dB. In particular, the 14-Hz frequency component reappears. Since this disturbance is within the control bandwidth, it will be challenging to get rid of it via standard loop-shaping techniques. This problem may be solved using a feedforward control method such as the one suggested by Yasuda *et al*. [26].

From the above discussions, it may be concluded that the 14-Hz disturbance appearing in the regulation and tracking responses of the Y-stage is because of the following.

1. Attenuated floor vibrations being transmitted through the optical table
2. Mechanical vibrations from the loose laser interferometer system components
3. Amplification of the disturbances by the controller dynamics

6.3 Test Results for Key Nanomanufacturing Applications

In this section, I apply the proposed methodologies to generate motion trajectories relevant to key nanomanufacturing applications such as DPN, μSTL, and scanning, and demonstrate the effectiveness of the path-planning techniques.

6.3.1 Dip-Pen Nanolithography

One of the practical applications that require extensive nanoscale path planning is DPN. DPN has emerged as an ideal solution for the direct-write nanofabrication, which plays an important role in areas such as sensor patterning, miniaturization of biological assays, and creation of nanoelectronic components. Nanoink uses NSCRIPTOR™, a dedicated scanning probe lithography system, for DPN process. Its scanning stage is motor-driven, and hence requires intensive maintenance and suffers losses due to friction from its contact-type mechanisms [60]. The apparatus uses seven motors for translation and zoom against the single-moving-part approach of the maglev stage we designed. Furthermore, their scanning is performed by three independent piezos which have several disadvantages over the maglev positioners as I discussed in Chapter I. For instance, the total travel range is limited by 90 μm in x and y and 8 μm in z. The placement precision is around 10 nm, which is comparable to the maglev nanopositioner. Thus, the maglev system has a much simpler mechanism and provides competitive advantages in terms of travel range, precision, and repeatability in DPN and other similar applications. Additionally, the maglev positioner can be used as a cluster tool in such applications, thereby eliminating the need for separate actuators for the positioning stage and cantilever probes. The probes can remain fixed throughout the entire patterning operation, while all the motion generations, as described below, can be performed using the maglev positioner.

The DPN process employs microfluidic ink delivery devices, called DPN inkwells, for coating. The use of these microwells allows dipping the probe in the ink in a controlled fashion and prevents the ink from coating the top side of the probe cantilever, and a number of different inks can be simultaneously introduced on adjacent cantilevers in a probe array. A typical nanopatterning process consists of the following steps. (1) The cantilever probe needs to be aligned with the microwells. The probe may be a single one or a probe array. (2) The probe is dipped in a microwell for coating. When lowering the probes onto the microwells, the probes contact the ink and their cantilevers bend. Here again, the lowering must be precisely controlled in order to avoid damage to the cantilevers. (3) After a successful dipping step, inking is complete. The probes are now translated onto the DPN substrate, where ink deposition can commence. Feature size is a primary concern for any patterning technology and can be controlled by the amount of ink and the environmental conditions for ink transfer to the substrate. The amount of ink in turn can be controlled by regulating the probe speed. As small as 80 nm line-width may be achieved with a write speed of 20 μm/s [80].

Apparently, all these steps require extensive path planning and motion control strategies. Additionally, for high-volume work where re-inking is necessary during the patterning process, the probes need to be switched repeatedly between the microwells and the substrate with the same level of position accuracy. The Y-stage offers a solution to these requirements of DPN because if its nanopositioning capabilities and versatility. A schematic of its use for DPN is shown in the Fig. 6.9. In this setup, the cantilever probe for nanopatterning can remain fixed while the platen performs all the operations mentioned above. Typical dimensions of a nanowell die and substrate are also indicated in the figure [81]. The distance from the edge of the nanowell die to the microwell is about 2 mm. Thus a 5-mm planar travel range of the Y-stage allows writing on a 3 mm × 5 mm substrate placed closely with the inkwell die.

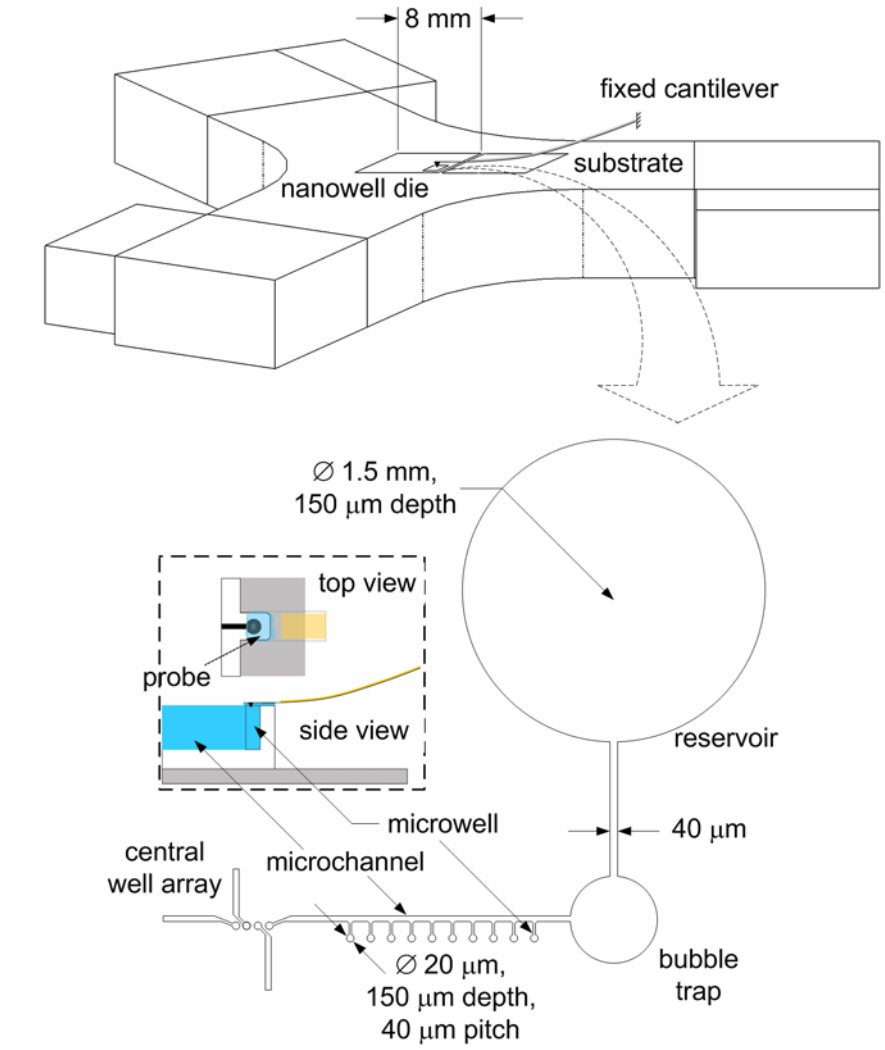

Fig. 6.9. Schematic showing the arrangement of Y-stage for DPN (Source: [81])

Fig. 6.10(a) shows the plot of experimental data of a trajectory traversed by the maglev platen for nanoscale patterning. The entire trajectory was traversed at variable speeds, 20 μm/s for the write speed channels, 100 μm/s for probe insertion, and 500 μm/s for probe release. The total time taken to complete this trajectory was 0.8 s. The height variation of the maglev positioner for patterning and rapid motions is shown in Fig. 6.10(b). Thus all the three axis motions can be achieved using the single-part platen and the cantilever probe can remain fixed

throughout the nanolithographic process. This eliminates the need of a separate bias control for cantilever probes.

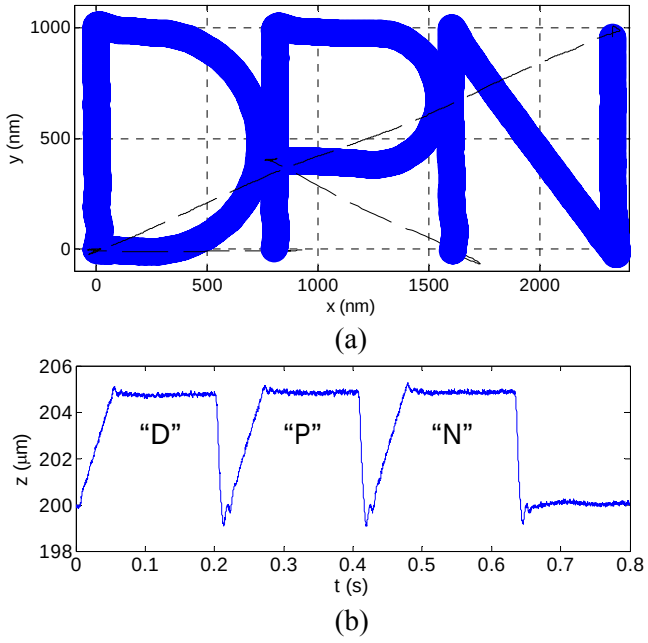

Fig. 6.10. (a) A "DPN" profile traced by the maglev nanopositioner at a write speed of 20 μm/s. The marker size for the plot is chosen so that the letters appear to be 80 nm wide in proportion to the size of the "DPN" pattern. Dashed lines represent the rapid motion of the stage while the probe is not in contact. (b) The *z*-axis motion of the maglev platen with the nominal vertical position at 200 μm when the probe is not in contact with the substrate. The height of 205 μm corresponds to the platen's vertical position during the patterning processes of each letter, D, P, and N.

6.3.2 Microstereolithography

With its inception in the early 1990's, remarkable research progresses have been made in MEMS. Many MEMS device concepts were proposed and their feasibilities were demonstrated for applications in various fields of microfluids, aerospace, biomedical, chemical analysis, wireless communications, data storage, display, optics, etc. [48]. Manufacturing processes, such as μSTL, micromachining, micromolding, and soft-lithography played a crucial role in the

miniaturization of MEMS devices. Classical STL processes use a laser beam deflected by a pair of low-inertia-galvanometric mirrors and focused by a dynamic lens to solidify photopolymer [47]. This methodology works well for objects on the order of a few hundred micrometers. However, beam defocusing becomes problematic for smaller objects. This limits the minimum achievable component size. An alternate approach is to keep the laser beam fixed and use a high-precision positioning stage to generate *x*-*y* motions for scanning [48]. Magnetic levitation became an enabling technology for these applications with position resolution as good as 5 nm [65].

Fig. 6.11 shows a microscale screw for medical tissues traced by the maglev stage with the lateral resolution of 12 nm and vertical resolution of 100 nm. The inner radius, the pitch, and the length of the threads are 12 μm, 3 μm, and 18 μm, respectively. The state of the art is the one fabricated by the Central Microstructure Facility with a lateral and vertical resolution of 10 μm, inner diameter of 600 μm, thread length of 900 μm, and pitch of 150 μm, approximately [82]. Thus the maglev positioner is capable of tracing the profile with a position resolution 2000 times better and the feature size 50 times smaller compared to the prevailing technology. Therefore in such applications, the limitation on the minimum achievable size is posed by the manufacturing technology, not the maglev positioning technology.

6.3.3 Scanning Applications

Among commonly used scanning devices are (1) piezoelectric-actuated scanners to position a probe on a sample surface during imaging of nanoscale surface phenomena with SPMs and (2) MEMS-based scanners to position optical micro-mirrors in wearable computers [32]. An alternative is to keep the probe fixed and move the stage in the *x*-*y* plane to scan the surface.

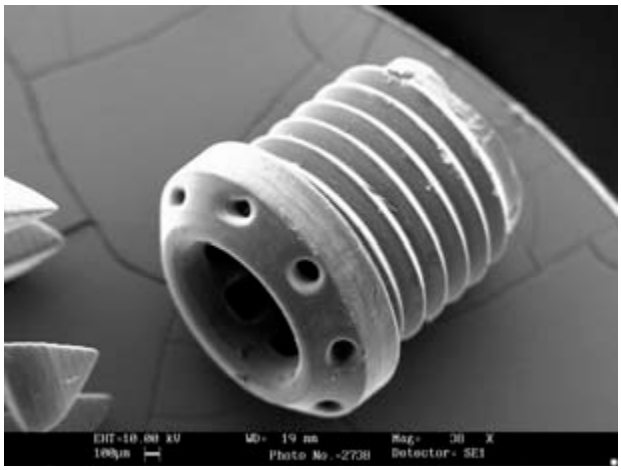

(a)

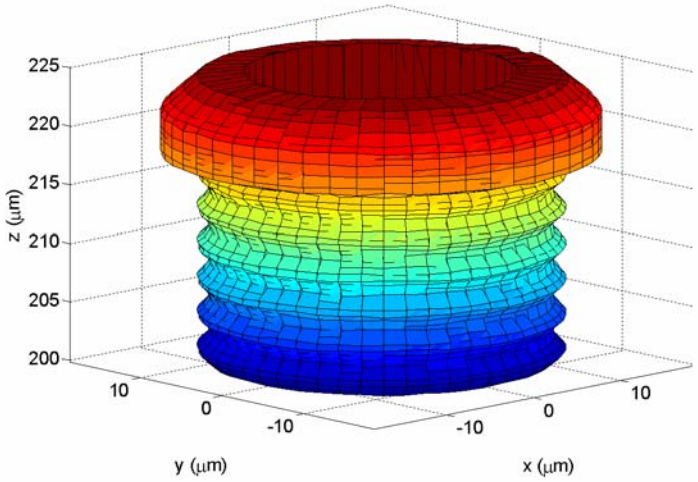

(b)

Fig. 6.11. (a) Image of a screw for medical applications manufactured by Central Microstructure Facility [82]. (b) 3D profile traced by the Δ-stage to manufacture a microscale screw for medical tissues with μSTL

A typical scanning operation consists of two sections: (1) the active-scan or output-tracking section where a desired output trajectory is pre-specified and must be tracked precisely and (2) the retrace or output-transition section where trajectory-tracking is not critical. Instead, the output is to be returned to a predefined value so that the active scan can be repeated [32].

These active-scan and retrace sections are repeated in time in a scanning operation. Fig. 6.12 shows a simple scanning trajectory traced by the maglev platen and the errors in *x* and *y* for the active scan component to demonstrate its precision scanning capability in the active-scan section as well as fast return motion in the retrace section. Paths 1-2, 3-4, and 5-6 are active-scan trajectories, and paths 2-3, 4-5, and 6-1 are fast retrace trajectories. The error in the active-scan section is well within 40 nm pp in *x* and 60 nm pp in *y*. The tracking speed and the return speed are 50 μm/s and 500 μm/s, respectively.

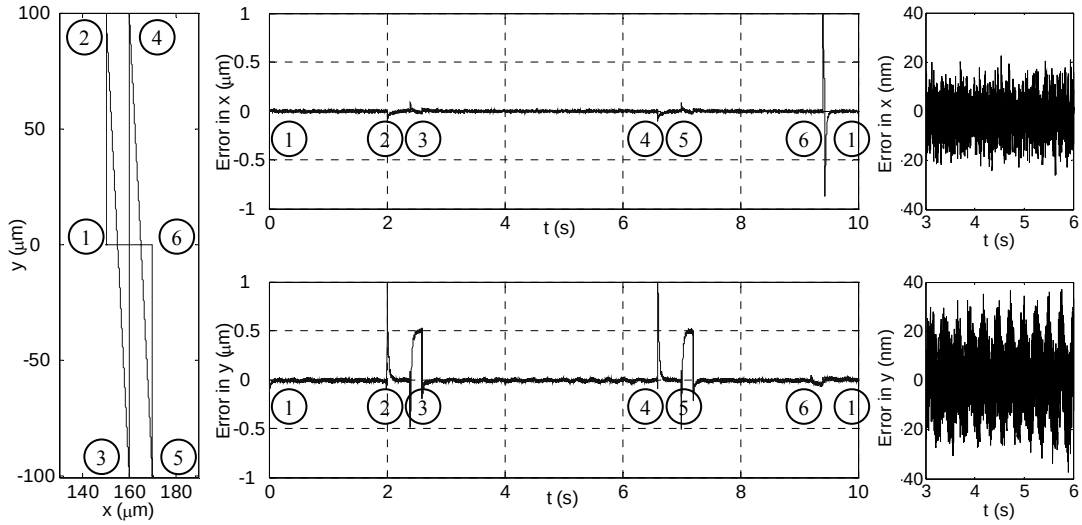

Fig. 6.12. (a) Active-scan and retrace sections scanned by the platen. (b) Error in *x* and in *y*. (c) Errors in the part 3-4 of the trajectory

6.4 Summary

With the recent development in nanomanipulation and nanomanufacturing, appropriate path-planning techniques are required as much as precision positioning itself. Although substantial research results are available on macroscopic trajectory planning and control, particularly in robotic applications, not much work has been reported yet in nanoscale path

planning and motion control. In this chapter, key problems were investigated that we might face while actually putting in use nanomanipulation devices, more specifically, incorporating a maglev stage in manufacturing or scanning applications at nanoscale.

The parameters that influence the dynamic behavior of the positioning device were identified, and ways to control these parameters were proposed. Design and implementation of a well-damped SISO lead-lag controller was described, and their influence on the performance of the maglev stage was discussed. Test results for key nanomanufacturing applications such as μSTL, DPN, and scanning were presented. The command-tracking errors were well within 20 nm with the best performance of 4.5 nm pp. The minimum achievable feature size is thus limited only by manufacturing techniques and not by our maglev positioning technology. The experimental results demonstrated that the maglev stage performed well for these nanomanufacturing applications in terms of position resolution, accuracy, speed, and versatility.

CHAPTER VII

MULTISCALE CONTROL

7.1 Introduction

One of the objectives of the presented work is to design a controller capable of meeting conflicting time-domain performance specifications. Semiconductor manufacturing is one of the applications of particular interest in this context with the demanding feature sizes (on the order of a few tens of nanometers) to be produced on a wafer while still requiring high throughput (greater than 100 wafers per hour). In this chapter, I present three multiscale control techniques that can be used to achieve these desired yet conflicting time-domain performance specifications: (1) a controller-switching technique that employs two controllers designed to meet two conflicting performance objectives. These controllers are switched in the course of operation when the tracking error reaches a predetermined fraction of the commanded step size. (2) An integral-reset scheme, which resets the integral term in the control law when a new reference point is reached. This method makes full use of the integral action in the beginning, and in effect, tends to slow down the system response to reduce overshoot as the output approaches the targeted command value. (3) A reduced-order model-following approach that uses a dynamic reference model without increasing the overall order of the system. The objective of this scheme is to make the plant's output track the model's output as closely as possible. All these methods exhibit better performances compared with conventional control schemes as shown in this chapter. The term *multiscale control* is used throughout this chapter in order to emphasize the

fact that such control is capable of meeting such conflicting time-domain performance specifications and providing desired performances in both nanoscale and macroscale operations.

Optimal PI control is used as a basis for the controller design. The reason for this choice is its popularity in most industrial applications. PI controllers are often effective and are easy to implement and maintain. Additionally, the results from optimal control methods are well-known to minimize the control effort and guarantee robust stability margins, particularly if full-state feedback is available. Furthermore, the inclusion of the integral term ensures the zero steady-state error for type-0 plants or the plants whose parameters are not perfectly known.

7.2 Conventional Optimal PI Control Revisited

In this section, the conventional optimal PI control is discussed briefly. It is usually desirable to include the integral action in optimal control systems in order to eliminate the offset due to unmeasured load disturbances or modeling errors. Consider the LTI system

$$\begin{aligned} \dot{\boldsymbol{x}}_{\boldsymbol{p}} &= A_p \boldsymbol{x}_{\boldsymbol{p}} + B_p \boldsymbol{u}_{\boldsymbol{p}} \\ \boldsymbol{y}_{\boldsymbol{p}} &= C_p \boldsymbol{x}_{\boldsymbol{p}} \end{aligned}, \tag{7.1}$$

where $\boldsymbol{x}_{\boldsymbol{p}}$ is the state vector of dimension n, $\boldsymbol{u}_{\boldsymbol{p}}$ is the control vector of dimension r, $\boldsymbol{y}_{\boldsymbol{p}}$ is the output vector of dimension m, and A_p, B_p, and C_p are constant matrices of appropriate dimensions. The system is assumed to be controllable. It is also assumed that full-state feedback is available. Its unavailability will not affect rest if the following analysis. However, robust stability cannot be guaranteed in that case. For the piecewise constant, non-zero reference points, an analogous PI control law can be obtained by redefining the state and output vectors. Let $\boldsymbol{y}'_{\boldsymbol{p}}$ be the r_0-dimensional subset of $\boldsymbol{y}_{\boldsymbol{p}}$ for which integral action is desired. It is assumed that $r_0 \leq r$ since there are only a total of r DOFs [78]. Then the augmented system can be described as

$$\begin{bmatrix} \dot{\boldsymbol{e}}_{x_p} \\ \dot{\boldsymbol{\xi}}_{\boldsymbol{p}} \end{bmatrix} = \begin{bmatrix} A_p & 0 \\ C_p' & 0 \end{bmatrix} \begin{bmatrix} \boldsymbol{e}_{x_p} \\ \boldsymbol{\xi}_{\boldsymbol{p}} \end{bmatrix} + \begin{bmatrix} B_p \\ 0 \end{bmatrix} \boldsymbol{e}_{u_p}$$
$$\begin{bmatrix} \boldsymbol{e}_{y_p} \\ \boldsymbol{\xi}_{\boldsymbol{p}} \end{bmatrix} = \begin{bmatrix} C_p & 0 \\ 0 & I \end{bmatrix} \begin{bmatrix} \boldsymbol{e}_{x_p} \\ \boldsymbol{\xi}_{\boldsymbol{p}} \end{bmatrix} \quad , \tag{7.2}$$

or

$$\begin{aligned} \dot{\tilde{\boldsymbol{x}}}_p &= \tilde{A}_p \tilde{\boldsymbol{x}}_p + \tilde{B}_p \boldsymbol{e}_{u_p} \\ \tilde{\boldsymbol{y}}_p &= \tilde{C}_p \tilde{\boldsymbol{x}}_p \end{aligned} \tag{7.3}$$

with the new set of variables $\boldsymbol{e}_{x_p} = \boldsymbol{x}_p - \boldsymbol{x}_{\boldsymbol{R}}$, $\boldsymbol{e}_{y_p} = \boldsymbol{y}_p - \boldsymbol{y}_{\boldsymbol{R}}$, $\boldsymbol{e}_{u_p} = \boldsymbol{u}_p - \boldsymbol{u}_{\boldsymbol{R}}$, and $\boldsymbol{y}_p' = C_p' \boldsymbol{x}_p$, where C_p' is the appropriate partition of C_p, and the subscript R denotes the reference values of the corresponding variables. Furthermore, the set of integral state variables, $\boldsymbol{\xi}_{\boldsymbol{p}}$ is defined as

$$\boldsymbol{\xi}_{\boldsymbol{p}}(t) = \int_0^t \left(\boldsymbol{y}_{\boldsymbol{p}}'(\tau) - \boldsymbol{y}_{\boldsymbol{R}}' \right) d\tau \, . \tag{7.4}$$

Let $\tilde{J}$ denote the performance index for the augmented system:

$$\begin{aligned} \tilde{J} &= \frac{1}{2} \int_0^\infty \left(\boldsymbol{e}_{y_p}^T Q \boldsymbol{e}_{y_p} + \boldsymbol{\xi}_{\boldsymbol{p}}^T Q_I \boldsymbol{\xi}_{\boldsymbol{p}} + \boldsymbol{e}_{u_p}^T R \boldsymbol{e}_{u_p} \right) dt \\ &= \frac{1}{2} \int_0^\infty \left(\tilde{\boldsymbol{y}}_{\boldsymbol{p}}^T \tilde{Q} \tilde{\boldsymbol{y}}_{\boldsymbol{p}} + \boldsymbol{e}_{u_p}^T R \boldsymbol{e}_{u_p} \right) dt \end{aligned} \quad , \tag{7.5}$$

where $\tilde{Q} = \begin{bmatrix} Q & 0 \\ 0 & Q_I \end{bmatrix}$. If the augmented system is controllable, the optimal control law is given by

$$\boldsymbol{e}_{u_p} = -R^{-1} \tilde{B}^T \tilde{P} \tilde{\boldsymbol{x}}_{\boldsymbol{p}} = -K \tilde{\boldsymbol{x}}_{\boldsymbol{p}} \, , \tag{7.6}$$

where $\tilde{P}$ satisfies the algebraic Riccati equation. The control law in (7.6) can also be expressed as

$$\boldsymbol{u}_{\boldsymbol{p}} = \boldsymbol{u}_{\boldsymbol{R}} + K_C \left(\boldsymbol{x}_{\boldsymbol{R}} - \boldsymbol{x}_{\boldsymbol{p}} \right) + K_I \int_0^t \left(\boldsymbol{y}_{\boldsymbol{R}}' - \boldsymbol{y}_{\boldsymbol{p}}' \right) d\tau \, , \tag{7.7}$$

where K_C and K_I are partitions of K in (7.6).

Equation (7.7) gives the optimal PI control law for the general non-zero reference-tracking problem. The control gain matrices, K_C and K_I, are determined by the choice of the weight matrices, Q, Q_I, and R. These weight matrices are often treated as the tuning parameters for a given control application. Although the integral-control action is essential to eliminate the tracking error, the choice of the weight matrices in the quadratic performance index (7.5) usually involves a compromise between load-change and reference-tracking performances. In the following section, I propose a remedy for this problem based on some modifications of the conventional optimal PI control.

7.3 Multiscale Control

One viable choice to deal with the problem discussed in the previous section is to design multiple controllers in advance and switch them in the course of operation. The other two proposed techniques, namely integral reset and reduced-order model-following, are more rigorous and capable of providing a generalized solution. In many applications, it is desirable to use only one set of control parameters for reference tracking as well as to deal with load changes. On the other hand, it is also desirable to have small overshoot and fast response time without causing additional controller complexity or increasing the order of the plant model associated with the model-following approach. In the following subsections, I will focus on the development of three different multiscale control schemes and their analyses in terms of stability, transient and steady-state behaviors, and closed-loop criteria such as sensitivity function, bandwidth, and control effort. The reduced-order model-following scheme, being most effective of the three methods, will be discussed in more elaborate details compared to the other two.

7.3.1 Controller-Switching Scheme

In order to meet the conflicting performance requirements of fast response as well as little or no overshoot, I designed a set of two controllers to meet these two objectives separately. The two controllers were then put into use sequentially. The continuous-time state-space plant model for the *x*-axis motion for designing these controllers is given by

$$\begin{aligned} \dot{\boldsymbol{x}}_p &= \begin{bmatrix} -5.69 & 1 \\ 5477.53 & 0 \end{bmatrix} \boldsymbol{x}_p + \begin{bmatrix} 0 \\ 3.19 \end{bmatrix} u_p \\ \boldsymbol{y}_p &= \begin{bmatrix} 1 & 0 \\ 0 & 1 \end{bmatrix} \boldsymbol{x}_p \end{aligned}, \tag{7.8}$$

where the state vector $\boldsymbol{x_p}$ consists of the position and velocity of the maglev positioner, control input $\boldsymbol{u_p}$ is the force required in *x* and output vector $\boldsymbol{y_p}$ consists of the sensed position and velocity data from the laser interferometer. This plant model in state-space form is essentially the same as TF (5.10a) identified in Chapter V using the BJ method. Controllers may be designed in a similar manner for the plant models in other two axes, namely *y* and rotation about *z*, using the TFs (5.11a) and (5.12a), respectively. Note once again that there is one right-half-plane pole in the identified plant model, which correctly reflects the maglev system's open-loop instability due to the negative stiffness of the magnetic origin.

A block diagram of its control structure is shown in Fig. 7.1. The first controller in the set was designed for this system following the method discussed in Section 7.2. Since we are primarily interested in positioning, the integral action is used for position control only. The weight matrices used for the controller design were

$$\begin{aligned} \tilde{Q} &= \begin{bmatrix} 2\times10^6 & 0 & 0 \\ 0 & 1\times10^3 & 0 \\ 0 & 0 & Q_I \end{bmatrix}, \\ R &= 1 \end{aligned} \tag{7.9}$$

with $Q_I = 1\times10^{14}$. These weight matrices were chosen after a few iterations, starting with using acceptable values of $\boldsymbol{x_p}$ and u_p based on the sensing range of the laser interferometer and actuator saturation limits, such that $\tilde{Q}_{ii} = 1/\max|x_{ii}|^2$ and $R = 1/\max|u_{ii}|^2$.

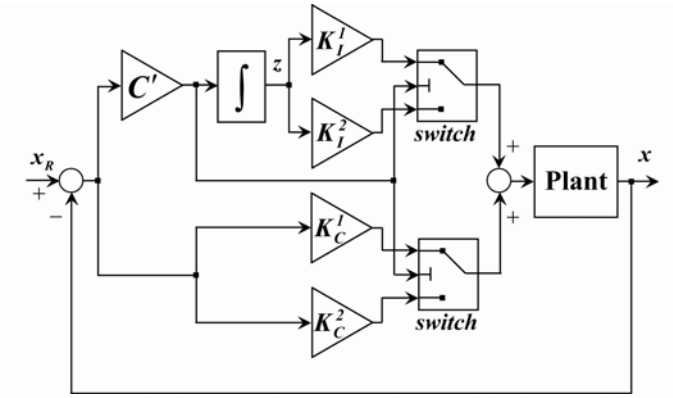

Fig. 7.1. Block diagram representing the controller-switching scheme

The simulated response of this controller to a step of 1 mm in the *x*-axis normalized to 1 is shown in Fig. 7.2(a) with a dash-dotted line. Although it had a fast response time, it generated a large overshoot. The second controller was designed for a smaller overshoot with the weight matrices given by (7.9) and $Q_I = 1\times10^{8}$. However, with this controller, we get a large settling time. The simulated response of this controller to a step of 1 mm normalized to 1 is shown in Fig. 7.2(a) with a dashed line. The values of controller gains for both the controllers are presented in the Table 7.1.

Table 7.1. Controller gains corresponding to the weight matrices given by (7.9)

$\boldsymbol{Q}_I$	$\boldsymbol{K}_C$	$\boldsymbol{K}_I$
10^8	[2510.16, 50.76]	10^4
10^{10}	[4182.04, 60.22]	10^5
10^{12}	[13784.36, 98.27]	10^6
10^{14}	[61008.15, 198.28]	10^7

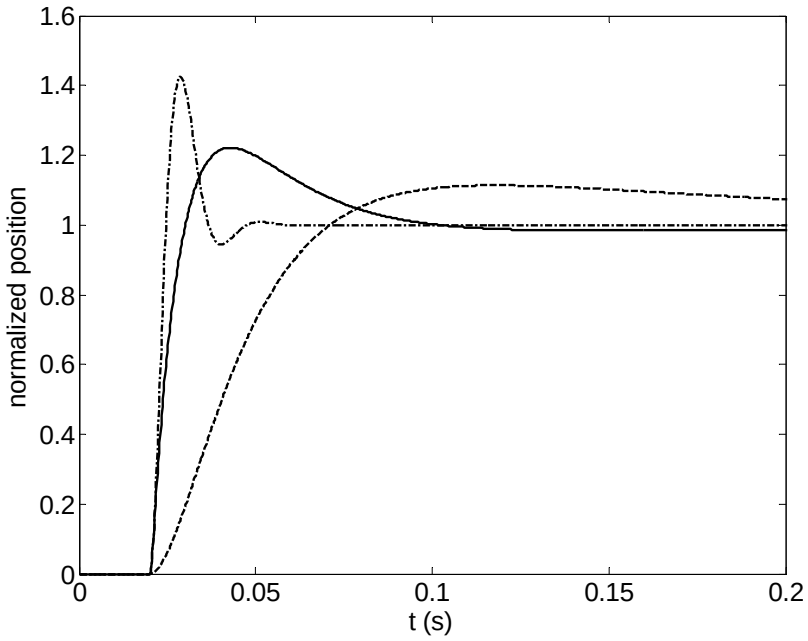

(a)

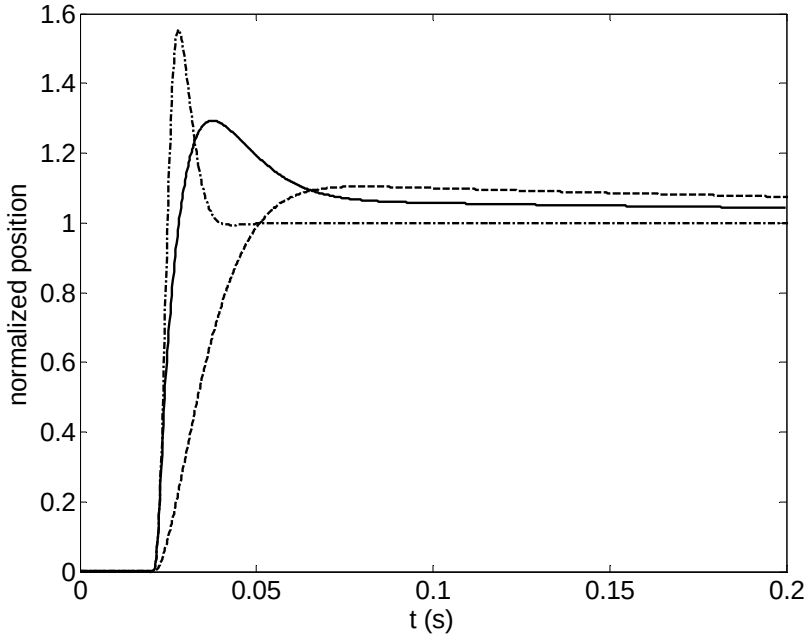

(b)

Fig. 7.2. (a) Simulations and (b) experimental verification of controller-switch scheme with a normalized 100-μm step response in x with $Q_1 = 10^{14}$ (dash-dotted), $Q_1 = 10^{8}$ (dashed), and the controller-switching scheme (solid)

Controller switching from the first to the second controller was triggered when the tracking-error reached 90% of the step size. This percentage yielded the best performance in terms of the overshoot as well as the rise and settling times and was obtained after a few iterations. The simulated response of the composite controller with the controller-switching scheme is shown in Fig. 7.2(a) with a solid line. This composite controller was able to reduce the percentage overshoot from 40.97% to 3.13% compared with the first controller. The rise and settling times were reduced from 39.3 ms and more than 450 ms to 18.7 ms and 330 ms, respectively compared with the second controller. Experimental verification of the three responses with the maglev nanopositioner is shown in Fig. 7.2(b). There is a close match between the simulated and experimental responses with small mismatches in overshoot and rise and settling times. These mismatches might be because of the reduced-order plant TFs used for controller designs. Thus, it may be concluded that the controller-switching scheme can provide significant improvements in the conflicting performance specifications compared with the conventional optimal control techniques.

7.3.2 Integral-Reset Scheme

Another promising solution to the multiscale-control problem is to limit the size of the integral term during the time period until a new reference point is reached. This strategy is equivalent to converting a tracking problem to a regulation problem after a certain period of time. This method makes full use of the integral control action in the beginning and hence, does not increase the rise time. In effect, setting the integral term to zero is equivalent to slowing down the response of the system to reduce overshoot as it reaches the targeted reference point. Thus, if a controller is designed to give a good regulatory control, this resetting of the integral term will have an advantage of smaller response times as well as less overshoot. The value of the integral

state vector, ξ_p, is stored and updated every time the control input calculations are performed. Thus the only extra effort it takes to implement this scheme is simply an on/off switch for the integral term, K_I, of the controller gain calculated with a conventional optimal control method.

Fig. 7.3 shows a block diagram to implement the integral-reset scheme. The weight matrices used to calculate the controller gain are given by (7.7) with $Q_I = 1 \times 10^{10}$. The values of the corresponding controller gains are presented in Table 7.1. The integral term was switched off when the tracking error reached 70% of the step size. This percentage was chosen to make full use of the integral action in the beginning and for the best performance in terms of overshoot as well as rise and settling times.

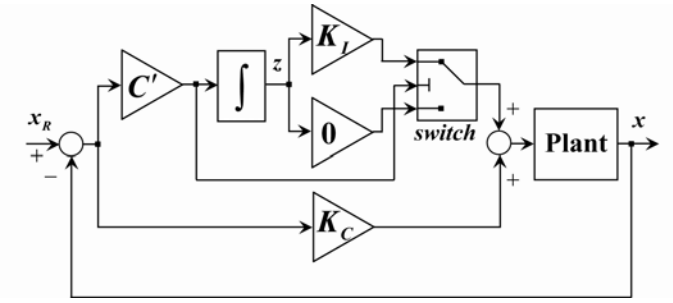

Fig. 7.3. Block diagram representing the integral-reset scheme

The simulated responses of the plant in the *x*-axis to a step of 1 mm with (solid) and without (dashed) the integral-reset scheme are shown in Fig. 7.4(a). The overshoot was reduced from 23.16% to 1.15% with this method without any significant negative effect on the rise time. Additionally, the settling time was reduced from 123 ms to 46 ms. For simulations, I used the analytical plant model. To completely switch off the integral term, the identified plant model could not be used since it had no inherent integrator. Thus, switching off the integral term completely would result in a non-zero steady-state error which is undesirable. This can be seen from the experimental results presented in the Fig. 7.4(b) with the same controller designs and

switching time as used for the simulations. This poses a limitation on the type of plants on which this method can be effectively applied.

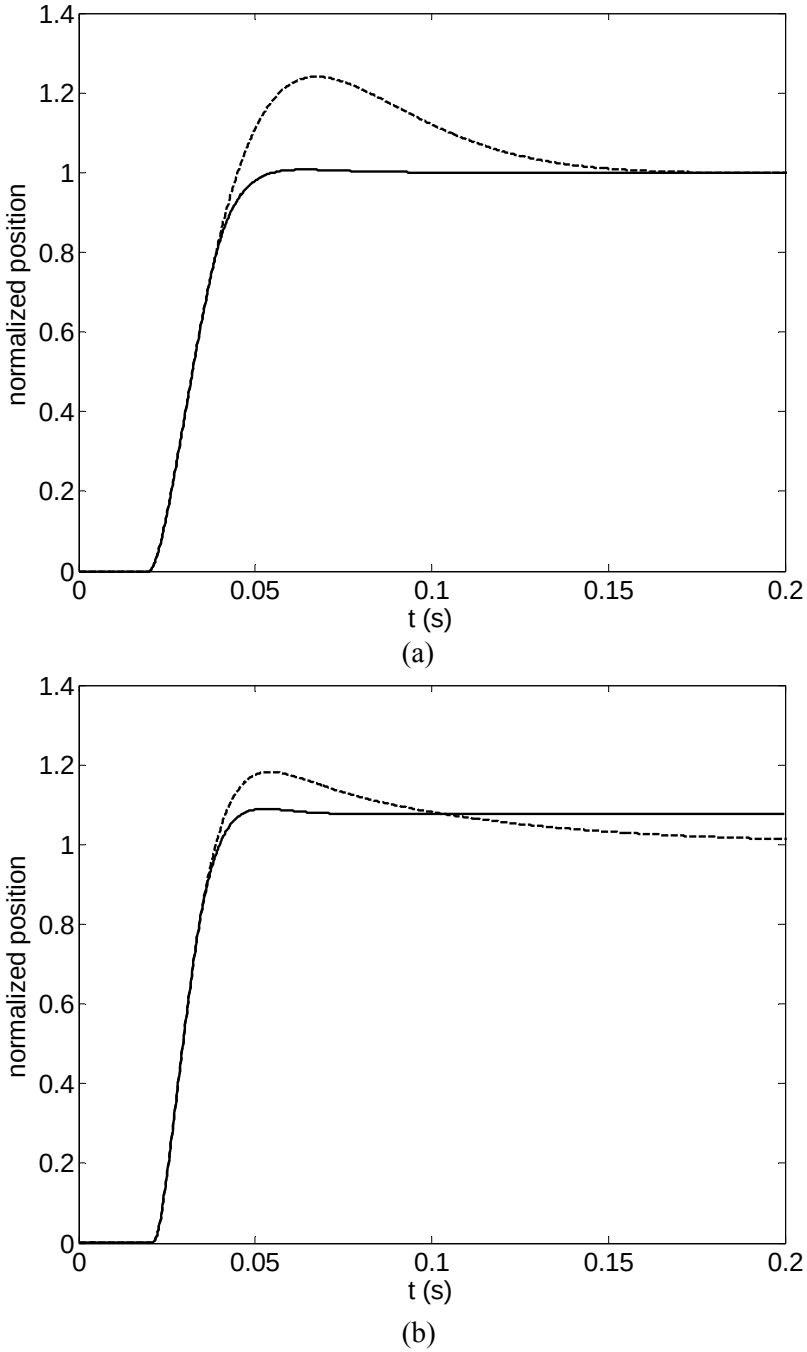

Fig. 7.4. (a) Simulation and (b) experimental verification of the integral-reset scheme with a normalized 100-μm step response in x with $Q_I = 10^{10}$ (dashed) and the integral-reset scheme (solid)

The above two schemes may be applied together sequentially to take the full advantages of both schemes. The motivation to devise this composite scheme, namely the controller switching with integral reset, originates from the following facts:

1. In the controller-switching technique, although there is a reduction in the overshoot, the difference in the response time compared with the fast controller may be significant depending on how much overshoot is acceptable. In other words, the rise-time of the composite controller may be close to the slow controller if the fast controller is used only for a very short period of time.
2. The integral-reset scheme makes the most of the fast controller in the beginning and tends to slow down the response when the integral term is turned off.

Thus, the issue of slow response may be resolved by using the fast control with integral-reset scheme in the beginning and then using the slower controller subsequently.

Fig. 7.5 shows the response to a 1-mm step command in the *x*-axis with the integral-reset plus controller-switching scheme. The controller-switching method was used with a combination of the controllers with the weight matrices given by (7.7) and $Q_I = 1\times10^{14}$ and 1×10^{8}. Switching was done when the tracking error reached 5% of the step command. The integral-reset method was used on the fast controller with the integral term being put to rest when the tracking error reached 60% of the step command. The switching criteria were set in order to obtain the best dynamic performance in terms of all three time-domain specifications, namely percentage overshoot, rise time, and settling time. With this composite multiscale control scheme, the percentage overshoot was reduced from 40.97% with $Q_I = 1\times10^{14}$ and 23.16% with $Q_I = 1\times10^{10}$ to 10.49%. It also shows a significant improvement in rise time from 20.9 to 6.0 ms compared with the optimal PI controller with $Q_I = 10^{10}$.

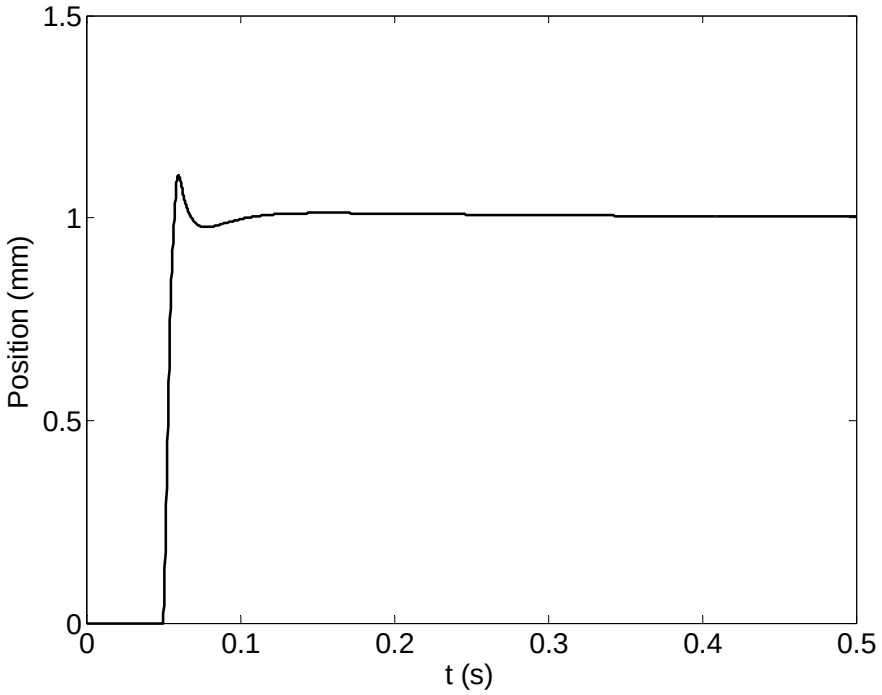

Fig. 7.5 Step response in x with the controller-switching plus the integral-reset scheme

7.3.3 Reduced-Order Model-Following Scheme

In this subsection, the controller design is carried out with a general linear time-invariant state-space model, deferring the results from the maglev positioner to be presented subsequently. This helps in proving that although the application of this method is demonstrated for the control of a maglev system, it essentially works well with a general class of higher-order LTI systems with or without open-loop instability and plant model uncertainties.

A. Controller Design

A model-following approach may also be used to alleviate the overshoot problem. Conventional model-following schemes try to make the output of the plant, $\boldsymbol{y}_p$, follow the output

of a reference model, $\boldsymbol{y_m}$, as closely as possible. The reference model is a dynamic model which has $\boldsymbol{y_R}$ as its input vector. A major disadvantage of the model-following scheme is that the original system's state vector is appended with the model's states, and hence the order of the overall plant dynamics increases. This requires a Riccati equation of higher order to be solved and an additional gain matrix to be stored.

A modified version of the model-following scheme is used here that does not require any additional states [43]. Consider a reference model of the form.

$$\begin{aligned} \dot{\boldsymbol{x}}_{\boldsymbol{m}} &= A_m \boldsymbol{x}_m + B_m \boldsymbol{u}_{\boldsymbol{m}} \\ \boldsymbol{y}_{\boldsymbol{m}} &= C_m \boldsymbol{x}_{\boldsymbol{m}} \end{aligned} . \tag{7.10}$$

The A_m, B_m, and C_m matrices in this reference model are assumed to be the same as those of the plant in (7.1). An approach to ensure that the reference model has a suitable reference-tracking response with little or no overshoot is to specify $\boldsymbol{u_m}$ as

$$\boldsymbol{u}_{\boldsymbol{m}} = \boldsymbol{u}_{\boldsymbol{R}} + K_C \left(\boldsymbol{x}_{\boldsymbol{R}} - \boldsymbol{x}_{\boldsymbol{m}} \right), \tag{7.11}$$

where K_C is the control gain matrix specified in (7.7). Using an analogous derivation as outlined in Section 7.2, we get

$$\begin{aligned} \dot{\tilde{\boldsymbol{x}}}_{\boldsymbol{m}} &= \tilde{A}_p \tilde{\boldsymbol{x}}_{\boldsymbol{m}} + \tilde{B}_p \boldsymbol{e}_{\boldsymbol{u_m}} \\ \tilde{\boldsymbol{y}}_{\boldsymbol{m}} &= \tilde{C}_p \tilde{\boldsymbol{x}}_{\boldsymbol{m}} \end{aligned} . \tag{7.12}$$

Define $\delta \boldsymbol{x} = \tilde{\boldsymbol{x}}_{\boldsymbol{p}} - \tilde{\boldsymbol{x}}_{\boldsymbol{m}}$, $\delta \boldsymbol{y} = \tilde{\boldsymbol{y}}_{\boldsymbol{p}} - \tilde{\boldsymbol{y}}_{\boldsymbol{m}}$, $\delta \boldsymbol{u} = \boldsymbol{u}_{\boldsymbol{p}} - \boldsymbol{u}_{\boldsymbol{m}}$. Then, the error dynamics is

$$\begin{aligned} \delta \dot{\boldsymbol{x}} &= \tilde{A}_p \delta \boldsymbol{x} + \tilde{B}_p \delta \boldsymbol{u} \\ \delta \boldsymbol{y} &= \tilde{C}_p \delta \boldsymbol{x} \end{aligned} . \tag{7.13}$$

The optimal PI control law for this plant is given by

$$\boldsymbol{u}_{\boldsymbol{p}} = \boldsymbol{u}_{\boldsymbol{m}} + K_C \left(\boldsymbol{x}_{\boldsymbol{m}} - \boldsymbol{x}_{\boldsymbol{p}} \right) + K_I \int_0^t \left(\boldsymbol{y}'_{\boldsymbol{m}} - \boldsymbol{y}'_{\boldsymbol{p}} \right) d\tau . \tag{7.14}$$

Using (7.11) and (7.14), we get

$$\boldsymbol{u_p} = \boldsymbol{u_R} + K_C\left(\boldsymbol{x_R} - \boldsymbol{x_p}\right) + K_I\int_0^t \left(\boldsymbol{y'_m} - \boldsymbol{y'_p}\right)d\tau\,. \tag{7.15}$$

This control law has essentially the same structure as that of the conventional optimal PI control given by (7.7) with $\boldsymbol{y'_R}$ replaced by $\boldsymbol{y'_m}$ in the integral term.

It may be proved that the reduced-order model-following scheme reduces the problem of overshoot subject to some conditions. Consider the plant and model dynamics defined by (7.1) and (7.10) respectively. The reference input dynamics is given by

$$\dot{\boldsymbol{x}}_{\boldsymbol{R}} = 0 = A_p\boldsymbol{x_R} + B_p\boldsymbol{u_R}\,. \tag{7.16}$$

Using the new set of variable defined in (7.2) and substituting the control law from reduced-order model-following scheme (7.14) in (7.1), we get

$$\dot{\boldsymbol{x}}_{\boldsymbol{p}} - \dot{\boldsymbol{x}}_{\boldsymbol{R}} = \left(A_p - B_pK_C\right)\left(\boldsymbol{x_p} - \boldsymbol{x_R}\right) + B_pK_I\int_0^t \left(\boldsymbol{y'_m}(\tau) - \boldsymbol{y_p}(\tau)\right)d\tau$$

or

$$\dot{\boldsymbol{x}}_{\boldsymbol{p}} = \left(A_p - B_pK_C\right)\left(\boldsymbol{x_p} - \boldsymbol{x_R}\right) + B_pK_IC'_p\int_0^t \left(\boldsymbol{x_m}(\tau) - \boldsymbol{x_p}(\tau)\right)d\tau\,. \tag{7.17}$$

Similarly, using the new set of variables defined in (7.12) and using (7.10) and (7.16), we get

$$\dot{\boldsymbol{x}}_{\boldsymbol{m}} - \dot{\boldsymbol{x}}_{\boldsymbol{R}} = A_p\left(\boldsymbol{x_m} - \boldsymbol{x_R}\right) + B_p\left(\boldsymbol{u_m} - \boldsymbol{u_R}\right). \tag{7.18}$$

From the control law defined by (7.11) and using (7.18), we get

$$\dot{\boldsymbol{x}}_{\boldsymbol{m}} = \left(A_p - B_pK_C\right)\left(\boldsymbol{x_m} - \boldsymbol{x_R}\right). \tag{7.19}$$

Subtracting (7.19) from (7.17), we get

$$\dot{\boldsymbol{x}}_{\boldsymbol{p}} - \dot{\boldsymbol{x}}_{\boldsymbol{m}} = \left(A_p - B_pK_C\right)\left(\boldsymbol{x_p} - \boldsymbol{x_m}\right) - B_pK_IC'_p\int_0^t \left(\boldsymbol{x_p}(\tau) - \boldsymbol{x_m}(\tau)\right)d\tau\,. \tag{7.20}$$

Differentiating (7.20) with respect to *t* gives

$$\ddot{\boldsymbol{x}}_{\boldsymbol{p}} - \ddot{\boldsymbol{x}}_{\boldsymbol{m}} = \left(A_p - B_pK_C\right)\left(\dot{\boldsymbol{x}}_{\boldsymbol{p}} - \dot{\boldsymbol{x}}_{\boldsymbol{m}}\right) - B_pK_IC'_p\left(\boldsymbol{x_p} - \boldsymbol{x_m}\right), \tag{7.21}$$

with initial condition $\boldsymbol{x}_p(0) - \boldsymbol{x}_m(0) = \mathbf{0}$. Therefore, from (7.20), we have $\dot{\boldsymbol{x}}_p(0) - \dot{\boldsymbol{x}}_m(0) = \mathbf{0}$. The solution of (7.21) with these initial conditions is given by

$$\boldsymbol{x}_m(t) = \boldsymbol{x}_p(t). \tag{7.22}$$

Equation (7.22) shows that the model states follow the plant states. Furthermore, the integral term in (7.20) is eliminated, provided (a) the initial states of the model are equal to those of the plant and (b) the plant and model system matrices are identical. This justifies the need to find an accurate plant model through system identification in Chapter V. In the presence of modeling errors, the integral windup will be small as long as the model output $\boldsymbol{y}_m$ is close to the plant output $\boldsymbol{y}_p$. Thus the problem of excessive overshoot due to the integral action is reduced without increasing the closed-loop plant order, requiring different controller gains and subsequent controller switching, or requiring the perfect knowledge of the plant TF or initial plant states. The effect of mismatch between the initial plant and model states will be further discussed in the following section.

B. Implementation on Maglev Positioner

A block diagram showing the implementation of the proposed control scheme on the plant model (7.8) is shown in Fig. 7.6. Step responses to a 1-mm command using the conventional optimal control as well as the proposed multiscale control are shown in Fig. 7.7. They support the claim made in Section 7.1 that a single controller cannot be used to achieve good load-change as well as reference-tracking performance objectives. The reduced-order model-following scheme, on the other hand, is capable of meeting both the objectives with a single set of controller gains, and without requiring any abrupt changes in the gain values.

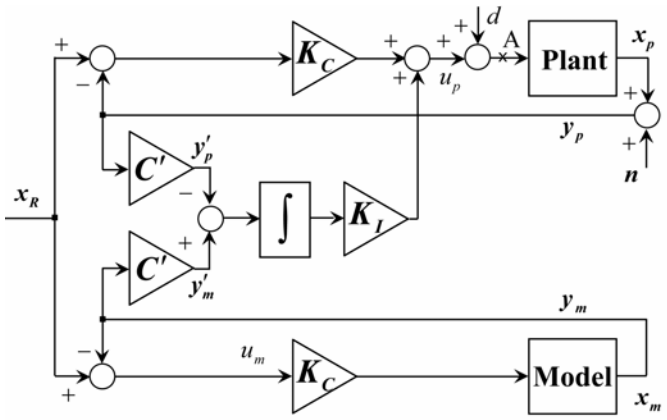

Fig. 7.6. Block diagram representing the reduced-order model-following scheme

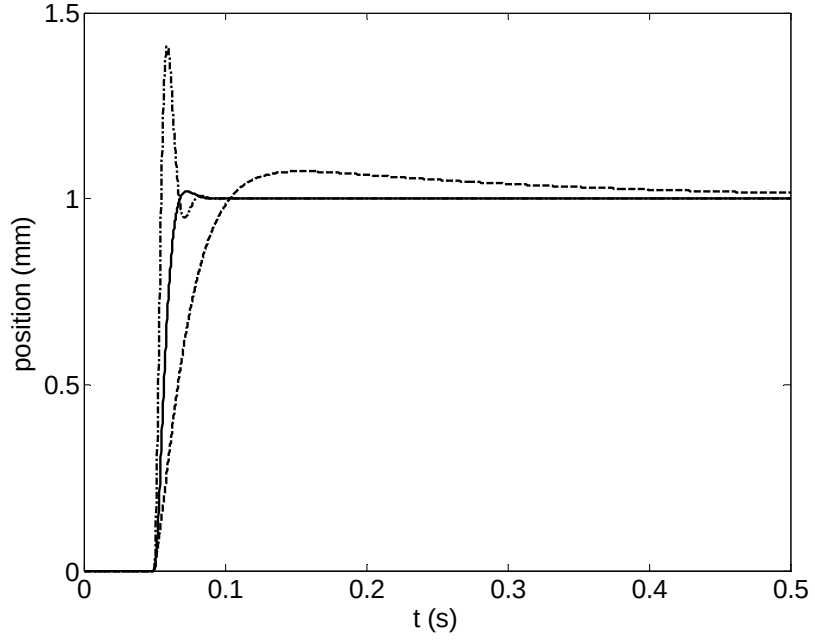

Fig. 7.7. 1-mm step responses in x with the reduced-order model-following scheme with $Q_I = 10^{12}$ (solid), and conventional LQ controllers with $Q_I = 10^{8}$ (dashed) and $Q_I = 10^{14}$ (dash-dotted)

This control scheme was tested for three different controllers with the weight matrices given by (7.9) and $Q_I = 1\times10^{8}$, 1×10^{10} and 1×10^{12}, respectively. The values of the controller gains for these controllers are presented in Table 7.2. Step responses to a 1-mm command with

these controllers are shown in Fig. 7.8. It can be seen from the figure that for all three chosen values of the integral terms, the reduced-order model-following scheme gives minimal (2.12% for $Q_I = 10^{12}$) or no overshoot ($Q_I = 10^8$).

Table 7.2. Comparison among the three proposed multiscale control schemes

Method	Q_I	**Overshoot (%)**	**Rise time (ms)**	**Settling time (ms)**
Optimal-control	10^8	7.33	39.3	>450
Controller-switching	10^8, 10^{14}	3.13	18.7	330
Optimal control	10^{10}	23.16	20.9	123
Integral-reset	10^{10}	1.15	21.9	46
Integral-reset plus Controller-switching	10^8, 10^{14}	10.49	6.0	161
Model-following	10^8	0.00	46.1	85
Model-following	10^{10}	0.05	28.6	45
Model-following	10^{12}	2.12	12.9	30

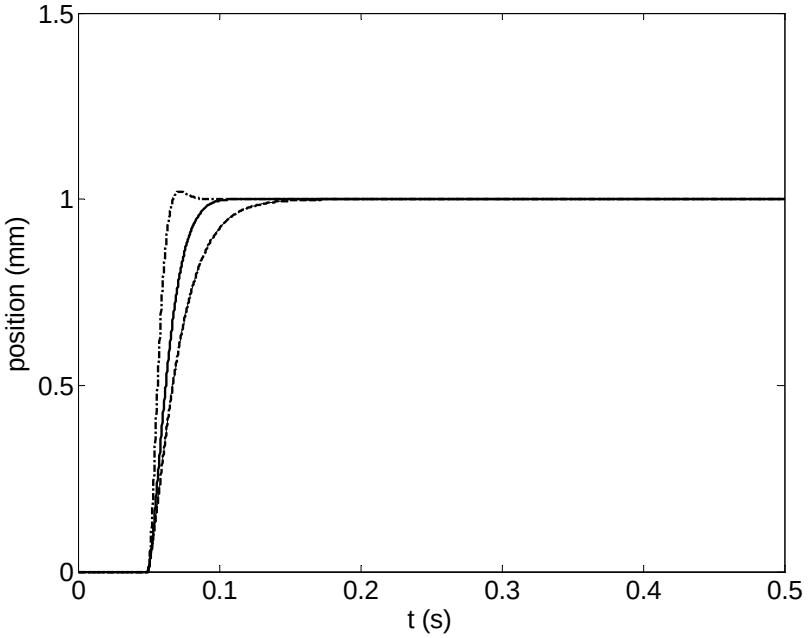

Fig. 7.8. 1-mm step response in x with the reduced-order model-following scheme with $Q_I = 10^8$ (dashed line), $Q_I = 10^{10}$ (solid line), and $Q_I = 10^{12}$ (dash-dotted line)

Fig. 7.9 shows the 1-mm and 100-nm step responses for positive and negative steps, normalized to unity for comparison. The plot demonstrates that the multiscale control scheme gives identical performances at nano- as well as macro-scale, except for the noise level, thus justifying the term *multiscale* defined in the Section 7.1. It also shows that the controller design results in repeatable performance and the results presented herein are not based on a single set of experiments.

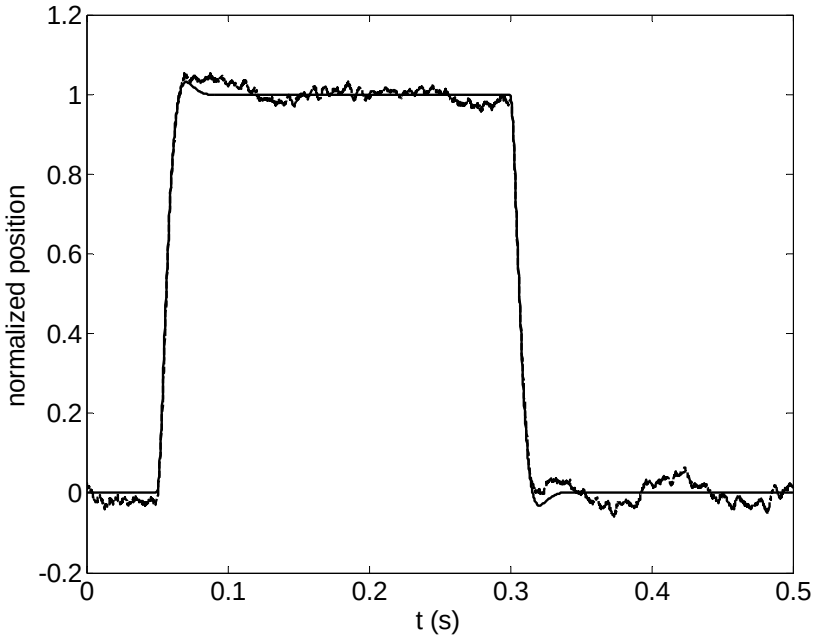

Fig. 7.9. 1-mm (solid) and 100-nm (dashed) step responses, normalized to 1 for comparison, with the reduced-order model-following scheme

7.3.4 Comparison among the Three Proposed Methods

A comparison of performances of the three methods is presented in this subsection. Table 7.2 gives the values of overshoot, rise time (with the 90% criterion), and settling time (with the 1% criterion) of the plant to a step command of 1mm. The values of Q and R matrices defined by (7.9) are kept identical for the sake of fair comparison. As summarized in Table 7.2,

the controller-switching scheme gave a good rise time performance while the integral-reset scheme provided a better overshoot performance. The integral-reset scheme with controller switching improved the rise-time significantly, but adversely affected the overshoot and settling time. Hence this scheme is not recommended in the applications that cannot tolerate large overshoot. The model-following approach, on the other hand, gave the best overall performance. The overshoot was comparable with that of the integral-reset scheme, while the rise-time was almost as good as the controller-switching method, particularly with the higher values of Q_l. At the same time, it showed a good settling-time performance as well, which is a shortcoming with the other two methods. Thus I continued further analysis concerning stability, uncertainties, and robustness in the presence of process and measurement noises for this third method alone. This analysis is presented in Section 7.4.

I conclude this section by making a remark that the methods discussed in this section are valid for any LTI plant with higher order as long as the assumptions and conditions noted in Sections 7.2 and 7.3 are valid. In particular, the controller-switching method may be devised for any given plant with a set of controllers to meet the conflicting requirements individually and then use the controllers sequentially. The integral-reset scheme may be applied to any *n*-th-order plant with *r* inputs as long as an integral action is desired for r_0 states with $r_0 \le r$. The model-following scheme may similarly be used with any *n*-th-order plant with *n*-th-order model.

7.4 Performance Analyses for Reduced-Order Model-Following Method

In this section, the analyses of the performance of the reduced-order model-following scheme are presented in terms of closed-loop stability, initial state uncertainties, and input and output sensitivities.

A. Closed-Loop Stability

Since modified optimal LQ control methodologies are used to design the controllers and since full state feedback is available, we have the advantage of the guaranteed stability margins, i.e., the gain margin (GM) between 6 dB and ∞, and the PM greater than 60° [78]. This may be verified by doing a Nyquist stability analysis at any loop-breaking point in the closed loop. Particularly for the model-following scheme, wherein the control gains are modified, these stability margins need to be verified. Although it is apparent from the step responses shown in the Figs. 7.7–7.9 that these control schemes give stable control loops, a formal stability analysis is still necessary to find how much uncertainty can be tolerated in the closed loop. Fig. 7.10 shows the Nyquist plot for the reduced-order model-following scheme at the loop-breaking point 'A' in Fig. 7.6.

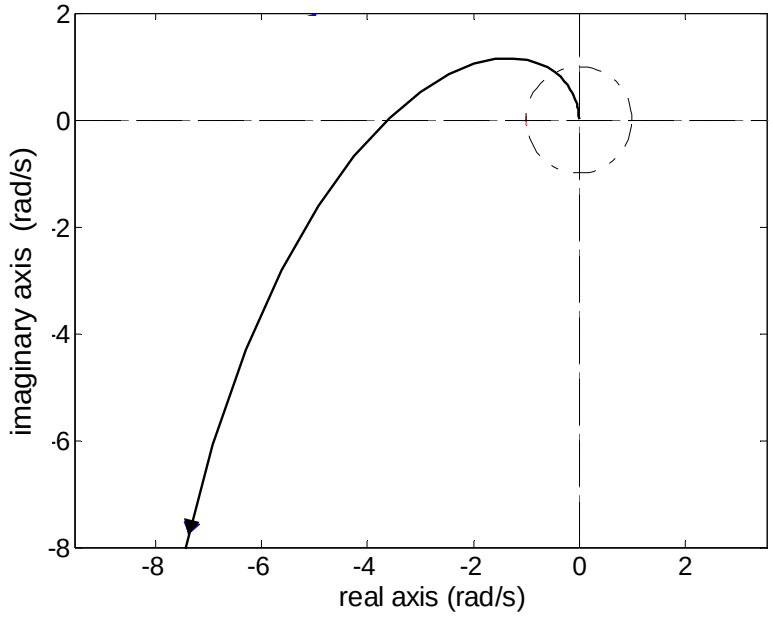

Fig. 7.10. Nyquist plot showing the stability margins of the reduced-order model-following scheme at control-input loop-breaking point to the plant 'A' in Fig. 7.6

Since there is an unstable pole in the plant TF and the Nyquist plot encircles the –1 point in the complex plane in the counterclockwise direction once, we have a stable closed loop from the Nyquist criteria. Furthermore, in this case, the closed-loop has a GM of at least 11.2 dB and a PM of at least 63°.

B. Performance with Initial-State Mismatch

In Subsection 7.3.3-A, I demonstrated that the integral term of the controller is eliminated provided the initial states match perfectly. Furthermore, in the presence of modeling errors, the integral windup will be small as long as the model output $\boldsymbol{y_m}$ is close to the plant output $\boldsymbol{y_p}$. Here, I demonstrate that even in the presence of initial-state mismatches as much as ±20%, the model states converge to the plant states in about the same time as without any mismatch. This percentage is chosen only to demonstrate the effect of mismatch; the plant states track the desired reference inputs no matter how large the initial mismatch is. Fig. 7.11 demonstrates this situation where the initial state vector of the model is not identical to that of the actual plant. The model states are shown with solid lines while the actual plant states are shown with dashed (+20% mismatch) and dash-dotted lines (–20% mismatch). With imperfect knowledge of initial plant states, the dynamic performance is moderately affected in terms of overshoot. However, there is no significant change in the rise and settling times and the steady-state errors. Furthermore, the model states converge to plant states in almost the same time. This implies that for any reference-tracking problem, if the initial plant states are not known perfectly, a dummy step can be given to allow the models states to become identical to those of plant. Any subsequent meaningful tracking can be then done without any error.

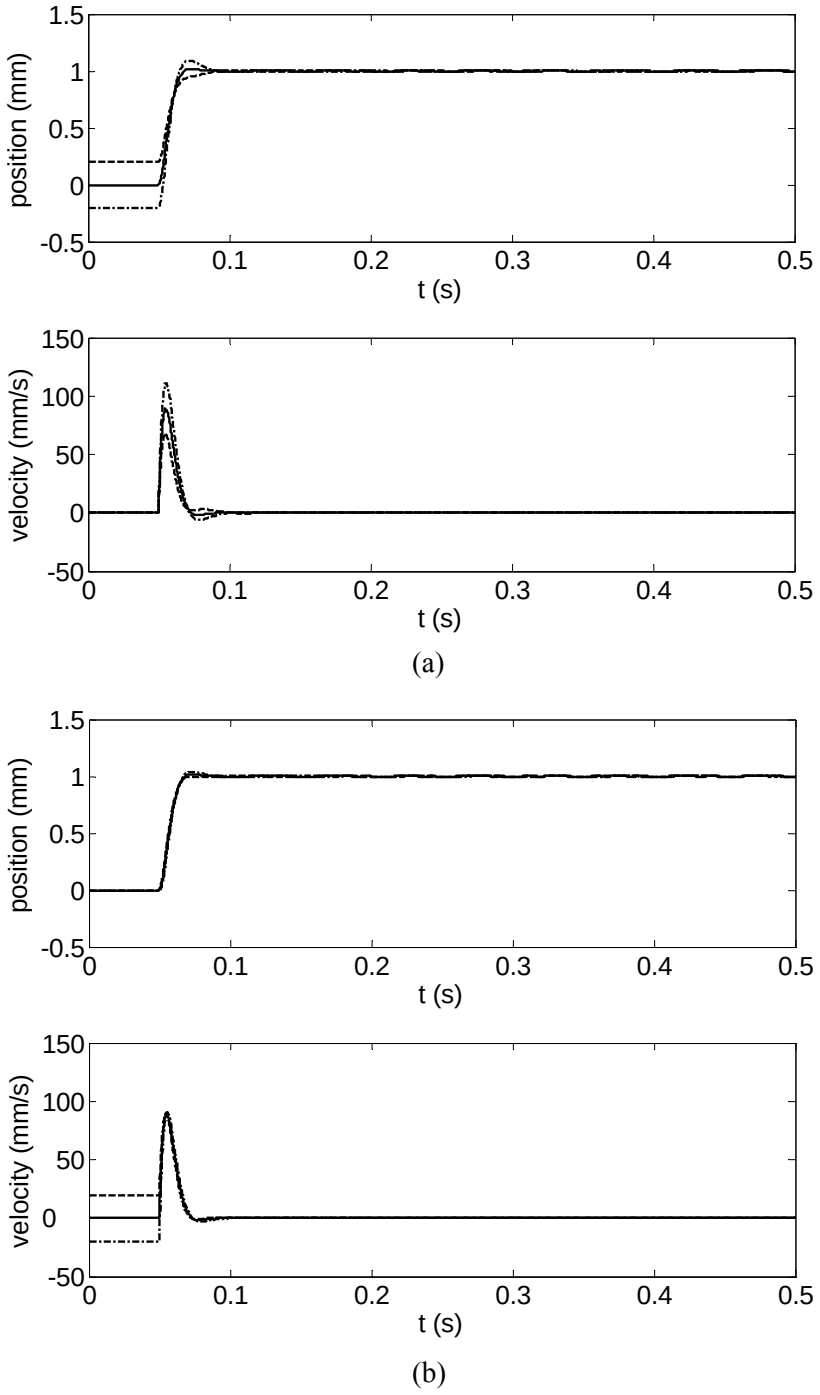

Fig. 7.11. Model states (solid) and responses of the plant with the multiscale control scheme in the presence of the mismatch between the plant and model initial states with a difference of +20% (dashed) and –20% (dash-dotted) in (a) position and (b) velocity

C. Performance in the Presence of Noises

Another analysis of particular interest is the robustness of the designed controller to process and measurement noise. Consider the combined closed-loop system given by

$$\begin{bmatrix} \dot{\tilde{\boldsymbol{x}}}_{\boldsymbol{p}} \\ \dot{\tilde{\boldsymbol{x}}}_{\boldsymbol{m}} \end{bmatrix} = \begin{bmatrix} \tilde{A}_p & 0 \\ 0 & \tilde{A}_p \end{bmatrix} \begin{bmatrix} \tilde{\boldsymbol{x}}_{\boldsymbol{p}} \\ \tilde{\boldsymbol{x}}_{\boldsymbol{m}} \end{bmatrix} + \begin{bmatrix} \tilde{B}_p & 0 \\ 0 & \tilde{B}_p \end{bmatrix} \begin{bmatrix} \boldsymbol{e}_{u_p} + \boldsymbol{d} \\ \boldsymbol{e}_{u_m} \end{bmatrix}$$
$$\begin{bmatrix} \tilde{\boldsymbol{y}}_{\boldsymbol{p}} \\ \tilde{\boldsymbol{y}}_{\boldsymbol{m}} \end{bmatrix} = \begin{bmatrix} \tilde{C}_p & 0 \\ 0 & \tilde{C}_p \end{bmatrix} \begin{bmatrix} \tilde{\boldsymbol{x}}_{\boldsymbol{p}} \\ \tilde{\boldsymbol{x}}_{\boldsymbol{m}} \end{bmatrix} + \begin{bmatrix} \boldsymbol{n} \\ \boldsymbol{0} \end{bmatrix}. \tag{7.23}$$

where $\boldsymbol{d}$ and $\boldsymbol{n}$ are process and measurement noises as indicated in Fig. 7.6. For input sensitivity, assuming $\boldsymbol{n} = \boldsymbol{0}$ and using the control laws (7.11) and (7.15), we get

$$\begin{aligned} \begin{bmatrix} \dot{\tilde{\boldsymbol{x}}}_{\boldsymbol{p}} \\ \dot{\tilde{\boldsymbol{x}}}_{\boldsymbol{m}} \end{bmatrix} &= \begin{bmatrix} \tilde{A}_p & 0 \\ 0 & \tilde{A}_p \end{bmatrix} \begin{bmatrix} \tilde{\boldsymbol{x}}_{\boldsymbol{p}} \\ \tilde{\boldsymbol{x}}_{\boldsymbol{m}} \end{bmatrix} - \begin{bmatrix} \tilde{B}_p & 0 \\ 0 & \tilde{B}_p \end{bmatrix} \begin{bmatrix} \begin{bmatrix} K_C & K_I \end{bmatrix} & \begin{bmatrix} 0 & -K_I \end{bmatrix} \\ \begin{bmatrix} 0 & 0 \end{bmatrix} & \begin{bmatrix} K_C & 0 \end{bmatrix} \end{bmatrix} \begin{bmatrix} \tilde{C}_p & 0 \\ 0 & \tilde{C}_p \end{bmatrix} \begin{bmatrix} \tilde{\boldsymbol{x}}_{\boldsymbol{p}} \\ \tilde{\boldsymbol{x}}_{\boldsymbol{m}} \end{bmatrix} + \begin{bmatrix} \tilde{B}_p & 0 \\ 0 & \tilde{B}_p \end{bmatrix} \begin{bmatrix} \boldsymbol{d} \\ \boldsymbol{0} \end{bmatrix} \\ &= \begin{bmatrix} \tilde{A}_p - \tilde{B}_p K \tilde{C}_p & -\tilde{B}_p \begin{bmatrix} 0 & -K_I \end{bmatrix} \tilde{C}_p \\ 0 & \tilde{A}_p - \tilde{B}_p \begin{bmatrix} K_C & 0 \end{bmatrix} \tilde{C}_p \end{bmatrix} \begin{bmatrix} \tilde{\boldsymbol{x}}_{\boldsymbol{p}} \\ \tilde{\boldsymbol{x}}_{\boldsymbol{m}} \end{bmatrix} + \begin{bmatrix} \tilde{B}_p \boldsymbol{d} \\ \boldsymbol{0} \end{bmatrix}. \end{aligned} \tag{7.24}$$

Using Laplace transforms on both sides and assuming zero initial conditions, we get

$$\begin{bmatrix} \tilde{\boldsymbol{X}}_{\boldsymbol{p}}(s) \\ \tilde{\boldsymbol{X}}_{\boldsymbol{m}}(s) \end{bmatrix} = \begin{bmatrix} sI - \tilde{A}_p + \tilde{B}_p K \tilde{C}_p & \tilde{B}_p \begin{bmatrix} 0 & -K_I \end{bmatrix} \tilde{C}_p \\ 0 & sI - \tilde{A}_p + \tilde{B}_p \begin{bmatrix} K_C & 0 \end{bmatrix} \tilde{C}_p \end{bmatrix}^{-1} \begin{bmatrix} \tilde{B}_p \boldsymbol{D}(s) \\ \boldsymbol{0} \end{bmatrix}. \tag{7.25}$$

Using the matrix identity [78]

$$\begin{bmatrix} A_{11} & A_{12} \\ A_{21} & A_{22} \end{bmatrix}^{-1} = \begin{bmatrix} A_{11}^{-1} + A_{11}^{-1} A_{12} X^{-1} A_{21} A_{11}^{-1} & -A_{11}^{-1} A_{12} X^{-1} \\ -X^{-1} A_{21} A_{11}^{-1} & X^{-1} \end{bmatrix}, \tag{7.26}$$

where $X \triangleq A_{22} - A_{21} A_{11}^{-1} A_{12}$, we get

$$\begin{bmatrix} \tilde{\boldsymbol{X}}_{\boldsymbol{p}}(s) \\ \tilde{\boldsymbol{X}}_{\boldsymbol{m}}(s) \end{bmatrix} = \begin{bmatrix} \left(sI - \tilde{A}_p + \tilde{B}_p K \tilde{C}_p \right)^{-1} & \times \\ 0 & \left(sI - \tilde{A}_p + \tilde{B}_p \begin{bmatrix} K_C & 0 \end{bmatrix} \tilde{C}_p \right)^{-1} \end{bmatrix} \begin{bmatrix} \tilde{B}_p \boldsymbol{D}(s) \\ \boldsymbol{0} \end{bmatrix}. \tag{7.27}$$

Thus the input sensitivity function T_d is given by

$$\|T_d\| = \frac{\left\|\tilde{\boldsymbol{X}}_p(s)\right\|}{\|D(s)\|} = \left\|\left(sI - \tilde{A}_p + \tilde{B}_p K \tilde{C}_p\right)^{-1} \tilde{B}_p\right\|. \tag{7.28}$$

The output sensitivity function T_n may be similarly found assuming $\boldsymbol{d} = \mathbf{0}$ and using the control laws (7.11) and (7.15). The TF is given by

$$\|T_n\| = \frac{\left\|\tilde{\boldsymbol{X}}_p(s)\right\|}{\|N(s)\|} = \left\|\left(sI - \tilde{A}_p + \tilde{B}_p K \tilde{C}_p\right)^{-1} \tilde{B}_p K\right\|. \tag{7.29}$$

Fig. 7.12(a) and (b) respectively show the input and output sensitivity TFs for the maglev positioner using (7.28–7.29). The output of the plant is not affected significantly by the input disturbances. The process noise at the input end to the plant is physical in nature and is expected to be of low frequency. For the entire frequency range the maximum amplification of these disturbances is around –80 dB at around 20 Hz. The measurement noises, on the other hand, have high-frequency contents. For the frequencies greater than 1 kHz, the amplification of the position measurement is less than –60 dB, whereas that of velocity measurement is less than –25 dB. Thus, the reduced-order model-following scheme offers almost the same level of performances even in the presence of process as well as measurement noises.

7.5 Summary

The main focus of this chapter was to present multiscale control techniques which can be used to meet conflicting time-domain performance specifications at nano- as well as macro-scale. Plant models from the closed-loop system identification results from Chapter V were used to design the controllers. In particular, emphasis was given to the requirement of achieving little or no overshoot with a zero steady-state error and fast dynamic response in terms of rise and settling times. Semiconductor manufacturing is such an application, wherein these performance objectives translate into achieving nanoscale feature sizes at high throughput.

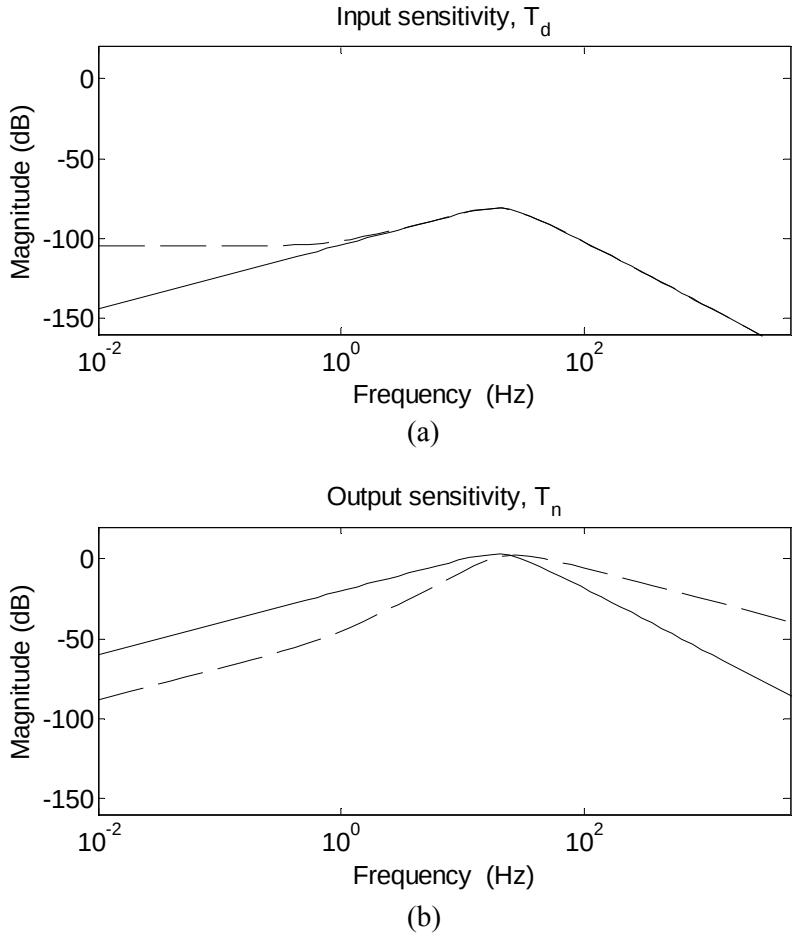

Fig. 7.12. (a) Input sensitivity TFs between the control input disturbance *d* and the states position (solid) and velocity (dashed), and (b) output sensitivity TFs between the measurement noises ***n*** and the respective states position (solid) and velocity (dashed)

Each of the three proposed multiscale control schemes were found to have certain benefits and limitations. The controller-switching scheme provided a fast response time. The main benefit of the integral-reset scheme was its simplicity and ease of implementation. The model-following approach was relatively complex. However, it provided the best results in terms of overshoot as well as response time. Furthermore, this method did not increase the overall order of the closed-loop system. Detailed performance analysis of this method was performed to

demonstrate its working on a practical system with problems like open-loop instability, unknown plant TF, imperfectly known initial plant states and presence of process and measurement noises.

All three multiscale control schemes were found to provide significantly improved responses compared with the conventional optimal PI control. In particular, the reduced-order model-following scheme gave identical performance for step sizes of 1 mm and 100 nm. The GM was found to be greater than 11.2 dB along with a PM of at least 63°. Furthermore, an initial mismatch between the plant and model states can also be sustained without losing stability or affecting the performance of the closed-loop significantly. In the presence of process and measurement noises, the attenuation is about 80 dB and 65 dB, respectively, in the frequency ranges of interest. The results presented herein were consistent and repeatable. Although only a linear system with a precisely known plant model was considered, the proposed multiscale-control method works well with a general class of higher-order LTI systems with or without open-loop instability.

CHAPTER VIII

CONCLUSIONS

This chapter summarizes the major contribution of this research. One of the main objectives of this dissertation was to develop nanoscale control strategies and motion planning to overcome the inherent technical challenges of the maglev positioning systems and to make them suitable to be used for commercial applications that require nanoscale position resolution. With the advances in electronics, medical and several other industries working with cutting-edge technologies, the role of precision positioning systems has become vital for nanopositioning and nanomanipulation. Currently available positioning technologies are able to provide good resolution but over very short travel range (a few tens to several hundred micrometers). Furthermore, with the increasing complexity of assembly, manufacturing, and metrology processes, multitasking will be a necessity in near future to increase the throughput. These demanding requirements call for a novel method for precision positioning in multiple DOF, with large travel range and nanoscale resolution at high control bandwidth. Two novel maglev stages were used as nanoscale positioning devices for industry applications that fulfill all the requirements mentioned above. The maglev systems have no mechanical contact between the moving and stationary parts. This non-contact nature of magnetic levitation facilitates its maintenance, eliminates wear in the mechanical parts, and increases their life spans, and do not require lubricants.

First of the two, namely the Δ-stage, is compact in size and capable of motion control in all 6 DOFs with the travel ranges of 300 μm in the three translations and 3.5 mrad in the three

rotations. The position resolution is better than 2 nm. It has the maximum speed capability of 0.5 m/s and the actuators are sized for 30 m/s^2 acceleration in horizontal direction. Due to a light-weight moving platen and compact design, there is a nominal power consumption of about 1 W by all the actuators in steady state. The Y-stage has an extended travel range of 5 mm × 5 mm in the horizontal axes and 500 μm in the *z*-axis, limited by the sensing range of the capacitance probes. The stage has noise level of 3 nm rms. This maglev stage has a very simple mechanical structure with a single moving part. It is easy and inexpensive to fabricate and can be easily taken out without disturbing rest of the assembly. This design makes it a very powerful positioning device that can be used as a cluster tool in applications requiring multitasking. In such applications, the same platen can be used for a variety of processes by changing the setup and all the processes can be completed with a fixed tool set. Analytical modeling, controller design and performance testing of the two maglev positioners were performed as a part of preliminary analysis. Both gave repeatable results with nanoscale precision for rigorous set-point-change as well as load-change tests.

A problem of potential interest was unavailability of accurate plant model. The pure-mass model obtained analytically with several assumptions was too simplistic and did not capture the low-frequency plant dynamics and coupling terms with fidelity. The effectiveness of any control strategy designed for a plant relies on the accuracy of plant model. To address this problem, system identification is required. System identification was particularly challenging in our because of the inherently unstable nature of maglev systems. I carried the conventional identification methods one step ahead in this research in order to obtain a more reliable, consistent, and complete plant models. Identification was performed using the BJ method with a closed-loop framework and a known controller structure. I performed the entire analysis using discrete-time equations to avoid any errors because of the continuous-to-discrete-time

conversions. An order-reduction algorithm was presented to reduce the order of the identified plant to a level at which the controller could be designed with ease and without loosing any significant dynamics of the plant within the control bandwidth. The closed-loop system responses with these models were found to have a significantly close match with simulated results. In the subsequent chapters, these identified models were used instead of the analytical ones for better and more reliable controller design.

Due to the use of a single-piece moving part to generate all the 6-axis motions and inaccuracies in the assembly of the actuator units relative to the platen, there are inherent and undesired couplings among the axes. A systematic procedure for designing a multivariable optimal control of the two maglev positioners was presented to reduce the effect of such couplings. Nonlinear equations of motion were derived using the Euler-angle approach, and a linearized plant model in state-space form was developed about an operating point. A comparison between the multivariable LQ controller and the decoupled SISO lead-lag controller revealed a reduction in coupling by about 97%. The control effort required for a given step size was reduced by a factor of 10. The peak velocity was also found to be reduced by 85.89%. It was concluded from the experimental results that the objectives of reduction in coupling as well as the control effort requirement were met with the designed LQ controller. However, the performance was found to be adversely affected in terms of settling time.

This problem of designing a controller to meet the conflicting time-domain performance specifications at nano- as well as macro-scale was covered separately in the multiscale control design. In particular, emphasis was given to the requirement of achieving little or no overshoot with a zero steady-state error and fast dynamic response in terms of rise and settling times. For practical applications, these performance objectives translate into achieving nanoscale position resolution at high throughput. Among the proposed control strategies, the controller-switching

scheme was found to provide a fast response time. The integral-reset scheme was particularly useful because of its simplicity and ease of implementation. The model-following approach gave the designer more control over the overshoot and provided the best results in terms of overshoot as well as response time. Emphasis was given on the fact that the proposed model-following method does not increase the overall order of the closed-loop system unlike the traditional model-following schemes. All three multiscale control schemes were found to provide significantly improved responses compared with the conventional optimal PI control. Detailed performance analysis of the proposed methods was performed to demonstrate their working on practical systems with problems like open-loop instability, unknown plant TF, imperfectly known initial plant states and presence of process and measurement noises. Although only a linear system with a precisely known plant model was considered, the proposed multiscale-control method works well with a general class of higher-order LTI systems with or without open-loop instability.

It was crucial in the presented research work to design controllers that can effectively reduce or eliminate the problems associated with the maglev positioners in order to make them usable for industry applications. Additionally, with the recent developments in nanomanipulation and nanomanufacturing, it is equally vital to device appropriate path-planning techniques for precision motion control. With this objective, key parameters that influence the dynamic behavior of the maglev positioning device were investigated, and ways to control these parameters were proposed. Design and implementation of a well-damped SISO lead-lag controller was described, and their influence on the performance of the maglev stage was discussed. Test results for key nanomanufacturing applications such as μSTL, DPN, and scanning were presented. The command-tracking errors were well within 20 nm pp with the best performance of 4.5 nm pp. The minimum achievable feature size is thus limited only by

manufacturing techniques and not by our maglev positioning technology. The experimental results demonstrated that the maglev stage performed well for these nanomanufacturing applications in terms of position resolution, accuracy, speed, and versatility.

With these results, the two maglev nanopositioners were shown to be a promising solution to nanopositioning requirements of the next-generation nanotechnology.

REFERENCES

[1] H. Doumanidis, “The nanomanufacturing programme at the National Science Foundation,” *Nanotechnology*, vol. 13, no. 3, pp. 248–252, Apr. 2002.

[2] M. Sitti, “Survey of nanomanipulation systems,” in *Proc. IEEE Conf Nanotechnology*, pp. 75–80, October 2001.

[3] W.-J. Kim, “High-precision planar magnetic levitation,” Ph.D. Dissertation, Dept. of Elect. Eng., Massachusetts Institute of Technology, Cambridge, MA, June 1997.

[4] X. Shan, S.-K. Kuo, J. Zhang, and C.-H. Menq, “Ultra precision motion control of a multiple degrees of freedom magnetic suspension stage,” *IEEE/ASME Tr. on Mechatronics*, vol. 7, no. 1, pp. 67–78, Mar. 2002.

[5] M. Holmes, R. Hocken, and D. L. Trumper, “The long-range scanning stage: a novel platform for scanned-probe microscopy,” *Precision Engineering*, vol. 24, no. 3, pp. 191–209, July 2000.

[6] E. Hajjaji and M. Ouladsine, “Modeling and nonlinear control of magnetic levitation systems,” *IEEE Tr. on Industrial Electronics*, vol. 48, no. 4, pp. 831–838, Aug. 2001.

[7] D. L. Trumper, W.-J. Kim, and M. E. Williams, “Design and analysis framework for permanent-magnet machines,” *IEEE Trans. on Industry Applications*, vol. 32, no. 2, pp. 371–379, Mar 1996.

[8] W.-J. Kim and D. L. Trumper, “High-precision magnetic levitation stage for photolithography,” *Precision Engineering*, vol. 22, no. 2, pp. 66–77, April 1998.

[9] S. Verma, W.-J. Kim, and H. Shakir, "Multi-axis maglev nanopositioner for precision manufacturing and manipulation applications," *IEEE Trans. on Industry Applications*, vol. 41, no. 5, pp. 1159–1167, Sep. 2005.

[10] J. Gu, W.-J. Kim, and S. Verma, "Nanoscale motion control with a compact minimum-actuator magnetic levitator," *ASME Journal of Dynamic Systems, Measurement and Control*, vol. 127, no. 3, pp. 433–442, Sep. 2005.

[11] K. S. Jung and Y. S. Baek, "Study on a novel contact-free planar system using direct drive DC coils and permanent magnets," *IEEE/ASME Tr. on Mechatronics*, vol. 7, no. 1, pp. 35–43, Mar. 2002.

[12] S. K. Kuo, X. Shan, and C. H. Menq, "Large travel ultra precision *x-y-θ* motion control of a magnetic-suspension stage," *IEEE/ASME Trans. on Mechatronics*, vol. 8, no. 3, pp. 334–341, Sep. 2003.

[13] D. N. Galburt, "Microlithographic apparatus," U.S. Patent 4,952,858, Aug. 28, 1990.

[14] D. N. Galburt and G. O'Connor, "Wafer stage with reference surface," U.S. Patent 5,285,142, Feb. 8, 1994.

[15] R. L. Hollis, S. E. Salcudean, and A. P. Allan, "A six degree-of-freedom magnetically levitated variable compliance fine-motion wrist: design, modeling, and control," *IEEE Trans. on Robotics and Automation*, vol. 7, no. 3, pp. 320–332, June 1991.

[16] R. L. Hollis, "Magnetically levitated fine motion wrist with programmable compliance," U.S. Patent 4,874,998, Oct. 17, 1989.

[17] H. Kano, “Optical pickup apparatus of thin type with magnetic circuit,” U.S. Patent 6,285,644 B1, Sep. 4, 2001.

[18] M. B. Khamesee, N. Kato, Y. Nomura, and T. Nakamura, “Design and control of a microrobotic system using magnetic levitation,” *IEEE/ASME Trans. on Mechatronics*, vol. 7, no. 1, pp. 1–13, Mar. 2002.

[19] M. Y. Chen, M. J. Wang, and L. C. Fu, “A novel dual-axis repulsive maglev guiding system with permanent magnet: modeling and controller design,” *IEEE/ASME Trans. on Mechatronics*, vol. 8, no. 1, pp. 77–86, March 2003.

[20] S. Dejima, W. Gao, K. Katakura, S. Kiyono, and Y. Tomita, “Dynamic modeling, controller design and experimental validation of a planar motion stage for precision positioning,” *Precision Engineering*, vol. 29, no. 3, pp. 263–271, July 2005.

[21] E. Villota and S. Jayasuriya, “Model based control of a multidimensional positioning system – A comparison of controller designs with experimental validation,” in *Proc. 2005 American Control Conference*, Portland, OR, pp. 1365–370, June 2005.

[22] R. Pintelon and J. Schoukens, “Box-Jenkins identification revisited–Part I: Theory,” *Automatica*, vol. 42, no. 1, pp. 63–75, Jan. 2006.

[23] R. Pintelon, Y. Rolain, and J. Schoukens, “Box-Jenkins identification revisited–Part II: Applications,” *Automatica*, vol. 42, no. 1, pp. 77–84, Jan. 2006.

[24] L Ljung, *System Identification: Theory for the User*, 2nd ed., Upper Saddle River, NJ: Prentice Hall, 1999.

[25] S. Endo, H. Kobayashi, C. J. Kempf, S. Kobayashi, M. Tomizuka, and Y. Hori, "Robust digital tracking controller design for high-speed positioning systems," *Control Eng. Practice*, vol. 4, pp. 527–536, 1996.

[26] M. Yasuda, T. Osaka, and M. Ikeda, "Feedforward control of a vibration isolation system for disturbance suppression," in *Proc. of the 35th Conf. on Decision and Control*, pp. 1229–1233, Kobe, Japan, Dec 1996.

[27] S. K. Kuo, and C. H. Menq, "Modeling and control of a six-axis precision motion control stage," *IEEE/ASME Trans. on Mechatronics*, vol. 10, no. 1, pp. 50–59, Feb. 2005.

[28] A. Sebastian and S. Salapaka, "$\mathcal{H}_\infty$ loop shaping design for nano-positioning," in *Proc. 2003 American Control Conference*, pp. 3708–3713, June 2003.

[29] J. Potzick, "Noise averaing and measurement resolution (or "A little noise is a good thing")," Review of Scientific Instruments, vol. 70, no. 4, pp. 2038–2040, Apr 1999.

[30] K. Nakashima, T. Tsujino, and T. Fujii, "Multivariable control of a magnetic levitation system using closed loop identification and H_∞ control theory," in *Proc. 35th Conf. on Decision and Control*, vol. 4, pp. 3668–3673, Dec. 1996.

[31] R. Becerril-Arreola, M. Maggiore, "Nonlinear stabilization of a 3 degrees-of-freedom magnetic levitation system," in *Proc. 2003 American Control Conference*, pp. 1092–1097, June 2003.

[32] H. Perez, Q. Zou, and S. Devasia, "Design and control of optimal scan trajectories: scanning tunneling microscope example," *Journal of Dynamical Systems, Measurement and Control*, vol. 126, no. 1, pp. 187–197, Mar. 2004.

[33] H. Chen, N. Xi, and Y. Chen, "Multi-objective optimal robot path planning in manufacturing," in *Proc. Intelligent Robots and Systems*, vol. 2, pp. 1167–1172, Oct. 2003.

[34] H. Shakir, W.-J. Kim, and S. Verma, "System identification and optimal control of a 6-DOF magnetic levitation stage with nanopositioning capabilities," in *Proc. of ASME IMECE 2004*, paper no. 60507, Nov. 2004.

[35] K. L. Moore and S. P. Bhattacharyya, "A technique for choosing locations for minimal overshoot," *IEEE Trans. on Automatic Control*, vol. 35, no. 5, pp. 577–580, May 1990.

[36] G. Deodhare and M. Vidyasagar, "Design of non-overshooting feedback control systems," in *Proc. 29th Conference on Decision and Control*, Honolulu, HI, pp. 1827–1834, Dec. 1990.

[37] S. F. Phillips and D. E. Seborg, "Conditions that guarantee no overshoot for linear systems," *Intl. J. of Control*, vol. 47, no. 4, pp. 1043–1059, 1988.

[38] M. Vidyasagar, "On overshoot and non-minimum phase zeros," *IEEE Trans. on Automatic Control*, vol. AC-31, no. 5, pp. 440, May 1986.

[39] S. Jayasuriya and A. G. Dharne, "Necessary and sufficient conditions for non-overshooting step responses for LTI systems," in *Proc. 2002 American Control Conference*, pp. 505–510, May 2002.

[40] S. Darbha and S. P. Bhattacharyya, "Controller synthesis for sign-invariant impulse response," *IEEE Trans. on Automatic Control*, vol. 47, no. 8, pp. 1346–1351, Aug. 2002.

[41] A. Datta, M.-T. Ho, and S. P. Bhattacharyya, "Structure and synthesis of PID controllers," *Advances in Industrial Control*, Springer, 2000, Chapter 5.

[42] M.-T. Ho, "Synthesis of $\mathcal{H}_\infty$ PID controllers: A parametric approach," *Automatica*, vol. 39, no. 6, pp. 1069–1075, June 2003.

[43] K. P. Wong, "Control and modeling strategies for non-linear systems with time delays," Ph.D. Dissertation, Dept. of Chem. Eng., University of California, Santa Barbara, CA, 1985.

[44] C. A. Markland, "Optimal model-following control system synthesis techniques," in *Proc. IEE*, vol. 117, pp. 623–627, 1970.

[45] L. H. Keel and S. P. Bhattacharyya, "Robust, fragile or optimal?" in *Proc. 1997 American Control Conference*, pp. 1307–1313, June 1997.

[46] D. Ditmore, J. Stewart, R. Dudley, and N. Bright, "Achieving semiconductor equipment reliability," in *Proc. of Seventh IEEE/CHMT Intl. Elec. Manf. Tech. Symposium*, pp. 5–11, Sep. 1989.

[47] P. F. Jacobs, *Stereolithography and other RP&M Technologies*. ASME Press, New York, 1996.

[48] V. K. Vardan, X. Jiang and V. V. Vardan, *Microstereolithography and other Fabrication Techniques for 3D MEMS*, John Wiley and Sons Ltd., 2001, pp. 111–127.

[49] L. Beluze, A. Bertsch, and P. Renaud, "Microstereolithography: A new process to build complex 3D objects," in *Proc. SPIE*, vol. 3680, pp. 808–817, Apr. 1999.

[50] X. Zhang, X. N. Jiang and C. Sun, "Microstereolithography of polymeric and ceramic microstructures," *Sensors and Actuators A (Physical)*, vol. A77, no. 2 , pp. 149–156, Mar. 1999.

[51] X. N. Jiang, C. Sun, X. Zhang, B. Xu, and Y. H. Ye, "Microstereolithography of lead zirconate titanate thick film on silicon substrate," *Sensors and Actuators A (Physical)*, vol. A87, no. 1-2 , pp. 72–77, May 2000.

[52] K. Ikuta, S. Maruo, and S. Kojima, "New microstereolithography for freely movable 3D microstructure–super IH process with submicron resolution," in *Proc. IEEE MEMS*, pp. 290–295, Jan. 1998.

[53] A. Sebastian, S. Salapaka, and M. V. Salapaka, *Lecture Notes in Control and Information Sciences*, Springer Berlin/Heidelberg, vol. 289, pp. 83–100, 2003.

[54] H. Richter, E. Misawa, and D. Lucca, H. Lu, "Modeling nonlinear behavior in a piezoelectric actuator," *Precision Engineering*, vol. 25, no. 2, pp. 128–137, Apr. 2001.

[55] C. Bauer, A. Bugacov, B. E. Koel, A. Madhukar, N. Montoya, T. R. Ramachandran, A. A. G. Requicha, R. Resch, and P. Will, "Nanoparticle manipulation by mechanical pushing: Underlying phenomena and real-time monitoring," *Nanotechnology*, vol. 9, no. 4, pp. 360–364, Dec. 1998.

[56] M. F. Yu, M. J. Dyer, H. W. Rohrs, X. K. Lu, K. D. Ausman, J. V. Her, and R. S. Ruoff, "Three-dimensional manipulation of carbon nanotubes under a scanning electron microscope," *Nanotechnology*, vol. 10, no. 3, pp. 244–252, Sep. 1999.

[57] R. M. Taylor, II, "The nanomanipulator: A virtual-reality interface to a scanning tunneling microscope," Ph.D. Dissertation, University of North Carolina at Chapel Hill, May 1994.

[58] S. Smith and D. Chetwynd, *Microscopic Staining Techniques*, London: Butterworths, 1963.

[59] A. A. G. Requicha, S. Meltzer, A. F. P. Terán, J. H. Makaliwe, H. Sikén, S. Hsieh, D. Lewis, B. E. Koel, and M. E. Thompson, "Manipulation of nanoscale components with the AFM: Principles and applications," in *Proc. IEEE-NANO 2001*, pp. 81–86, October 2001.

[60] Nanoink, Inc., *NSCRIPTOR DPN System Product Data Sheet*, 2002.

[61] J. Gu, "Development of a 6-degree-of-freedom magnetically levitated instrument with nanometer precision," Masters Thesis, Dept. of Mech. Eng., Texas A&M University, College Station, TX, May 2003.

[62] S. Verma, "Development of novel high-performance six-axis magnetically levitated instruments for nanoscale applications," Ph.D. Dissertation, Dept. of Mech. Eng., Texas A&M University, College Station, TX, Aug 2005.

[63] W.-J. Kim and H. Maheshwari, “High-precision control of a maglev linear actuator with nanopositioning capability,” in *Proc. 2002 American Control Conference*, Anchorage, AK, pp. 4279–4284, May 2002.

[64] W.-J. Kim, “Method and Apparatus for Magnetically Generating Motion with High Precision,” US Patent and Trademark Office (PTO) Patent No. 6,885,536 B1, April 26, 2005.

[65] S. Verma, W.-J. Kim, and J. Gu, “Six-axis nanopositioning device with precision magnetic levitation technology,” *IEEE/ASME Tr. on Mechatronics*, vol. 9, no. 2, pp. 384–391, June 2004.

[66] W.-J. Kim and S. Verma, “Magnetically Levitated Apparatus,” US PTO Provisional Patent No. 60/794,981, April 26, 2006.

[67] M. L. Culpepper and G. Anderson, “Design of a low-cost nanomanipulator which utilizes a monolithic, spatial compliant mechanism,” *Precision Engineering*, vol. 28, no. 4, pp. 469–482, Oct. 2004.

[68] A. H. Slocum, *Precision Machine Design*, Prentice-Hall, Inc. 1992.

[69] Agilent, Inc. *Agilent 10706B High Stability Plane Mirror Interferometer User Manual*, 2002.

[70] C. Y. Kim and K. H. Kim, “Gain scheduled control of magnetic suspension system,” in *Proc. 1994 American Control Conference*, pp. 3127–3131, June 1994.

[71] H. K. Khalil, *Nonlinear Systems*, 3rd ed., Prentice-Hall, 2002.

[72] M. French and E. Rogers, “Approximate parameterizations for adaptive feedback linearization,” in *Proc. on the 36th Conf. on Decision & Control,* pp. 4665–4670, Dec. 1997.

[73] A. J. Krener, *A Brief Tutorial on Linear and Nonlinear Control Theory*, Available online: www.samsi.info/200304/multi/akrener.pdf.

[74] S. A. Bortoff, “Approximate state-feedback linearization using spline functions,” *Automatica*, vol. 33, no. 8, pp. 1449–1458, Aug. 1997.

[75] B. Lennartson, “On the choice of controller and sampling period for linear stochastic control,” *Automatica*, vol. 26, no. 3, pp. 573–578, May 1990.

[76] S. Earnshaw, “On the nature of the molecular forces which regulate the constitution of the luminiferous ether,” *Trans. of the Cambridge Philosophical Society*, vol. 7, pp. 97–112, 1842.

[77] H. Goldstein, *Classical Mechanics*, 2nd ed., Addison-Wesley Publishing Co., Inc., 1980.

[78] S. Stogestad and I. Postlewaite, *Multivariable Feedback Control*, John Wiley and Sons, 2003.

[79] P. S. Maybeck, *Stochastic Models, Estimation and Control, Part I*, Academic Press, 1979.

[80] D. Bullen, X. Wang, J. Zou, S. Hong, S-W. Chung, K. Ryu, Z. Fan, C. Mirkin, and C. Liu, “Micromachined arrayed dip pen nanolithography probes for sub-100 nm direct chemistry patterning,” in *Proc. of IEEE 16th Annual International Conference on Micro Electro Mechanical Systems*, pp. 4–7, Jan. 2003.

[81] Nanoink, Inc., *Inkwell Arrays Product Data Sheet*, 2003.

[82] R. Lawes, (2002, Dec. 10). Microfabrication cost models for micromachining methods. Central Microstructure Facility. Available online: http://www.cmf.rl.ac.uk/latest/msl.html.

VITA

Name: Huzefa Shakir

Address: 102 Khara Kunwa Bahaderpura
Ujjain, MP – 456 006 India

Email: huz.shak@gmail.com

Education: Texas A&M University, College Station, TX. May 2007
Doctor of Philosophy in Mechanical Engineering

Indian Institute of Technology, Kharagpur, India. July 2000
Bachelor of Technology (Honors) in Mechanical Engineering

Employment: Senior Scientist, Halliburton

Publications:

[1] H. Shakir and W.-J. Kim, "Multiscale control for nano-precision positioning systems with large throughput," *IEEE Trans. on Control Systems Technology*, in press, Dec. 2006.

[2] W.-J. Kim, S. Verma, and H. Shakir, "Design and precision construction of novel magnetic-levitation based multi-axis nanoscale positioning systems," *Precision Engineering*, revised and resubmitted, Dec. 2006.

[3] H. Shakir and W.-J. Kim, "Nanoscale path planning and motion control for maglev nanopositioners," *IEEE/ASME Trans. on Mechatronics*, vol. 11, no. 5, pp. 625–633, Oct. 2006.

[4] S. Verma, H. Shakir, and W.-J. Kim, "Novel actuation scheme for multi-axis nanopositioning," *IEEE Trans. on Magnetics*, vol. 42, no. 8, pp. 2052–2062, Aug. 2006.

[5] S. Verma, W.-J. Kim, and H. Shakir, "Multi-axis maglev nanopositioner for precision manufacturing and manipulation applications," *IEEE Trans. on Industry Applications*, vol. 41, no. 5, pp. 1159–1167, Sep. 2005.

Awards:

[1] International Texas Public Education Grant, June 2006

[2] Best presentation award – American Control Conference, June 2005

[3] Fellow, Graduate Teaching Academy, Center for Teaching Excellence, Texas A&M University, May 2005

[4] Invited member, The Honor Society of Phi Kappa Phi, Apr. 2003

[5] "Hall Color," Rajendra Prasad Hall of Residence, Indian Institute of Technology, Kharagpur, India for excellence in fine arts, Mar. 2000